Efficient color-dressed calculation of virtual corrections

Walter T. Giele [a], Zoltan Kunszt [b,c], Jan Winter [a,*]

[a] *Fermilab, Batavia, IL 60510, USA*
[b] *Institute for Theoretical Physics, ETH, CH-8093 Zürich, Switzerland*
[c] *Theoretical Physics, CERN, CH-1211 Geneva, Switzerland*

Abstract

With the advent of generalized unitarity and parametric integration techniques, the construction of a generic Next-to-Leading Order Monte Carlo becomes feasible. Such a generator will entail the treatment of QCD color in the amplitudes. We extend the concept of color dressing to one-loop amplitudes, resulting in the formulation of an explicit algorithmic solution for the calculation of arbitrary scattering processes at Next-to-Leading order. The resulting algorithm is of exponential complexity, that is the numerical evaluation time of the virtual corrections grows by a constant multiplicative factor as the number of external partons is increased. To study the properties of the method, we calculate the virtual corrections to n-gluon scattering.
Published by Elsevier B.V.

1. Introduction

Automated Leading Order (LO) generators [1–8] play an essential role in experimental analyses and phenomenology in general. However, the theoretical uncertainties associated with these generators are only understood qualitatively. The augmentation of the LO generators with Next-to-Leading Order (NLO) corrections will give a more quantitative understanding of the theoretical uncertainties. This is crucial for the realization of precision measurements at the Hadron colliders. By calculating NLO corrections using analytic generalized unitarity methods [9–11], the one-loop amplitude is factorized into sums over products of on-shell tree-level amplitudes.

---

* Corresponding author.
  E-mail address: jwinter@fnal.gov (J. Winter).

This makes the integration of numerical generalized unitarity methods into the LO generators attractive. One can use the LO generator as the building block for obtaining the NLO correction, thereby negating the need for a separate generator of all the one-loop Feynman diagrams. The generalized unitarity approach reduces the complexity of the calculation through factorization. It can reduce the evaluation time with increasing number of external particles from faster than factorial growth to slower than factorial growth.

By utilizing the parametric integration method of Ref. [12] significant progress has been made in the algorithmic implementation of generalized unitarity based one-loop generators [13,14] and other non-unitary methods [15].[1] These implementations rely on the color decomposition of the amplitude into colorless, gauge invariant ordered amplitudes [24,25]. At tree-level these ordered amplitudes can be efficiently calculated by recursion relation algorithms [26,27]. These algorithms are of polynomial complexity and grow asymptotically as n^4 as the number of external partons, n, increases [28,29]. By replacing the 4-gluon vertex by an effective 3-gluon vertex the polynomial growth factor can be further reduced to n^3 [30–32].

At the one-loop level the ordered amplitudes generalize into primitive amplitudes [33]. These primitive amplitudes reflect the more complicated dipole structure of one-loop amplitudes. While the analytic structure of the factorized one-loop amplitude in color factors and primitive amplitudes is systematic, the subsequent calculation of the color summed virtual corrections becomes unwieldy in the algorithmic implementation [34]. The reason for this is the rapid growth in the number of primitive amplitudes. This rapid growth is mainly caused by the multiple quark-pairs amplitudes. A further complication arises from the possible presence of electro-weak particles in the ordered amplitudes.

While in LO generators the analytic treatment of color is more manageable, alternatives were developed for high parton multiplicity scattering amplitudes [31,35,32]. Those alternatives provided a more numerical treatment of the color, thereby facilitating the construction of tree-level Monte Carlo programs for the automated generation of high multiplicity parton scattering amplitudes at LO. This was accomplished by not only choosing the external momenta and helicities, but also choosing the explicit colors of the external partons for each scattering event considered. In doing so, the tree-level partonic amplitude is a complex number and the absolute value squared is simply calculated. This numerical treatment can be done in the context of ordered amplitudes [7] by calculating the explicit color weights of each ordered amplitude. This method was generalized to one-loop calculations in Ref. [15]. More directly, one can reformulate the recursion relations into color-dressed recursion relations [36,31,32]. These color-dressed recursion relations integrate the now explicit color weights into the recursive formula. The resulting algorithm is of exponential complexity and grows asymptotically as 4^n for n-parton amplitudes; again, a reduction of the growth factor to 3^n can be achieved if the 4-gluon vertex is replaced by the effective 3-gluon vertex [32].

In this paper we extend the generalized unitarity method of Ref. [13] as implemented in Ref. [37] to incorporate the color-dressing method. The algorithm is developed such that it can augment a dressed LO generator such as COMIX [8] to become a NLO generator.[2] For the numerical examples presented in this paper, we have used our own implementation of a color-dressed LO gluon recursion relation to calculate the virtual corrections for n-gluon scattering processes.

---

[1] These methods have matured to the point where explicit NLO parton generators for specific processes have been constructed [16–23].

[2] The LO generator needs to be upgraded to allow for complex momenta in the evaluation of tree-level matrix elements.

The motivation for color dressing at the one-loop level is discussed in Section 2. We outline in Section 3 the tree-level dressed recursion relations for generic theories expressed in terms of Feynman diagrams. We optimize the color-sampling performance and study the phase-space integration convergence for LO n-gluon scattering. The dressed formalism is extended to one-loop amplitudes in Section 4. The scaling with n, the accuracy of the algorithm and the color-sampling convergence of the virtual corrections to n-gluon scattering are studied in some detail. We summarize our results in Section 5. Finally, two appendices are added giving an explicit LO 6-quark example and details on the color-dressed implementation of the gluon recursion relation.

2. Motivation for the color-dressed generalized unitarity method

So far the numerical implementations of generalized unitarity for the evaluation of one-loop amplitudes make use of color ordering: the ordered one-loop amplitudes are constructed from tree-level ordered amplitudes through the D-dimensional unitarity cuts. This has the advantage that the color is factorized off the loop calculation and attached subsequently to each ordered one-loop amplitude. For the pure gluon one-loop amplitude, this leads to a particularly simple decomposition in terms of the adjoint generators F of SU(N):

$$\mathcal{M}^{(0,1)}(1,2,\ldots,n) \sim \sum_{P(2,3,\ldots,n)} \text{Tr}\big(F^{a_1} F^{a_2} \cdots F^{a_n}\big) m^{(0,1)}(1,2,\ldots,n). \tag{1}$$

The decomposition is valid for both tree-level [24] and one-loop amplitudes [38]. Once we can calculate the colorless ordered amplitude $m(1,2,\ldots,n)$, all other ordered amplitudes are obtained by simple permutations. All kinematic information about the n-gluon amplitude is encapsulated in a single ordered amplitude. However, we also see the drawback of this approach as we are interested in evaluating the amplitude squared. We have to calculate $\mathcal{M}^{(0,1)}(1,2,\ldots,n) \times (\mathcal{M}^{(0)}(1,2,\ldots,n))^\dagger$ summed over all color and spin states of the external gluons. This immediately leads to a factorial complexity when doing the multiplications of the full amplitudes as we have to sum over the permutations, $P(2,3,\ldots,n)$, of the ordered amplitudes. Additionally, the color sum has to be performed either analytically or in some numerical manner.

When including quark pairs the situation becomes even more complicated. The reason is that the internal structure of the one-loop amplitude is not uniquely defined by the external states, thereby affecting the color flow of the ordered amplitudes. As a result there exist many types of ordered amplitudes depending on the internal configuration of quark and gluon propagators. These amplitudes are called primitive amplitudes [33] and in general cannot be obtained from each other by simple permutations. For example, the one-loop $q\bar{q} + n$ gluon amplitude is given by [38]

$$\mathcal{M}^{(1)}(q;1,\ldots,n;\bar{q})$$
$$\sim \sum_{k=2}^{n} \sum_{P(1,\ldots,n)} \big(T^y T^{a_1} \cdots T^{a_k} T^x\big)_{ij} \big(F^{a_{k+1}} \cdots F^{a_n}\big)_{xy} m^{(1)}(q,1,\ldots,k,q,k+1,\ldots,n),$$
$$\tag{2}$$

where the T-matrices are the fundamental generators of SU(N). While for the full amplitude a cut line has an undetermined flavor, each primitive amplitude has an unique flavor for all the cut lines. Therefore we can apply generalized unitarity to the primitive amplitudes. However, from a numerical/algorithmic point of view the evaluation of this equation becomes tedious as

can be seen for instance in the calculation of the one-loop matrix elements for $W + 5$ partons in Ref. [34].

It is clear that for an automated generator of one-loop corrections one would like to avoid ordered and/or primitive amplitudes altogether. For LO matrix elements, this can be done by applying the color-dressed recursion relations to evaluate the (unordered) tree-level amplitudes. From these color-dressed tree-level amplitudes we can build the one-loop color-dressed amplitudes by applying generalized unitarity, thereby circumventing the need for primitive amplitudes and explicit color summations. It is of interest to investigate the feasibility of this approach. The n-gluon scattering process is good for studying the behavior of the dressed algorithm. The color-ordered approach is most effective for n-gluon scattering. For processes with quark-pairs, the color-dressed approach will become even more efficient compared to the color-ordered approach.

An additional advantage of the color-dressed algorithm is that it treats partons and color neutral particles on the same footing. Specifically, we can include electro-weak particles without altering the algorithm. This is in contrast to the color-ordered algorithm, where the addition of electro-weak particles would lead to significant modifications in the algorithmic implementation of the method.

3. Dressed recursive techniques for leading order amplitudes

In tree-level generators the Monte Carlo sampling over the external color and helicity states has become a standard practice [31,35,32]. Such a color sampling allows for the efficient evaluation of large multiplicity partonic processes. A particular efficient implementation of the color-dressed Monte Carlo method uses the color-flow decomposition of the multi-parton amplitudes [39,40,31,41,42,6,43,32].

The principle of Monte Carlo sampling over the states of the external sources generalizes to any theory expressible through Feynman rules. By explicitly specifying the quantum numbers of the n external sources, one can evaluate the tree-level amplitude squared and differential cross section using Monte Carlo sampling:

$$d\sigma_{\text{LO}}(f_1 f_2 \to f_3 \cdots f_n)$$
$$= \frac{W_{\text{S}}}{N_{\text{event}}} \times \sum_{r=1}^{N_{\text{event}}} d\text{PS}^{(r)}(K_1 K_2 \to K_3 \cdots K_n) \big| \mathcal{M}^{(0)}\big(\mathbf{f}_1^{(r)}, \mathbf{f}_2^{(r)}, \ldots, \mathbf{f}_n^{(r)}\big)\big|^2, \tag{3}$$

where

$$\mathbf{f}_i^{(r)} = \{f_i, h_{f_i}, C_{f_i}, K_{f_i}\}^{(r)} \tag{4}$$

denotes the flavor, spin, color and momentum four-vector of external state i for event r.[3] The constant W_{S} contains the appropriate identical particle factors and Monte Carlo sampling weights. For each event r, the external states are stochastically chosen such that when summed over many events we approximate the correct differential cross section with sufficient accuracy.

---

[3] We will use flavor to indicate the particle type, such as e.g. gluon, up-quark, W-boson, etc.

3.1. The generic recursive formalism

To calculate the tree-level amplitude $\mathcal{M}^{(0)}$ in Eq. (3), we follow the method of color-dressed recursion relations as detailed in Refs. [32,8]. A recursion relation builds multi-particle currents from other currents. The m-particle current $J_{\mathbf{g}}(\mathbf{f}_\pi)$ has m on-shell particles $\mathbf{f}_\pi = \{\mathbf{f}_i\}_{i \in \pi} = \{\mathbf{f}_{i_1}, \ldots, \mathbf{f}_{i_m}\}$ where $\pi = \{i_1, \ldots, i_m\}$ and one off-shell particle $\mathbf{g} = \{g, L_g, C_g, K_g\}$ with g, L_g, C_g and K_g denoting the flavor, Lorentz label, color and four-momentum, respectively. The momentum of the off-shell particle, K_g, is constrained by momentum conservation: $K_g = -K_\pi = -\sum_{i \in \pi} K_i$.

The dressed recursion relation generates currents using the propagators and interaction vertices of the theory. Using standard tensor notation we can write the propagators as

$$P^{\mathbf{g_1 g_2}}(Q) = \delta_{g_1 g_2} \delta_{C_{g_1} C_{g_2}} P^{L_{g_1} L_{g_2}}(Q),$$

$$P^{\mathbf{g}}\big[J(\mathbf{f}_\pi)\big] = \sum_{\mathbf{g_1}} P^{\mathbf{g g_1}}(K_\pi) J_{\mathbf{g_1}}(\mathbf{f}_\pi),$$

$$P\big[J(\mathbf{f}_{\pi_1}), J(\mathbf{f}_{\pi_2})\big] = \sum_{\mathbf{g_1 g_2}} J_{\mathbf{g_1}}(\mathbf{f}_{\pi_1}) P^{\mathbf{g_1 g_2}}(K_{\pi_1}) J_{\mathbf{g_2}}(\mathbf{f}_{\pi_2}), \tag{5}$$

where e.g. the gluon propagator is given by $P^{\mu_1 \mu_2}(Q) = -g^{\mu_1 \mu_2}/Q^2$. Note that the particle sums are taken over all quantum numbers of the off-shell particles $\mathbf{g}_i$. Furthermore, in all expressions momentum conservation is always implicitly understood. The on-shell tree-level n-particle amplitude can hence be expressed in terms of an $(n-1)$-current,

$$\mathcal{M}^{(0)}(\mathbf{f}_1, \ldots, \mathbf{f}_n) = P^{-1}\big[J(\mathbf{f}_1, \ldots, \mathbf{f}_{n-1}), J(\mathbf{f}_n)\big]. \tag{6}$$

We denote the interaction vertices of the theory as $V_{\mathbf{g_1} \cdots \mathbf{g_k}}(Q_1, \ldots, Q_k)$. The maximal number of legs for the allowed vertices of the theory is denoted by $V_{\max}$. The number of legs of the vertex is indicated by the number of its arguments and the type of vertex is specified by the quantum numbers of the legs. The labels $\mathbf{g_1}, \ldots, \mathbf{g_k}$ run over the values of all particles of the theory. Symmetries and renormalizability imply that many of the vertices are set to zero. The theory is defined by its particle content and its non-vanishing vertices, which are generalized tensors:

$$V_{\mathbf{g_1} \cdots \mathbf{g_k}}(Q_1, \ldots, Q_k) = V^{L_{g_1} \cdots L_{g_k}}_{g_1 \cdots g_k; C_{g_1} \cdots C_{g_k}}(Q_1, \ldots, Q_k). \tag{7}$$

The sum of all vertices contracted in with currents constitutes the main building block of the recursion relation. We define it as

$$D_{\mathbf{g}}\big[J(\mathbf{f}_{\pi_1}), \ldots, J(\mathbf{f}_{\pi_k})\big] = \sum_{\mathbf{g_1} \cdots \mathbf{g_k}} V_{\mathbf{g g_1} \cdots \mathbf{g_k}}(K_g = -K_{\Pi_k}, K_{\pi_1}, \ldots, K_{\pi_k})$$
$$\times J^{\mathbf{g_1}}(\mathbf{f}_{\pi_1}) \times \cdots \times J^{\mathbf{g_k}}(\mathbf{f}_{\pi_k}), \tag{8}$$

where the inclusive list Π_k is build up of unions of the exclusive lists:

$$\Pi_k = \bigcup_{i=1}^{k} \pi_i. \tag{9}$$

Fig. 1 is a pictorial representation of Eq. (8) when using the example of QCD. For this case, we will work out the generic vertex blob in detail in the next subsection.
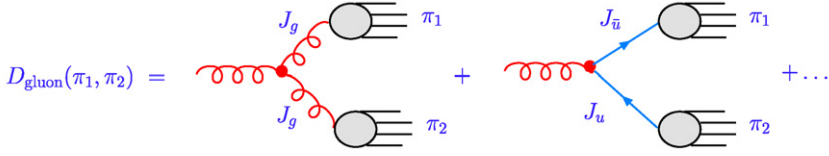
Fig. 1. A graphical representation of Eq. (8) for $k = 2$ and an off-shell gluon in QCD. Because of flavor conservation only one of the two vertices can contribute for any given partition.
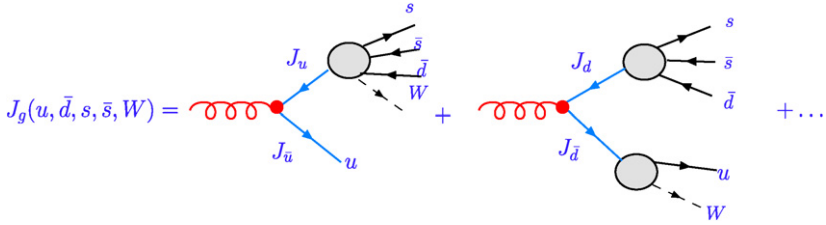

Fig. 2. The first recursion step for the unordered gluon current with $u, \bar{d}, s, \bar{s}$ quarks and a W^- gauge boson in the final state. There are 15 contributions corresponding to all possible partitions of the final-state particles into two groups. Because of flavor conservation there are only 4 non-vanishing contributions for the "$4 + 1$" partitions (first term) and 2 non-vanishing contributions for the "$3 + 2$" partitions (second term).

The recursion relations terminate with the one-particle currents. A one-particle $\mathbf{g}$-current is defined in terms of the source $S^{h_{f_i} C_{f_i}}_{f_i L_g}(K_{f_i})$. Hence, we have

$$J_{\mathbf{g}}(\mathbf{f}_i) = \delta^{g f_i} \delta^{C_g C_{f_i}} S^{h_{f_i} C_{f_i}}_{f_i L_g}(K_{f_i}). \tag{10}$$

For example, the $\mathbf{g}_1$-gluon one-particle source with helicity λ_1, color c_1 and momentum K_1 is given by $J_{\mathbf{g}}(\mathbf{g}_1) = \delta^{c c_1} \epsilon^{\lambda_1}_{\mu_1}(K_1)$. I.e. the $\mathbf{g}_1$-gluon source is a matrix in color space multiplied by the helicity vector.

The n-particle currents are now efficiently calculated from a recursively defined current in the following manner:

$$J_{\mathbf{g}}(\mathbf{f}_1, \ldots, \mathbf{f}_n) = \sum_{k=2}^{V_{\max}-1} \sum_{P_{\pi_1 \cdots \pi_k}(1,\ldots,n)}^{\mathcal{S}_2(n,k)} P_{\mathbf{g}}\big[D\big[J(\mathbf{f}_{\pi_1}), \ldots, J(\mathbf{f}_{\pi_k})\big]\big], \tag{11}$$

where $\mathcal{S}_2(n, k)$ is the Stirling number of the second kind. The first recursive step is graphically illustrated in Fig. 2 for the example of $J_{\mathbf{g}}(\mathbf{u}, \bar{\mathbf{d}}, \mathbf{s}, \bar{\mathbf{s}}, \mathbf{W}^-)$. The sum over $P_{\pi_1 \cdots \pi_k}(1, \ldots, n)$ generates all different partitions decomposing the set $\{1, \ldots, n\}$ into the non-empty subsets $\pi_1, \ldots, \pi_k$. An example for a list of different partitions is

$$\begin{aligned}
P_{\pi_1 \pi_2 \pi_3}(1, 2, 3, 4) &= \big\{\pi_1^{(i)} \pi_2^{(i)} \pi_3^{(i)}\big\}_{i=1}^{\mathcal{S}_2(4,3)=6} \\
&= \big\{\{\{1, 2\}\{3\}\{4\}\}, \{\{1, 3\}\{2\}\{4\}\}, \{\{1, 4\}\{2\}\{3\}\}, \\
&\quad \{\{2, 3\}\{1\}\{4\}\}, \{\{2, 4\}\{1\}\{3\}\}, \{\{3, 4\}\{1\}\{2\}\}\big\}.
\end{aligned} \tag{12}$$

The formalism described here fully specifies an automated algorithm of exponential complexity to calculate the LO differential cross sections for any theory defined in terms of Feynman rules. Owing to the characteristics of the partitioning, the computer resources needed to calculate

the n-particle tree-level amplitudes asymptotically grow in proportion to $\mathcal{S}_2(n, V_{max})$. The exponential behavior arises from the large-n limit of the Stirling numbers, i.e. $\mathcal{S}_2(n, V_{max}) \to V_{max}^n$ [30]. It may be possible to reduce V_{max} by rewriting higher multiplicity vertices as sums of lower multiplicity vertices thereby improving the efficiency of the recursive algorithm [31,6,32]. For the case of the Standard Model, this has been fully worked out in Ref. [8] and implemented in the COMIX LO generator.

3.2. Multi-jet scattering amplitudes

We specify the generic recursion relations to the perturbative QCD Feynman rules. This will give an algorithmic description of the scattering amplitudes at LO for multi-jet production at hadron colliders.

The external sources are gluons and massless quarks. All these particles have color and helicity as quantum numbers. Instead of the traditional color representation in terms of fundamental generators, we choose the color-flow representation [4,43,6,32], which is more pertinent to Monte Carlo sampling and easily derivable from the traditional color representation by making the following two observation: first, any internal propagating gluon has as a color factor $\delta^{ab} = \text{Tr}(T^a T^b)$. This color factor can be rewritten as

$$\mathcal{M} = \mathcal{A}_a \frac{\delta^{ab}}{K^2} \mathcal{B}_b = \mathcal{A}_a \frac{\text{Tr}(T^a T^b)}{K^2} \mathcal{B}_b = \mathcal{A}_{ij} \frac{1}{K^2} \mathcal{B}^{ji}. \tag{13}$$

Second, we contract the amplitude with $T^{a_k}_{i_k j_k}$ for each external gluon:

$$|\mathcal{M}|^2 = \mathcal{M}^a \delta_{ab} (\mathcal{M}^b)^\dagger = \mathcal{M}^a T^a_{ij} T^b_{ji} (\mathcal{M}^b)^\dagger = \mathcal{M}_{ij} \mathcal{M}^\dagger_{ji}. \tag{14}$$

From these observations it follows that we can calculate the interaction vertices in the color-flow representation by simply contracting each gluon with $T^{a_k}_{i_k j_k}$ and summing over a_k. The three gluon vertex is thus given by

$$\begin{aligned}
V_{\mathbf{g}_1 \mathbf{g}_2 \mathbf{g}_3}(K_1, K_2, K_3) &= V^{\mu_1 \mu_2 \mu_3}_{i_1 j_1 i_2 j_2 i_3 j_3}(K_1, K_2, K_3) \\
&= T^{a_1}_{i_1 j_1} T^{a_2}_{i_2 j_2} T^{a_3}_{i_3 j_3} V^{\mu_1 \mu_2 \mu_3}_{a_1 a_2 a_3}(K_1, K_2, K_3) \\
&= T^{a_1}_{i_1 j_1} T^{a_2}_{i_2 j_2} T^{a_3}_{i_3 j_3} f^{a_1 a_2 a_3} \sqrt{2} \widehat{V}^{\mu_1 \mu_2 \mu_3}_3(K_1, K_2, K_3) \\
&= \left(\delta^{i_1}_{j_2} \delta^{i_2}_{j_3} \delta^{i_3}_{j_1} - \delta^{i_1}_{j_3} \delta^{i_2}_{j_1} \delta^{i_3}_{j_2} \right) \widehat{V}^{\mu_1 \mu_2 \mu_3}_3(K_1, K_2, K_3),
\end{aligned} \tag{15}$$

with

$$\begin{aligned}
\widehat{V}^{\mu_1 \mu_2 \mu_3}_3(K_1, K_2, K_3) = \frac{1}{\sqrt{2}} \Big(&(K_1 - K_2)^{\mu_3} g^{\mu_1 \mu_2} + (K_2 - K_3)^{\mu_1} g^{\mu_2 \mu_3} \\
&+ (K_3 - K_1)^{\mu_2} g^{\mu_3 \mu_1} \Big).
\end{aligned} \tag{16}$$

Similarly, for the four gluon vertex we find

$$V_{\mathbf{g}_1 \mathbf{g}_2 \mathbf{g}_3 \mathbf{g}_4} = V^{\mu_1 \mu_2 \mu_3 \mu_4}_{i_1 j_1 i_2 j_2 i_3 j_3 i_4 j_4} = \sum_{C(234)} \left(\delta^{i_1}_{j_2} \delta^{i_2}_{j_3} \delta^{i_3}_{j_4} \delta^{i_4}_{j_1} + \delta^{i_1}_{j_4} \delta^{i_2}_{j_1} \delta^{i_3}_{j_2} \delta^{i_4}_{j_3} \right) \widehat{V}^{\mu_1 \mu_3, \mu_2 \mu_4}_4, \tag{17}$$

with

$$\widehat{V}^{\mu_1 \mu_2, \mu_3 \mu_4}_4 = 2 g^{\mu_1 \mu_2} g^{\mu_3 \mu_4} - g^{\mu_1 \mu_3} g^{\mu_2 \mu_4} - g^{\mu_1 \mu_4} g^{\mu_2 \mu_3}, \tag{18}$$

and the sum is over the cyclic permutation of the indices $\{2, 3, 4\}$. In the color-flow representation the quark–antiquark–gluon vertex is given by

$$V_{\mathbf{q}\mathbf{g}\bar{\mathbf{q}}} = V_{i,i_1 j_1,j}^{s\mu\bar{s}} = \left(\delta_{ij_1}\delta_{i_1 j} - \frac{1}{N_{\mathrm{C}}}\delta_{i_1 j_1}\delta_{ij} \right) \widehat{V}^{s\mu\bar{s}}, \tag{19}$$

with

$$\widehat{V}_{s\bar{s}}^{\mu} = \frac{1}{\sqrt{2}}\gamma_{s\bar{s}}^{\mu}. \tag{20}$$

The external sources are given by

$$J_{\mathbf{g}}(\mathbf{g}_1) = \delta^{Ii_1}\delta^{Jj_1}\varepsilon_{\mu}^{\lambda_1}(K_1),$$
$$J_{\mathbf{q}}(\mathbf{q}_1) = \delta^{Ii_1}v_s^{\lambda_1}(K_1),$$
$$J_{\bar{\mathbf{q}}}(\bar{\mathbf{q}}_1) = \delta^{Jj_1}\bar{u}_{\bar{s}}^{\lambda_1}(K_1), \tag{21}$$

where $\mathbf{g} = \{g, \mu, (IJ), -K_1\}$, $\mathbf{g}_1 = \{g_1, \lambda_1, (i_1 j_1), K_1\}$, $\mathbf{q} = \{q, s, I, -K_1\}$, $\mathbf{q}_1 = \{q_1, \lambda_1, i_1, K_1\}$, $\bar{\mathbf{q}} = \{\bar{q}, \bar{s}, J, -K_1\}$ and $\bar{\mathbf{q}}_1 = \{\bar{q}_1, \lambda_1, j_1, K_1\}$. The internal propagating particles are given by

$$P^{\mathbf{g}_1 \mathbf{g}_2}(Q) = \delta_{j_2}^{i_1}\delta_{j_1}^{i_2}\left(\frac{-g_{\mu_1\mu_2}}{Q^2} \right),$$
$$P^{\mathbf{q}_1 \mathbf{q}_2}(Q) = \delta_{i_2}^{i_1}(\slashed{Q} - m_{q_1})_{s_1 s_2}^{-1},$$
$$P^{\bar{\mathbf{q}}_1 \bar{\mathbf{q}}_2}(Q) = \delta_{j_2}^{j_1}(\slashed{Q} + m_{\bar{q}_1})_{\bar{s}_1 \bar{s}_2}^{-1}, \tag{22}$$

with $\mathbf{g}_k = \{g_k, \mu_k, (i_k j_k), Q\}$, $\mathbf{q}_k = \{q_k, s_k, i_k, Q\}$ and $\bar{\mathbf{q}}_k = \{\bar{q}_k, \bar{s}_k, j_k, Q\}$.

We can now construct Berends–Giele recursion relations [26] using color-dressed multi-parton currents based on Eq. (11). The result is

$$J_{\mathbf{q}}(\mathbf{f}_1, \ldots, \mathbf{f}_n) = \sum_{P_{\pi_1\pi_2}(1,\ldots,n)} P_{\mathbf{q}}\big[D\big[J(\mathbf{f}_{\pi_1}), J(\mathbf{f}_{\pi_2})\big]\big],$$

$$J_{\mathbf{g}}(\mathbf{f}_1, \ldots, \mathbf{f}_n) = \sum_{P_{\pi_1\pi_2}(1,\ldots,n)} P_{\mathbf{g}}\big[D\big[J(\mathbf{f}_{\pi_1}), J(\mathbf{f}_{\pi_2})\big]\big]$$
$$+ \sum_{P_{\pi_1\pi_2\pi_3}(1,\ldots,n)} P_{\mathbf{g}}\big[D\big[J(\mathbf{f}_{\pi_1}), J(\mathbf{f}_{\pi_2}), J(\mathbf{f}_{\pi_3})\big]\big], \tag{23}$$

where each current violating flavor conservation is defined to give zero. The compact operator language can be expanded out to an explicit formula by adding back in the particle attributes. For example,

$$P_{\mathbf{g}}\big[D\big[J(\mathbf{f}_{\pi_1}), J(\mathbf{f}_{\pi_2})\big]\big] = \sum_{\mathbf{q}\mathbf{g}_1\bar{\mathbf{q}}} P_{\mathbf{g}\mathbf{g}_1}(K_{\Pi_2})V^{\mathbf{q}\mathbf{g}_1\bar{\mathbf{q}}}J_{\mathbf{q}}(\mathbf{f}_{\pi_1})J_{\bar{\mathbf{q}}}(\mathbf{f}_{\pi_2})$$

$$+ \sum_{\mathbf{g}_1\mathbf{g}_2\mathbf{g}_3} P_{\mathbf{g}\mathbf{g}_1}(K_{\Pi_2})V^{\mathbf{g}_1\mathbf{g}_2\mathbf{g}_3}(-K_{\pi_1\cup\pi_2}, K_{\pi_1}, K_{\pi_2})J_{\mathbf{g}_2}(\mathbf{f}_{\pi_1})J_{\mathbf{g}_3}(\mathbf{f}_{\pi_2})$$

$$= \frac{1}{K_{\Pi_2}^2}V_{i,IJ,j}^{s_1\mu s_2} \times J_{s_1}^i(\mathbf{f}_{\pi_1}) \times J_{s_2}^j(\mathbf{f}_{\pi_2})$$

$$+ \frac{1}{K_{\Pi_2}^2}V_{IJi_2 j_2 i_3 j_3}^{\mu\mu_1\mu_2}(-K_{\pi_1\cup\pi_2}, K_{\pi_1}, K_{\pi_2})$$

$$\times J_{\mu_1}^{(ij)_2}(\mathbf{f}_{\pi_1}) \times J_{\mu_2}^{(ij)_3}(\mathbf{f}_{\pi_2}). \tag{24}$$

The n-parton tree-level matrix element is calculated using Eq. (6). We exemplify in Appendix A how to work out the 6-quark recursion steps using the above formalism.

3.3. Numerical implementation of n-gluon scattering

The method of color dressing as discussed in this section relies on the ability to perform a Monte Carlo sampling over the degrees of freedom of the external sources. In this subsection we will study in some detail the properties of such a sampling approach by means of the color-dressed gluonic recursion relation. We are particularly interested in the accuracy of the color-sampling procedure and overall speed of the implementation. The addition of quarks and external vector bosons is a straightforward extension and will not affect the conclusions reached in this subsection.

The explicit color-dressed gluon recursion algorithm is given in terms of colored gluonic currents. The gluonic currents are 3×3 matrices in color space and defined as

$$J_{\mathbf{g}}(\mathbf{g}_m) = \delta^{I i_m} \delta^{J j_m} \varepsilon_\mu^{\lambda_m}(K_m),$$

$$J_{\mathbf{g}}(\mathbf{g}_1, \ldots, \mathbf{g}_m) = \sum_{P_{\pi_1 \pi_2}(1,\ldots,m)} P_{\mathbf{g}}\big[D\big[J(\mathbf{g}_{\pi_1}), J(\mathbf{g}_{\pi_2})\big]\big]$$

$$+ \sum_{P_{\pi_1 \pi_2 \pi_3}(1,\ldots,m)} P_{\mathbf{g}}\big[D\big[J(\mathbf{g}_{\pi_1}), J(\mathbf{g}_{\pi_2}), J(\mathbf{g}_{\pi_3})\big]\big]. \tag{25}$$

The color-dressed n-gluon amplitude is given by

$$\mathcal{M}^{(0)}(\mathbf{g}_1, \mathbf{g}_2, \ldots, \mathbf{g}_n) = P^{-1}\big[J(\mathbf{g}_1, \mathbf{g}_2, \ldots, \mathbf{g}_{n-1}), J(\mathbf{g}_n)\big]. \tag{26}$$

For this specific example, we have labelled the on-shell gluons by $\mathbf{g}_i$, the off-shell gluon is denoted by $\mathbf{g}$ as before. The operator formulation of the recursive algorithm is particularly suited for an object oriented implementation of the recursive algorithm. We have implemented the algorithm presented above in C++. More details including the more explicit recursion equation are shown in Appendix B.

The first issue to deal with is the correctness of the implemented algorithm. To this end we want to compare the color-dressed amplitude to existing evaluations of the gluonic amplitudes based on ordered amplitudes. To facilitate the comparison, we write the color-ordered expansion of the amplitude using the color-flow representation [43]:

$$\mathcal{M}^{(0)}(\mathbf{g}_1, \mathbf{g}_2, \ldots, \mathbf{g}_n) = \sum_{P(2,\ldots,n)} A^{(0)\,i_1 \cdots i_n}_{j_1 \cdots j_n}\big(g_1^{\lambda_1}, \ldots, g_n^{\lambda_n}\big)$$

$$= T^{a_1}_{i_1 j_1} \cdots T^{a_n}_{i_n j_n} \sum_{P(2,\ldots,n)} \mathrm{Tr}\big(F^{a_1} \cdots F^{a_n}\big) m^{(0)}\big(g_1^{\lambda_1}, \ldots, g_n^{\lambda_n}\big)$$

$$= \frac{1}{2} \sum_{P(2,\ldots,n)} \big(\delta^{i_1}_{j_2} \delta^{i_2}_{j_3} \cdots \delta^{i_{n-1}}_{j_n} \delta^{i_n}_{j_1} + (-1)^n \delta^{i_n}_{j_{n-1}} \delta^{i_{n-1}}_{j_{n-2}} \cdots \delta^{i_2}_{j_1} \delta^{i_1}_{j_n}\big)$$

$$\times m^{(0)}\big(g_1^{\lambda_1}, \ldots, g_n^{\lambda_n}\big)$$

$$= \sum_{P(2,\ldots,n)} \delta^{i_1}_{j_2} \delta^{i_2}_{j_3} \cdots \delta^{i_{n-1}}_{j_n} \delta^{i_n}_{j_1} m^{(0)}\big(g_1^{\lambda_1}, \ldots, g_n^{\lambda_n}\big). \tag{27}$$

The $m^{(0)}(g_1^{\lambda_1}, \ldots, g_n^{\lambda_n})$ are ordered amplitudes with the property $m^{(0)}(1, 2, \ldots, n) = (-1)^n \times m^{(0)}(n, \ldots, 2, 1)$. From the above formulas it follows that $A^{(0)}{}_{j_1 \cdots j_n}^{i_1 \cdots i_n} = A^{(0)}{}_{i_1 \cdots i_n}^{j_1 \cdots j_n}$. By choosing the explicit momentum, helicity and color $(ij)_m$ of each gluon we can compare the numerical values of Eqs. (26) and (27). We have done the comparison for up to $2 \to 12$ gluon amplitudes and found complete agreement, thereby validating the correctness of the color-dressed algorithm.

An important consideration in calculating the color-dressed amplitudes is the color-sampling method used in the Monte Carlo program. For a $2 \to n - 2$ gluon scattering amplitude, each of the gluon color states is stochastically chosen. The full color configuration of the event is expressed by $\{(ij)_m\}_{m=1}^n$ where i_m and j_m each denote a color state out of three possible ones that can be labelled $\{1, 2, 3\}$. In the "Naive" approach one samples uniformly over all possible color states of the gluons. The number of color configurations, $N_{\text{col}}^{\text{Naive}}$, and the color-configuration weight, $W_{\text{col}}^{\text{Naive}}$, are given by

$$N_{\text{col}}^{\text{Naive}} = 9^n \tag{28}$$

and

$$W_{\text{col}}^{\text{Naive}} = 1, \tag{29}$$

respectively. About 95% of these naive color configurations have vanishing color factors. This results in a rather inefficient Monte Carlo procedure when sampling over the color states. As was noted in Ref. [32], a significant number of the zero color-weight configurations can be removed by imposing color conservation. This is implemented by vetoing any color configuration for which the condition $\exists c \in \{1, 2, 3\}: \sum_{m=1}^n (\delta_{i_m,c} - \delta_{j_m,c}) \neq 0$ is true. In other words, the non-vetoed color configurations can be obtained by uniformly choosing the colors $i_1, \ldots, i_n$ and subsequently generating the colors $j_1, \ldots, j_n$ through a permutation of the list $\{i_1, \ldots, i_n\}$. For the number of color configurations to be sampled over, this approach, which we name "Conserved" in what follows, then yields

$$N_{\text{col}}^{\text{Conserved}} = \sum_{n_1,n_2,n_3=0}^n \delta_{n_1+n_2+n_3,n} \left(\frac{n!}{n_1! n_2! n_3!} \right)^2 \tag{30}$$

where $n_c = \sum_{m=1}^n \delta_{i_m,c}$. As this way of sampling is no longer uniform, each generated color configuration gets an associated color weight described by

$$W_{\text{col}}^{\text{Conserved}} = 3^n \frac{n!}{n_1! n_2! n_3!}. \tag{31}$$

Yet, there still are non-contributing color configurations left in the sampling set. We have to augment the selection criteria further by vetoing any color configuration for which the condition $\exists c \in \{1, 2, 3\}: [\forall m \in \{1, 2, \ldots, n\}: (i_m = c \to i_m = j_m)]$ is true.[4] In other words, we veto a color configuration if *all* occurrences of a particular color c come paired: $i_m = j_m = c$. By adding this veto to the "Conserved" generation, we obtain the "Non-Zero" Monte Carlo procedure that has removed *all* color configurations with zero color weight. The number of leftover configurations sampled over is given by

---

[4] When all colors are identical, i.e. $i_1 = j_1 = i_2 = j_2 = \cdots = i_n = j_n$, every color factor in Eq. (27) is equal to one. We can still veto the event because the sum over all ordered amplitudes is identical to zero at tree level [26].

Table 1
The number of color configurations sampled over when using the different Monte Carlo color schemes.

Scattering	Naive	Conserved	Non-Zero
$2 \to 2$	6561	639	378
$2 \to 3$	59,049	4653	3180
$2 \to 4$	531,441	35,169	27,240
$2 \to 5$	4,782,969	272,835	231,672
$2 \to 6$	43,046,721	2,157,759	1,949,178
$2 \to 7$	387,420,489	17,319,837	16,279,212
$2 \to 8$	3,486,784,401	140,668,065	135,526,716

$$N_{\text{col}}^{\text{Non-Zero}} = \sum_{n_1,n_2,n_3=0}^{n} \delta_{n_1+n_2+n_3,n} \left(\frac{n!}{n_1!n_2!n_3!} \right)$$
$$\times \left(\frac{n! - n_1!n_2!n_3![1 - \sum_c \Theta(n_c-1)] - \sum_c \Theta(n_c-1)n_c!(n-n_c)!}{n_1!n_2!n_3!} \right), \tag{32}$$

where the step function $\Theta(x) = 1$ for $x \geqslant 0$ and zero otherwise. The weight associated with each sampled color configuration has to be modified and reads

$$W_{\text{col}}^{\text{Non-Zero}} = \left(3^n - 3\right) \left(\frac{n! - n_1!n_2!n_3![1 - \sum_c \Theta(n_c-1)] - \sum_c \theta(n_c-1)n_c!(n-n_c)!}{n_1!n_2!n_3!} \right). \tag{33}$$

For up to 10-gluon scatterings, Table 1 displays the resulting number of sampled color configurations in the column indicated "Non-Zero". It is also shown how this number compares to the numbers found for the "Conserved" and "Naive" sampling scheme.

Next we examine the execution time of n-gluon scattering amplitudes using the "Non-Zero" color sampling. In Table 2 the CPU time needed to calculate the color-dressed amplitudes according to Eqs. (26) and (27) are compared.

The evaluation of Eq. (27) employs the ordered recursion relation [26]. Naively one would expect this evaluation to grow factorially with the number of gluons. However this growth is considerably dampened by sampling over non-zero color configurations only. Note that for a given event we calculate each ordered amplitude with non-vanishing color factor independently of the other ordered amplitudes. One can speed up the computation time by sharing the calculated sub-currents between different orderings. This, however, is outside the scope of this paper.

For the evaluation of Eq. (26) we use the color-dressed recursion relation of Eq. (25). To study its time behavior we apply this recursion as discussed in Appendix B with and without the 4-gluon vertex. As can be seen from Table 2, the required CPU times scales as 4^n or 3^n if the 4-gluon vertex is neglected. This exponential scaling was derived in Refs. [30,6,32]. The derivation, following [32], uses the recursive buildup of the amplitude. To calculate an n-particle amplitude using a V-point vertex, we have to evaluate the $(n-1)$-particle current of Eq. (6). This current in turn is determined by calculating all $\binom{n-1}{m}$ m-particle sub-currents, where $n-1 \geqslant m \geqslant 2$. Each m-current is constructed from smaller currents using Eq. (11) thereby employing the V-point vertex. All possible partitions into $V - 1$ sub-currents are given by the Stirling number of the second kind, $\mathcal{S}_2(m, V-1)$. This leads to the following scaling of the calculation of the n-particle amplitude

Table 2

The time (in seconds) to evaluate 10,000 color-dressed tree-level amplitudes for $2 \to n - 2$ gluon scatterings. Only color configurations with non-zero weight are taken into account. Also indicated is the growth factor (given in brackets) with increasing n. To compute the amplitudes, a 2.20 GHz Intel Core2 Duo processor was used.

Scattering	Color-ordered	Color-dressed $(V_{\max} = 4)$	Color-dressed $(V_{\max} = 3)$
$2 \to 2$	0.0313	0.117	0.083
$2 \to 3$	0.169 (5.40)	0.495 (4.24)	0.327 (3.93)
$2 \to 4$	0.791 (4.68)	1.556 (3.14)	0.822 (2.51)
$2 \to 5$	3.706 (4.69)	6.11 (3.93)	2.66 (3.23)
$2 \to 6$	17.83 (4.81)	25.26 (4.13)	7.55 (2.84)
$2 \to 7$	99.79 (5.60)	93.43 (3.70)	24.9 (3.30)
$2 \to 8$	557.9 (5.59)	392.4 (4.20)	76.1 (3.05)
$2 \to 9$	2979 (5.34)	1528 (3.89)	228 (2.99)
$2 \to 10$	19,506 (6.55)	5996 (3.92)	693 (3.04)
$2 \to 11$	118,635 (6.08)	24,821 (4.14)	
$\vdots$		$\vdots$	
$2 \to 15$		6,248,300 (3.98^4)	

$$T_n = \sum_{m=2}^{n-1} \binom{n-1}{m} \mathcal{S}_2(m, V - 1) = \mathcal{S}_2(n, V) \sim V^n. \tag{34}$$

Consequently, the n-gluon amplitude using the standard 3-gluon and 4-gluon vertex has an exponential scaling behavior $T_n \to 4^n$. This is evident from the results shown in Table 2. As can also be seen in the table, the scaling behaves as expected when the 4-gluon vertex is left out, i.e. $T_n \to 3^n$. As was shown in Refs. [31,32], the 4-gluon vertex can be avoided and replaced by an effective 3-point vertex. This results in a significant time gain for the evaluation of high multiplicity gluon scattering amplitudes.

An important consideration in the usefulness of the color-sampling approach is the convergence to the correct answer as a function of the Monte Carlo sampling size N_{MC}. To this end, we compare the phase-space integration performances for the two different cases of using (i) the color-sampled result $S_{\mathrm{MC}}^{(0)}$ for the tree-level amplitude squared,

$$S_{\mathrm{MC},r}^{(0)} = W_{\mathrm{col}}(n_1, n_2, n_3) \times \left| \mathcal{M}^{(0)}\left(\mathbf{g}_1^{(r)}, \ldots, \mathbf{g}_n^{(r)}\right) \right|^2, \tag{35}$$

and (ii) the color-summed, i.e. color-exact, result

$$S_{\mathrm{col},r}^{(0)} = \sum_{i_1,\ldots,i_n=1}^{3} \sum_{j_1,\ldots,j_n=1}^{3} \left| \mathcal{M}^{(0)}\left(\mathbf{g}_1^{(r)}, \ldots, \mathbf{g}_n^{(r)}\right) \right|^2. \tag{36}$$

In both approaches the average values are computed via

$$\langle S^{(0)} \rangle = \frac{1}{N_{\mathrm{MC}}} \sum_{r=1}^{N_{\mathrm{MC}}} S_r^{(0)} \tag{37}$$

where the index r numbers the different events with the only exception that the gluon polarizations have been held fixed: $\lambda_1, \ldots, \lambda_n = + - \cdots + -(+)$. The standard deviation of each average is calculated by
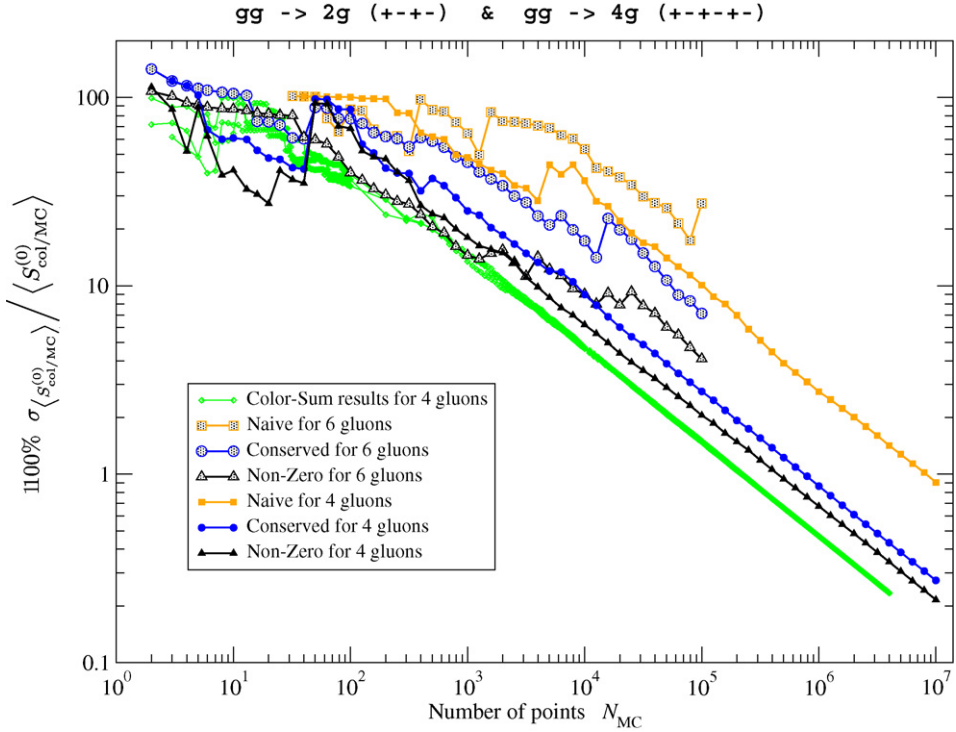
Fig. 3. The relative errors of the Monte Carlo phase-space integrations of color-summed and color-sampled 4- and 6-gluon matrix elements at the tree level. The errors are shown as a function of the number of generated flat phase-space points. For the applied phase-space cuts, see the text.

$$\sigma_{\langle S^{(0)} \rangle} = \frac{\sqrt{\sum_{r=1}^{N_{\mathrm{MC}}} (S_r^{(0)})^2 - N_{\mathrm{MC}} \langle S^{(0)} \rangle^2}}{N_{\mathrm{MC}} - 1}. \tag{38}$$

The phase-space points have been distributed uniformly (by means of the Rambo algorithm) and were subject to the constraints: $p_{\perp,m} > 0.1\sqrt{s}$, $|\eta_m| < 2$ and $\Delta R_{ml} > 0.7$, see also Eq. (65). In Fig. 3 we show the relative errors $\sigma_{\langle S^{(0)} \rangle}/\langle S^{(0)} \rangle$ of the color-sampled and color-summed Monte Carlo integrations for the 4- and 6-gluon scattering examples as a function of the number of generated phase-space points N_{MC}. The behavior for large N_{MC} may be approximated by a power law of the form $\alpha/N_{\mathrm{MC}}^{1/2}$. The color sampling then introduces an additional uncertainty to the pure phase-space integration resulting in larger α-factors. The magnitude of the additional error depends on which color-sampling scheme has been employed. For the "Conserved" scheme, we find this error to be of the order of the pure phase-space integration error. The discontinuities in the presented error curves are a feature of the flat phase-space integration; they occur because the randomly picked phase-space points generally come with largely fluctuating color and/or matrix-element weights. It is of course possible – however beyond the scope of this paper – to improve the integration performance by utilizing more sophisticated phase-space generators, which accommodate for the antenna structures of QCD amplitudes.

Having estimated the effect of combining color and phase-space sampling, we concentrate in the following on the discussion of the integration performances of the different color-sampling methods. We therefore plot the ratio of the average value of the color-sampled amplitude squared

and its standard deviation over the average value of the color-summed amplitude squared as a function of the number of Monte Carlo events:

$$R = \frac{\langle S_{\mathrm{MC}}^{(0)} \rangle \pm \sigma_{\langle S_{\mathrm{MC}}^{(0)} \rangle}}{\langle S_{\mathrm{col}}^{(0)} \rangle}. \tag{39}$$

We define the ratio this way so that most of the phase-space integration fluctuations may divide out. The normalization as given by the average color-summed result then implies a target value of $R = 1$ for large N_{MC}. If we want to estimate the total relative uncertainty on R (or more exactly on $\langle S_{\mathrm{MC}}^{(0)} \rangle / \langle S_{\mathrm{col}}^{(0)} \rangle$), we have to add the relative errors $\sigma_{\langle S_{\mathrm{MC}}^{(0)} \rangle} / \langle S_{\mathrm{MC}}^{(0)} \rangle$ and $\sigma_{\langle S_{\mathrm{col}}^{(0)} \rangle} / \langle S_{\mathrm{col}}^{(0)} \rangle$, because the average of the color-summed matrix elements is determined after N_{MC} phase-space points along with the average of the color-sampled squared amplitudes. The 4- and 6-gluon scattering results for the R-ratio as defined in Eq. (39) are presented in the respective upper parts of Figs. 4 and 5 for the three different sampling methods "Naive", "Conserved" and "Non-Zero". As it can be seen from the two plots by avoiding to sample over zero-weight color configurations the convergence can be greatly enhanced. Note that in these plots we do not show the pure phase-space integration errors of the color-summed results, as we wish to emphasize the differences in the color-sampling schemes.

For $N_{\mathrm{MC}} = \mathcal{O}(10^5)$, we obtain sufficient accuracy in the "Non-Zero" sampling method. To illustrate this more clearly, we show in the lower panels of Figs. 4 and 5 as well as in Fig. 6 the number of Monte Carlo events needed to achieve a certain relative precision in the color sampling. For these plots, we generate N_{event} events, which are partitioned into trial and sampling events via $N_{\mathrm{event}} = N_{\mathrm{trial}} \times N_{\mathrm{MC}}$. We define as a function of N_{MC} the ratio

$$R_{\mathrm{MC}}(N_{\mathrm{MC}}) = \frac{\sum_{r=1}^{N_{\mathrm{MC}}} S_{\mathrm{MC},r}^{(0)}}{\sum_{r=1}^{N_{\mathrm{MC}}} S_{\mathrm{col},r}^{(0)}} = \frac{\langle S_{\mathrm{MC}}^{(0)} \rangle (N_{\mathrm{MC}})}{\langle S_{\mathrm{col}}^{(0)} \rangle (N_{\mathrm{MC}})} \tag{40}$$

and plot N_{MC} versus the relative precision $\sigma(R_{\mathrm{MC}})/\mu(R_{\mathrm{MC}})$. The mean value

$$\mu(R_{\mathrm{MC}}) = \frac{1}{N_{\mathrm{trial}}} \sum_{k=1}^{N_{\mathrm{trial}}} R_{\mathrm{MC},k}(N_{\mathrm{MC}}) \tag{41}$$

and the standard deviation

$$\sigma(R_{\mathrm{MC}}) = \sqrt{\frac{\sum_{k=1}^{N_{\mathrm{trial}}} (R_{\mathrm{MC},k}(N_{\mathrm{MC}}))^2 - N_{\mathrm{trial}} \mu^2(R_{\mathrm{MC}})}{N_{\mathrm{trial}} - 1}} \tag{42}$$

are computed by using a sufficiently large number of trials, i.e. N_{trial} estimates of $R_{\mathrm{MC}}(N_{\mathrm{MC}})$ are calculated to obtain the mean value and the standard deviation for R_{MC}. For $N_{\mathrm{trial}} > \mathcal{O}(100)$, we get rather smooth curves. In the 4-gluon case shown in the lower part of Fig. 4 this gives a reasonable description for $N_{\mathrm{MC}} < 10^5$. The 6- and 8-gluon scatterings are more involved and require more statistics. The trend however can be read off the respective plots in Figs. 5 and 6.

For sufficiently large N_{MC}, the expected scaling of the relative standard deviation σ with the number of Monte Carlo events is $\sigma(R_{\mathrm{MC}}) \sim 1/\sqrt{N_{\mathrm{MC}}}$. As can be seen from the second plot of Fig. 4 the scaling is as expected and we can fit to the functional form $A \times N_{\mathrm{MC}}^{-B}$. In the 4-gluon case, we find

$$\text{Naive:} \quad \frac{\sigma(R_{\mathrm{MC}})}{\mu(R_{\mathrm{MC}})} = 33.8 \times N_{\mathrm{MC}}^{-0.529},$$
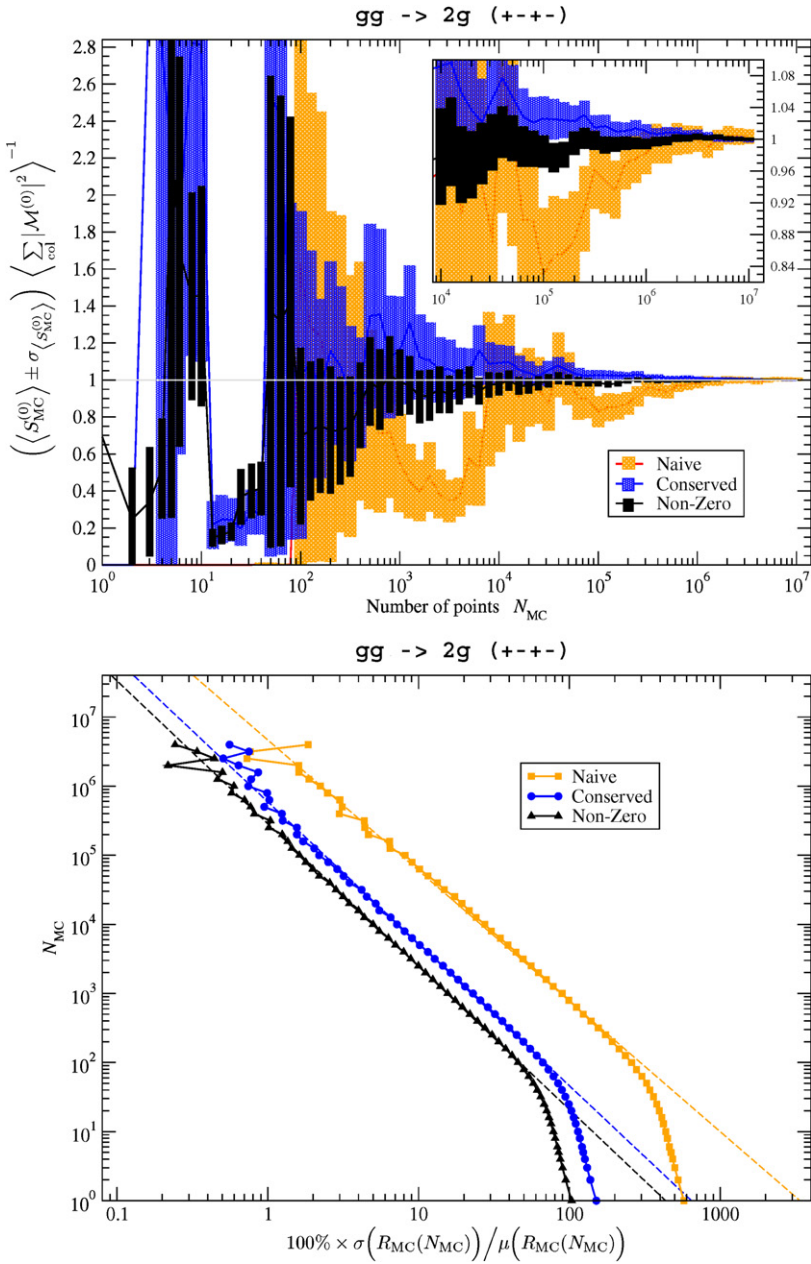
Fig. 4. Top panel: comparison of Monte Carlo integrations, including the standard deviations, for various color-sampling schemes shown as a function of the number of evaluated phase-space points and normalized to the exact color-summed result. Adding the error on the color-summed result, one obtains after 10^7 steps $\langle S_{\mathrm{MC}}^{(0)} \rangle / \langle S_{\mathrm{col}}^{(0)} \rangle = 1.0034 \pm 0.0091(\mathrm{MC}) \pm 0.0015(\mathrm{col})$, $0.9989 \pm 0.0027(\mathrm{MC}) \pm 0.0015(\mathrm{col})$ and $0.9999 \pm 0.0022(\mathrm{MC}) \pm 0.0014(\mathrm{col})$ for the "Naive", "Conserved" and "Non-Zero" sampling, respectively. Bottom panel: number of events required to reach a given relative accuracy on the numerical evaluation of the color-sampled amplitude. For the definition of $R_{\mathrm{MC}}(N_{\mathrm{MC}})$ and the parameters of the dashed fit curves, cf. the text.
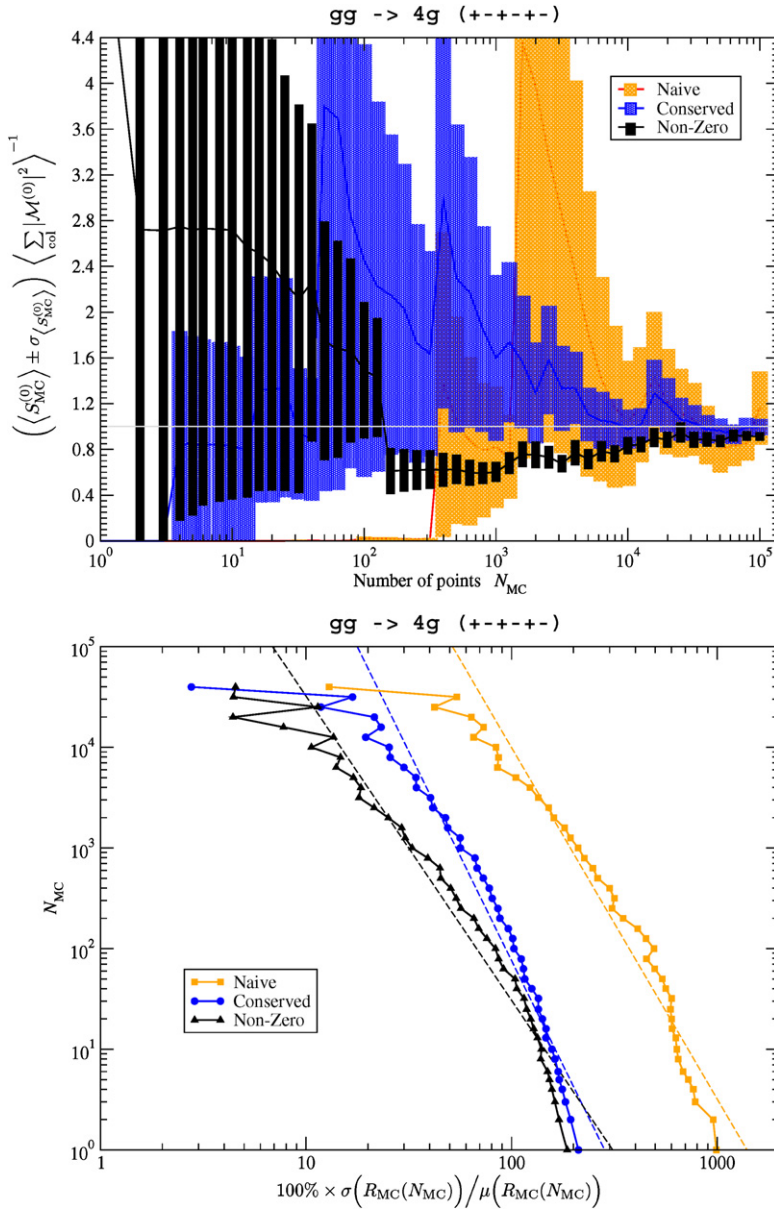
Fig. 5. Top panel: comparison of Monte Carlo integrations, plus their standard deviations, for various color-sampling schemes shown as a function of the number of evaluated phase-space points and normalized to the exact color-summed result. Including the errors on the color-summed results, one obtains after 10^5 steps $\langle S_{MC}^{(0)} \rangle / \langle S_{col}^{(0)} \rangle = 1.16 \pm 0.32(MC) \pm 0.04(col)$, $0.995 \pm 0.071(MC) \pm 0.039(col)$ and $0.913 \pm 0.037(MC) \pm 0.026(col)$ for the "Naive", "Conserved" and "Non-Zero" sampling, respectively. Bottom panel: required number of events to reach a given relative accuracy on the numerical evaluation of the color-sampled amplitude. For the definition of $R_{MC}(N_{MC})$, cf. the text. The fit curves $\sigma/\mu = f(N_{MC})$ are described by $14.0 N_{MC}^{-0.287}$, $2.84 N_{MC}^{-0.241}$ and $3.10 N_{MC}^{-0.331}$ for the "Naive", "Conserved" and "Non-Zero" sampling, respectively. In terms of computer time the latter two schemes run slower than the "Naive" scheme by factors of $f = 10.5$ and $f = 13.3$ (see text).
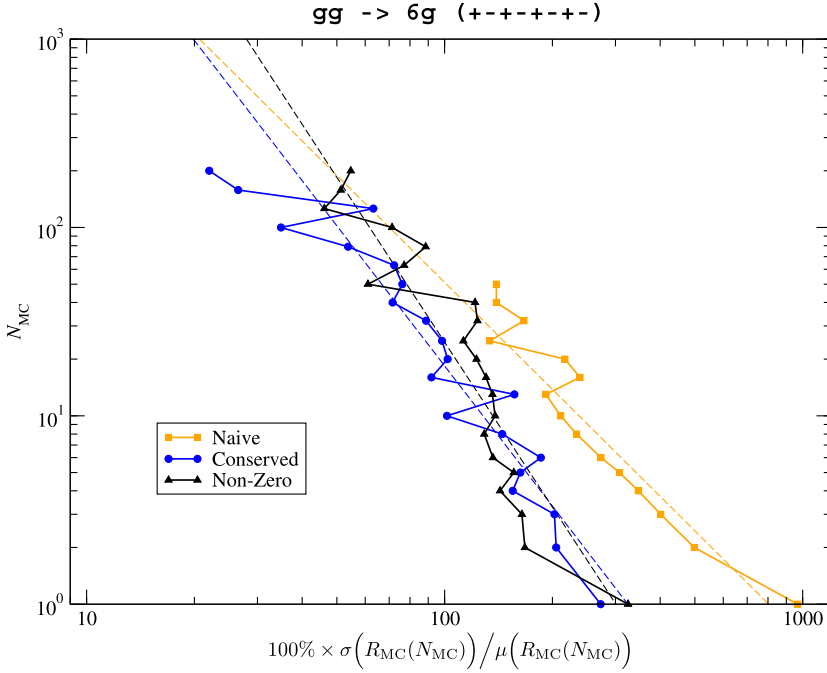
Fig. 6. Number of events required to reach a given relative accuracy on the numerical evaluation of the color-sampled amplitude. For the definition of $R_{MC}(N_{MC})$, cf. the text. The fit curves $\sigma/\mu = f(N_{MC})$ are described by $8.04 N_{MC}^{-0.530}$, $3.25 N_{MC}^{-0.405}$ and $3.01 N_{MC}^{-0.344}$ for the "Naive", "Conserved" and "Non-Zero" sampling, respectively. The computer times for the "Conserved" and "Non-Zero" approaches are larger with respect to the "Naive" sampling method by factors of $f = 9.6$ and $f = 10.8$, respectively (see text).

$$\text{Conserved:} \quad \frac{\sigma(R_{MC})}{\mu(R_{MC})} = 6.45 \times N_{MC}^{-0.487},$$

$$\text{Non-Zero:} \quad \frac{\sigma(R_{MC})}{\mu(R_{MC})} = 4.35 \times N_{MC}^{-0.484}. \tag{43}$$

From these fits we can quantify the enhancements owing to the sampling strategies. The "Conserved" sampling method improves over the "Naive" method by a factor of $33.8/6.45 = 5.2$, while the improvement of the "Non-Zero" method over the "Conserved" method yields an additional factor of $6.45/4.35 = 1.5$ (or a factor of $33.8/4.35 = 7.8$ over the "Naive" method). The algorithm determines the color configurations with vanishing color factor before it fully evaluates the corresponding matrix-element weight. The differences between the various sampling methods therefore become smaller when we measure the computer evaluation time to reach a certain relative precision. When we express this in numbers for the example of 4-gluon scattering, we notice that the "Conserved" and "Non-Zero" sampling schemes are slower than the "Naive" sampling by factors of $f = 2.42$ and $f = 3.29$, respectively. This translates into changing the fit parameter $A \rightarrow A' = A f^B$. The corresponding ratios then read $33.8/9.92 = 3.4$ and $9.92/7.74 = 1.3$ when specifying the improvement of the "Conserved" versus the "Naive" and the "Non-Zero" versus the "Conserved" method, respectively. We see using improved sampling over color configurations is still highly preferred.

4. Dressed generalized unitarity for virtual corrections

By using the parametric integration method of Ref. [12] one can implement the generalized unitarity method of Ref. [10] into an efficient algorithmic solution [44]. For the evaluation of color-ordered amplitudes, the algorithm is of polynomial complexity [29]. To calculate the dimensional regulated one-loop amplitude we extend the parametric expressions to D dimensions and apply the cuts in several integer dimensions to determine all the parametric coefficients [13].[5] The algorithm is equally applicable for the inclusion of massive quarks [48]. The power of this algorithmic solution was demonstrated in Refs. [46,47,37] for pure gluonic scattering.

Given the fully specified external sources and interaction vertices, both real and virtual corrections can be evaluated by the recursive formulas. The virtual corrections to the differential cross section are given by

$$d\sigma^{(V)}(f_1 f_2 \to f_3 \cdots f_n) = \frac{W_S}{N_{\text{event}}} \times \sum_{r=1}^{N_{\text{event}}} dPS^{(r)}(K_1 K_2 \to K_3 \cdots K_n)$$
$$\times 2\Re\big(\mathcal{M}^{(0)}\big(\mathbf{f}_1^{(r)}, \ldots, \mathbf{f}_n^{(r)}\big)^\dagger \times \mathcal{M}^{(1)}\big(\mathbf{f}_1^{(r)}, \ldots, \mathbf{f}_n^{(r)}\big)\big), \quad (44)$$

where the external sources, including momenta and quantum numbers, are sampled through a Monte Carlo procedure. The weight W_S is determined by process dependent symmetry factors and sampling weights.

In this section we show how to use the color-dressed tree-level amplitudes discussed in the previous section to construct the color-dressed one-loop amplitudes. By color sampling over the external partons one can calculate the virtual corrections using Eq. (44). The generic algorithm will be outlined and applied to pure gluon scattering.

4.1. Generic color-dressed generalized unitarity

The one-loop amplitude $\mathcal{M}^{(1)}(\mathbf{f}_1, \ldots, \mathbf{f}_n)$ is obtained by integrating the un-integrated amplitude denoted by $\mathcal{A}^{(1)}(\mathbf{f}_1, \ldots, \mathbf{f}_n \mid \ell)$ over the loop momentum ℓ:

$$\mathcal{M}^{(1)}(\mathbf{f}_1, \ldots, \mathbf{f}_n) = \int \frac{d^D \ell}{(2\pi)^D} \mathcal{A}^{(1)}(\mathbf{f}_1, \ldots, \mathbf{f}_n \mid \ell). \quad (45)$$

The integrand function can be decomposed into a sum of a finite number of rational functions of the loop momentum with loop independent coefficients [12]. The coefficients can be calculated in terms of tree-level amplitudes.

The parametric form of the integrand is given by the triple sum of rational functions,

$$\mathcal{A}^{(1)}(\mathbf{f}_1, \ldots, \mathbf{f}_n \mid \ell) = \sum_{k=1}^{C_{\max}} \sum_{RP_{\pi_1 \cdots \pi_k}(1,2,\ldots,n)}^{\max(1, \frac{1}{2}(k-1)!)\mathcal{S}_2(n,k)} \sum_{g_{\Pi_1}, \ldots, g_{\Pi_k}} \frac{\mathcal{P}_k(\vec{C}_{g_{\Pi_1} \cdots g_{\Pi_k}} \mid \ell)}{d_{g_{\Pi_1}}(\ell) d_{g_{\Pi_2}}(\ell) \cdots d_{g_{\Pi_k}}(\ell)}, \quad (46)$$

where the sum over the propagator flavors $g_{\Pi_1}, \ldots, g_{\Pi_k}$ is required as these are not uniquely defined for unordered amplitudes. The first sum includes all basic denominator structures that

---

[5] If one uses an analytical implementation of the D-dimensional unitarity method of Ref. [13], one can eliminate the penta-cuts [45]. However, in numerical implementations the removal of the penta-cuts requires performing a numerical contour integral in the complex plane [14].
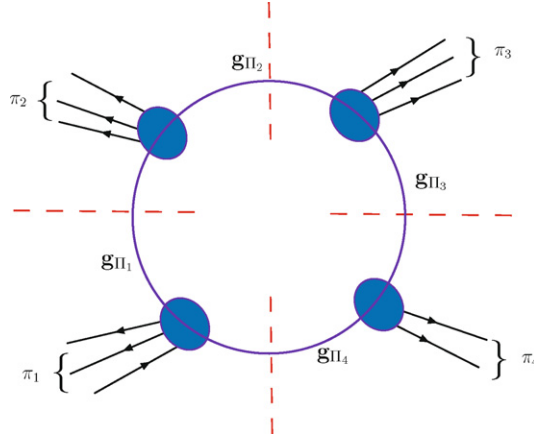
Fig. 7. Graphical representation of a quadrupole-cut partitioning of the external legs into an ordered set of four unordered subsets $\pi_1, \pi_2, \pi_3, \pi_4$ of external particles. The corresponding tree-level diagrams are connected with the propagators of particle $g_{\Pi_1}, g_{\Pi_2}, g_{\Pi_3}$ and g_{Π_4}.

occur in the decomposition of the integrand while the second sum runs over all different cuts related to a specific number k of denominators. In the most general case, i.e. when dealing with massive internal particles, tadpole contribution ($k = 1$) have to be included. The maximum number of denominators needed to describe the dimensional regulated one-loop matrix element is $C_{\max}$. The value of $C_{\max}$ is given by the dimensionality of the loop momentum. For the one-loop calculations in dimensional regularization the maximum dimension of the loop momentum is equal to five, i.e. $C_{\max} = 5$. The denominator terms are defined as

$$d_{g_{\Pi_m}}(\ell) = (\ell + K_{\Pi_m})^2 - m_g^2 \tag{47}$$

where m_g denotes the mass of the internal particle and Π_m is given through Eq. (9). The partition sum is over $RP_{\pi_1 \cdots \pi_k}(1, 2, \ldots, n)$ ($\supseteq P_{\pi_1 \cdots \pi_k}(1, 2, \ldots, n)$) elements. The total number of elements is given by $\max(1, \frac{1}{2}(k-1)!) \times \mathcal{S}_2(n, k)$. This extended partition list now also includes non-cyclic and non-reflective permutations over the regular partition lists $\{\{\pi_i\}_{i=1}^k\}$; more specifically we have:

$$RP_{\pi_1 \pi_2} = \{P_{\pi_1 \pi_2}\},$$
$$RP_{\pi_1 \pi_2 \pi_3} = \{P_{\pi_1 \pi_2 \pi_3}\},$$
$$RP_{\pi_1 \pi_2 \pi_3 \pi_4} = \{P_{\pi_1 \pi_2 \pi_3 \pi_4}, P_{\pi_1 \pi_3 \pi_4 \pi_2}, P_{\pi_1 \pi_4 \pi_2 \pi_3}\},$$
$$RP_{\pi_1 \pi_2 \pi_3 \pi_4 \pi_5} = \{P_{\pi_1 \pi_2 \pi_3 \pi_4 \pi_5}, P_{\pi_1 \pi_3 \pi_4 \pi_5 \pi_2}, P_{\pi_1 \pi_4 \pi_5 \pi_2 \pi_3}, P_{\pi_1 \pi_5 \pi_2 \pi_3 \pi_4},$$
$$\qquad\qquad P_{\pi_1 \pi_2 \pi_4 \pi_5 \pi_3}, P_{\pi_1 \pi_4 \pi_5 \pi_3 \pi_2}, P_{\pi_1 \pi_5 \pi_3 \pi_2 \pi_4}, P_{\pi_1 \pi_3 \pi_2 \pi_4 \pi_5},$$
$$\qquad\qquad P_{\pi_1 \pi_2 \pi_5 \pi_3 \pi_4}, P_{\pi_1 \pi_5 \pi_3 \pi_4 \pi_2}, P_{\pi_1 \pi_3 \pi_4 \pi_2 \pi_5}, P_{\pi_1 \pi_4 \pi_2 \pi_5 \pi_3}\}. \tag{48}$$

The polynomial dependence of the numerator functions $\mathcal{P}_k$ on the loop momentum is specified with a vector of parametric coefficients $\vec{C}_{g_{\Pi_1} \cdots g_{\Pi_k}}$. The explicit polynomial forms that we are using are given in Ref. [13]. The dimensionality of the parameter vector $\vec{C}_{g_{\Pi_1} \cdots g_{\Pi_k}}$ depends on the number of denominators. In the case of 5 denominators there is only one parameter, for the terms with 4 denominators we have five parameters, etc. The parameters are determined by

putting sets of denominators to zero and calculating the residue in terms of tree-level amplitudes. Setting denominator factors to zero is on a par with cutting the corresponding propagators as required by generalized D-dimensional unitarity. Let $\ell_{\Pi_1\cdots\Pi_c}$ be the "on-shell" loop momentum fulfilling the "unitarity condition":

$$d_{g_{\Pi_1}}(\ell_{\Pi_1\cdots\Pi_c}) = \cdots = d_{g_{\Pi_c}}(\ell_{\Pi_1\cdots\Pi_c}) = 0; \quad c = 1, \ldots, C_{\max}. \tag{49}$$

To fulfill the unitarity conditions we allow also complex values for the components of the loop momenta. The parametric form of the numerator functions for c-cuts becomes

$$
\begin{aligned}
\mathcal{P}_c(\vec{C}_{g_{\Pi_1}\cdots g_{\Pi_c}} \mid \ell_{\Pi_1\cdots\Pi_c}) = {}& \mathrm{Res}_{g_{\Pi_1}\cdots g_{\Pi_c}}\left(\mathcal{A}^{(1)}(\mathbf{f}_1,\ldots,\mathbf{f}_n \mid \ell_{\Pi_1\cdots\Pi_c})\right) \\
& - \sum_{m=c+1}^{C_{\max}} \sum_{PP_{\widehat{\pi}_1,\ldots,\widehat{\pi}_m}(1,\ldots,n)} \delta_{\Pi_1\widehat{\Pi}_1}\cdots\delta_{\Pi_c\widehat{\Pi}_c} \\
& \times \sum_{g_{\widehat{\Pi}_{c+1}}\cdots g_{\widehat{\Pi}_m}} \frac{\mathcal{P}_m(\vec{C}_{g_{\widehat{\Pi}_1}\cdots g_{\widehat{\Pi}_m}} \mid \widehat{\ell}_{\widehat{\Pi}_1\cdots\widehat{\Pi}_c})}{d_{g_{\widehat{\Pi}_{c+1}}}(\widehat{\ell}_{\widehat{\Pi}_1\cdots\widehat{\Pi}_c})\cdots d_{g_{\widehat{\Pi}_m}}(\widehat{\ell}_{\widehat{\Pi}_1\cdots\widehat{\Pi}_c})},
\end{aligned}
\tag{50}
$$

where the sum $PP_{\widehat{\pi}_1,\ldots,\widehat{\pi}_m}(1,\ldots,n)$ over all $m!$ permutations of the m partitions is supplemented with the δ-functions to generate the appropriate subtraction functions. Each individual subtraction expression has to be evaluated with the appropriate shift of the loop-momentum, such that $\ell_{\Pi_1\cdots\Pi_c} \to \widehat{\ell}_{\widehat{\Pi}_1\cdots\widehat{\Pi}_c}$. This equation provides us with an iterative procedure starting with the highest number of cuts. For a given number of cuts, the numerator function becomes the residue of the one-loop integrand function minus the known contributions of terms with a higher number of denominator factors. The residue of the one-loop integrand factorizes into a product of tree-level amplitudes (see e.g. Fig. 7):

$$
\begin{aligned}
& \mathrm{Res}_{g_{\Pi_1}\cdots g_{\Pi_c}}\left(\mathcal{A}^{(1)}(\mathbf{f}_1,\ldots,\mathbf{f}_n \mid \ell_{\Pi_1\cdots\Pi_c})\right) \\
& = \left[d_{g_{\Pi_1}}(\ell) \times \cdots \times d_{g_{\Pi_c}}(\ell) \times \mathcal{A}^{(1)}(\mathbf{f}_1,\ldots,\mathbf{f}_n \mid \ell) \right]_{\ell=\ell_{\Pi_1\cdots\Pi_c}} \\
& = \sum_{\mathbf{g}_1\cdots\mathbf{g}_c} \left\{ \prod_{k=1}^{c} \mathcal{M}^{(0)}(\mathbf{g}_k^\dagger, \mathbf{f}_{\pi_k}, \mathbf{g}_{k+1}) \right\},
\end{aligned}
\tag{51}
$$

where the index k is cyclic (i.e. $\mathbf{g}_{c+1} = \mathbf{g}_1$) and the $\mathbf{g}_k$ denote the particles resulting from the cut lines.

We can determine the parametric vector $\vec{C}_{g_{\Pi_1}\cdots g_{\Pi_c}}$ in Eq. (50) by evaluating the right-hand side for a set of loop momenta fulfilling the unitarity constraint of Eq. (49). The only physics model input is given through the tree-level on-shell amplitudes, $\mathcal{M}^{(0)}$, which we evaluate using Eqs. (6) and (11). Two of the external lines to the on-shell tree-level amplitudes are generated by the D-dimensional cut lines. These external states have in general complex, 5-dimensional momenta. This extension of the momenta does not modify the general structure of the tree-level level recursion relations discussed in the previous section. In this way we obtain a fully specified algorithm to determine the parameters and thereby the parametric form on the left-hand side of Eq. (46).

It is instructive to illustrate the structure given by Eq. (46) for a simple example. Let us consider the cut-constructible ($D = 4$) part of the box terms in 4-gluon scattering ($n = 4$, $k = 4$). In this case we have no pentagon terms and the numerator functions of the box terms are parametrized by two coefficients:

$$\sum_{RP_{1234}(1,2,3,4)} \sum_{f=\{g,q\}} \frac{\mathcal{P}_4(\vec{C}_{f_1 f_2 f_3 f_4} \mid \ell)}{d_{f_1}(\ell) d_{f_{12}}(\ell) d_{f_{123}}(\ell) d_{f_{1234}}(\ell)}$$

$$= \frac{\mathcal{P}_4(\vec{C}_{g_1 g_2 g_3 g_4} \mid \ell)}{d_{g_1}(\ell) d_{g_{12}}(\ell) d_{g_{123}}(\ell) d_{g_{1234}}(\ell)} + \frac{\mathcal{P}_4(\vec{C}_{g_1 g_3 g_4 g_2} \mid \ell)}{d_{g_1}(\ell) d_{g_{13}}(\ell) d_{g_{134}}(\ell) d_{g_{1342}}(\ell)}$$

$$+ \frac{\mathcal{P}_4(\vec{C}_{g_1 g_4 g_2 g_3} \mid \ell)}{d_{g_1}(\ell) d_{g_{14}}(\ell) d_{g_{142}}(\ell) d_{g_{1423}}(\ell)} + \frac{\mathcal{P}_4(\vec{C}_{q_1 q_2 q_3 q_4} \mid \ell)}{d_{q_1}(\ell) d_{q_{12}}(\ell) d_{q_{123}}(\ell) d_{q_{1234}}(\ell)}$$

$$+ \frac{\mathcal{P}_4(\vec{C}_{q_1 q_3 q_4 q_2} \mid \ell)}{d_{q_1}(\ell) d_{q_{13}}(\ell) d_{q_{134}}(\ell) d_{q_{1342}}(\ell)} + \frac{\mathcal{P}_4(\vec{C}_{q_1 q_4 q_2 q_3} \mid \ell)}{d_{q_1}(\ell) d_{q_{14}}(\ell) d_{q_{142}}(\ell) d_{q_{1423}}(\ell)} \qquad (52)$$

where

$$\mathcal{P}_4(\vec{C}_{f_1 f_2 f_3 f_4} \mid \ell) = C^{(0)}_{f_1 f_2 f_3 f_4} + C^{(1)}_{f_1 f_2 f_3 f_4} \times \ell \cdot n; \quad n_\mu = \epsilon_{\mu \mu_1 \mu_2 \mu_3} p_1^{\mu_1} p_{12}^{\mu_2} p_{123}^{\mu_3}. \qquad (53)$$

The parameters are calculated by using the residue formula of Eq. (51). After the coefficients of the box functions have been obtained, one turns to calculate the coefficients of the triangle contributions. The numerator function for the triangle cut of the quark-loop contribution, Eq. (50), becomes

$$\mathcal{P}_3(\vec{C}_{q_1 q_2 q_{34}} \mid \ell_{\Pi_1 \Pi_2 \Pi_{34}}) = \text{Res}_{q_1 q_2 q_{34}}\big(\mathcal{A}^{(1)}(\mathbf{g}_1, \mathbf{g}_2, \mathbf{g}_3, \mathbf{g}_4 \mid \ell_{\Pi_1 \Pi_2 \Pi_{34}})\big)$$

$$- \frac{\mathcal{P}_4(\vec{C}_{q_1 q_2 q_3 q_4} \mid \ell_{\Pi_1 \Pi_2 \Pi_{34}})}{d_{q_{123}}(\ell_{\Pi_1 \Pi_2 \Pi_{34}})} - \frac{\mathcal{P}_4(\vec{C}_{q_1 q_2 q_4 q_3} \mid \ell_{\Pi_1 \Pi_2 \Pi_{34}})}{d_{q_{124}}(\ell_{\Pi_1 \Pi_2 \Pi_{34}})}, \qquad (54)$$

where the residuum of the quark loop can be calculated again using Eq. (51),

$$\text{Res}_{q_1 q_2 q_{34}}\big(\mathcal{A}^{(1)}(\mathbf{g}_1, \mathbf{g}_2, \mathbf{g}_3, \mathbf{g}_4 \mid \ell_{\Pi_1 \Pi_2 \Pi_{34}})\big)$$

$$= \big[d_{q_1}(\ell) \times d_{q_{12}}(\ell) \times d_{q_{1234}}(\ell) \times \mathcal{A}^{(1)}(\mathbf{g}_1, \mathbf{g}_2, \mathbf{g}_3, \mathbf{g}_4 \mid \ell)\big]_{\ell=\ell_{\Pi_1 \Pi_2 \Pi_{34}}}$$

$$= \sum_{\mathbf{q}_1 \mathbf{q}_2 \mathbf{q}_3} \mathcal{M}^{(0)}(\mathbf{q}_1^\dagger, \mathbf{g}_1, \bar{\mathbf{q}}_2) \times \mathcal{M}^{(0)}(\mathbf{q}_2^\dagger, \mathbf{g}_2, \bar{\mathbf{q}}_3) \times \mathcal{M}^{(0)}(\mathbf{q}_3^\dagger, \mathbf{g}_3, \mathbf{g}_4, \bar{\mathbf{q}}_1). \qquad (55)$$

Finally, we can obtain the one-loop amplitude, Eq. (45), by integrating out the parametric forms on the right-hand side of Eq. (46) over the loop momentum. In this way one finds the master-integral decomposition of the one-loop matrix element for every specified scattering configuration point [13]:

$$\mathcal{M}^{(1)}(\mathbf{f}_1, \dots, \mathbf{f}_n) = \int \frac{d^D \ell}{(2\pi)^D} \mathcal{A}^{(1)}(\mathbf{f}_1, \dots, \mathbf{f}_n \mid \ell)$$

$$= \sum_{k=1}^{C_{\max}} \sum_{RP_{\pi_1 \cdots \pi_k}(1,2,\dots,n)} \sum_{g_{\Pi_1} \cdots g_{\Pi_k}} S_F^{(g_{\Pi_1} \cdots g_{\Pi_k})}$$

$$\times (\bar{C}_{g_{\Pi_1} \cdots g_{\Pi_k}} \mathcal{I}_{g_{\Pi_1} \cdots g_{\Pi_k}} + \bar{\bar{C}}_{g_{\Pi_1} \cdots g_{\Pi_k}} \mathcal{R}_{g_{\Pi_1} \cdots g_{\Pi_k}}) \qquad (56)$$

where $S_F^{(g_{\Pi_1} \cdots g_{\Pi_k})}$ is the loop-integral symmetry factor (e.g. for a gluonic self-energy, the symmetry factor is $\frac{1}{2}$), the $\mathcal{I}_{g_{\Pi_1} \cdots g_{\Pi_k}}$ denote the scalar master-integral functions corresponding to the generalized cut given by the ordered partition list $\{\Pi_1 \cdots \Pi_k\}$ and flavors of the cut lines

$(g_{\Pi_1} \cdots g_{\Pi_k})$. The terms $\mathcal{R}_{g_{\Pi_1} \cdots g_{\Pi_k}}$ are the leading terms of the higher dimensional scalar integrals in the limit $D \to 4$,

$$
\mathcal{R}_{f_{\Pi_1} f_{\Pi_2} f_{\Pi_3} f_{\Pi_4}} = -\frac{1}{6},
$$
$$
\mathcal{R}_{f_{\Pi_1} f_{\Pi_2} f_{\Pi_3}} = \frac{1}{2},
$$
$$
\mathcal{R}_{f_{\Pi_1} f_{\Pi_2}} = -\frac{(K_{\Pi_1} - K_{\Pi_2})^2}{6} + \frac{m_{f_{\Pi_1}}^2 + m_{f_{\Pi_2}}^2}{2},
$$
$$
\mathcal{R}_{f_{\Pi_1}} = 0. \tag{57}
$$

The scalar master integrals

$$
\mathcal{I}_{f_{\Pi_1} \cdots f_{\Pi_k}} = I_k(K_{\Pi_1}, \ldots, K_{\Pi_k}, m_{f_{\Pi_1}}, \ldots, m_{f_{\Pi_k}}), \tag{58}
$$

can be evaluated by e.g. using the numerical package developed in Ref. [50]. In Eq. (56) the coefficients $\bar{C}$ and $\bar{\bar{C}}$ are determined by applying Eqs. (50) and (51) using a numerical algorithm. The $\bar{\bar{C}}$ coefficients are generated due to the dimensional regularization procedure and are associated with the higher dimensional terms in the parametric forms.

4.2. Numerical results for the virtual corrections of n-gluon scattering

We have applied the formalism of the previous sections to multi-gluon scattering. In this case, Eq. (46) simplifies, since only gluons can occur as internal particles. Therefore, no cuts on massive propagators have to be considered, tadpole contributions vanish ($k \geqslant 2$) and the propagator flavor sum reduces to one term. Starting from these simplifications we have extended the implementation presented in Ref. [37]. Three major changes are required to alter this generalized-unitarity based algorithm (and similar ones) for the evaluation of color-ordered amplitudes to a numerical algorithm capable of calculating color-dressed one-loop amplitudes. First, in the decomposition of the one-loop integrands (cf. Eq. (3) of Ref. [37] and Eq. (46)), all sums over ordered cuts have to be replaced by sums over partitions, which include all configurations obtained by non-cyclic and non-reflective permutations:

$$
\sum_{[i_1 | i_k]} \quad \to \quad \sum_{RP_{\pi_1 \cdots \pi_k}(1 \ldots n)}. \tag{59}
$$

Note that $[i_1 | i_k] = 1 \leqslant i_1 < i_2 < \cdots < i_k \leqslant n$. Second, the tree-level amplitudes occurring in the determination of the integrand's residues have to be calculated from color-dressed recursion relations. In addition, one not only has to sum over the internal polarizations of the gluons but also over their internal colors when computing these residues. Third, gluon bubble coefficients need to be supplemented by a symmetry factor of $1/2!$. The appearance of the symmetry factor is associated with the parametrization ambiguity of the subtraction terms in the double cuts. For example, Eq. (50) gives for one of the double cuts in 4-gluon scattering

$$
\mathcal{P}_2(\vec{C}_{g_{12}g_{34}} \mid \ell) = \text{Res}_{g_{12}g_{34}}\big(\mathcal{A}^{(1)}(\mathbf{g}_1, \mathbf{g}_2, \mathbf{g}_3, \mathbf{g}_4 \mid \ell)\big)
$$
$$
- \frac{\mathcal{P}_3(\vec{C}_{g_1 g_2 g_{34}} \mid \ell)}{d_{g_1}(\ell)} - \frac{\mathcal{P}_3(\vec{C}_{g_2 g_1 g_{34}} \mid \ell)}{d_{g_2}(\ell)} - \frac{\mathcal{P}_3(\vec{C}_{g_3 g_4 g_{12}} \mid \ell)}{d_{g_3}(\ell)}
$$

$$- \frac{\mathcal{P}_3(\vec{C}_{g_4 g_3 g_{12}} \mid \ell)}{d_{g_4}(\ell)} - \frac{\mathcal{P}_4(\vec{C}_{g_1 g_2 g_3 g_4} \mid \ell)}{d_{g_1}(\ell) d_{g_{123}}(\ell)} - \frac{\mathcal{P}_4(\vec{C}_{g_2 g_1 g_3 g_4} \mid \ell)}{d_{g_2}(\ell) d_{g_{213}}(\ell)}$$

$$- \frac{\mathcal{P}_4(\vec{C}_{g_1 g_2 g_4 g_3} \mid \ell)}{d_{g_1}(\ell) d_{g_{124}}(\ell)} - \frac{\mathcal{P}_4(\vec{C}_{g_2 g_1 g_4 g_3} \mid \ell)}{d_{g_2}(\ell) d_{g_{214}}(\ell)}$$

$$= \mathrm{Res}_{g_{12} g_{34}} \big(\mathcal{A}^{(1)}(\mathbf{g}_1, \mathbf{g}_2, \mathbf{g}_3, \mathbf{g}_4 \mid \ell) \big)$$

$$- \frac{\mathcal{P}_3(\vec{C}_{g_1 g_2 g_{34}} \mid \ell)}{d_{g_1}(\ell)} - \frac{\mathcal{P}_3(\vec{C}_{g_1 g_2 g_{34}} \mid -\ell + K_1 + K_2)}{d_{g_1}(-\ell + K_1 + K_2)}$$

$$- \frac{\mathcal{P}_3(\vec{C}_{g_3 g_4 g_{12}} \mid \ell)}{d_{g_3}(\ell)} - \frac{\mathcal{P}_3(\vec{C}_{g_3 g_4 g_{12}} \mid -\ell + K_3 + K_4)}{d_{g_3}(-\ell + K_3 + K_4)}$$

$$- \frac{\mathcal{P}_4(\vec{C}_{g_1 g_2 g_3 g_4} \mid \ell)}{d_{g_1}(\ell) d_{g_{123}}(\ell)} - \frac{\mathcal{P}_4(\vec{C}_{g_1 g_2 g_3 g_4} \mid -\ell + K_1 + K_2)}{d_{g_1}(-\ell + K_1 + K_2) d_{g_{123}}(-\ell + K_1 + K_2)}$$

$$- \frac{\mathcal{P}_4(\vec{C}_{g_1 g_2 g_4 g_3} \mid \ell)}{d_{g_1}(\ell) d_{g_{124}}(\ell)} - \frac{\mathcal{P}_4(\vec{C}_{g_1 g_2 g_4 g_3} \mid -\ell + K_3 + K_4)}{d_{g_1}(-\ell + K_3 + K_4) d_{g_{124}}(-\ell + K_3 + K_4)}. \quad (60)$$

We see that each of the four possible parametrized terms is subtracted twice but with a different choice of the loop momentum. The symmetry factor of 1/2! "averages" over the double subtractions.

The results of the new formalism have been verified by applying the usual consistency checks such as solving for the master-integral coefficients with two independent sets of loop momenta. They indeed can be tested more thoroughly: for a given color configuration, the value of the double pole (dp) can easily be cross-checked against the analytic result

$$\mathcal{M}^{(1)}_{\mathrm{dp,th}} = -\frac{c_\Gamma}{\epsilon^2} n N_\mathrm{C} \mathcal{M}^{(0)}. \quad (61)$$

In principle, the single poles are also known analytically. Here, we will however use the already validated ordered algorithm of Ref. [37] to compute the full one-loop amplitude of a certain color and helicity (polarization) configuration for a given point in phase space including the singular terms. Following the color-decomposition approach, we can analytically calculate the necessary color factors and sum up all relevant orderings to obtain the full result. In particular, we have employed:

$$\mathcal{M}^{(1)}(\mathbf{g}_1, \ldots, \mathbf{g}_n)$$

$$= \sum_{P(2\cdots n)} A^{(1) \, i_1 \cdots i_n}_{ j_1 \cdots j_n} \big(g_1^{\lambda_1}, \ldots, g_n^{\lambda_n} \big)$$

$$= \sum_{P(1\cdots n-1)} \left[N_\mathrm{C} \Delta_{1\cdots n} + \sum_{k=1}^{\mathrm{int}(n/2)} \sum_{m_1=1}^{n-k+1} \cdots \sum_{m_k=m_{k-1}+1}^{n} (-1)^k \Delta_{m_1 \cdots m_k} \Delta_{1 \cdots \not{m}_1 \cdots \not{m}_k \cdots n} \right]$$

$$\times m^{(1)}(12 \cdots n) \quad (62)$$

where

$$\Delta_{12\cdots n} = \delta^{i_1}_{j_2} \delta^{i_2}_{j_3} \cdots \delta^{i_{n-1}}_{j_n} \delta^{i_n}_{j_1}. \quad (63)$$

For example,

Table 3
The number of cuts required for the calculation of one ordered n-gluon amplitude. The column labelled "total" gives the number of cuts when calculating all $(n-1)!/2$ ordered amplitudes needed to reconstruct the full virtual correction. The last two columns list the number of non-zero color-weight orderings for two special color configurations given in the text.

Ordered cuts									
# n	5-gon cuts	box cuts	triangle cuts	bubble cuts	sum	$\frac{\text{sum}_n}{\text{sum}_{n-1}}$	total = sum × #orderings	#orderings $=(n-1)!/2$	$\mathcal{N}_{(ab)_k}=$ $(n-2)!$	$\mathcal{N}_{(cd)_k}$
4	0	1	4	2	7		21	3	2	3
5	1	5	10	5	21	3.00	252	12	6	7
6	6	15	20	9	50	2.38	3000	60	24	22
7	21	35	35	14	105	2.10	37,800	360	120	40
8	56	70	56	20	202	1.92	509,040	2520	720	144
9	126	126	84	27	363	1.80	7,318,080	20,160	5040	756
10	252	210	120	35	617	1.70	111,948,480	181,440	40,320	2688
11	462	330	165	44	1001	1.62	1,816,214,400	1,814,400	362,880	
12	792	495	220	54	1561	1.56	31,155,062,400	19,958,400	3,628,800	

$$
\begin{aligned}
\mathcal{M}^{(1)}(\mathbf{g}_1, \mathbf{g}_2, \mathbf{g}_3, \mathbf{g}_4, \mathbf{g}_5) &= \sum_{P(2345)} A^{(1)}(\mathbf{g}_1, \mathbf{g}_2, \mathbf{g}_3, \mathbf{g}_4, \mathbf{g}_5) \\
&= \sum_{P(2345)} (N_C \Delta_{12345} - \Delta_1 \Delta_{2345} - \Delta_2 \Delta_{1345} - \Delta_3 \Delta_{1245} \\
&\quad - \Delta_4 \Delta_{1235} - \Delta_5 \Delta_{1234} + \Delta_{12} \Delta_{345} + \Delta_{13} \Delta_{245} + \Delta_{14} \Delta_{235} \\
&\quad + \Delta_{15} \Delta_{234} + \Delta_{23} \Delta_{145} + \Delta_{24} \Delta_{135} + \Delta_{25} \Delta_{134} + \Delta_{34} \Delta_{125} \\
&\quad + \Delta_{35} \Delta_{124} + \Delta_{45} \Delta_{123}) m^{(1)}(12345).
\end{aligned}
\tag{64}
$$

Compared to the LO color-ordered decomposition, Eq. (27), the NLO color-ordered decomposition leads to many subleading color factors. The number of one-loop ordered amplitudes with zero color weight is significantly smaller than the corresponding number for tree-level ordered amplitudes. As a result, the advantages of color dressing become more apparent at the one-loop level.

4.2.1. Cut configurations of ordered and unordered gluons

For a more quantitative understanding of the one-loop amplitude decomposition, we respectively itemize in Tables 3 and 4 how many cuts need be applied to decompose the color-ordered and color-dressed one-loop integrands for n external gluons. In both cases we separately list the numbers of pentagon, box, triangle and bubble cuts and their sum. While for the ordered cuts these numbers are basically ruled by combinatorics[6]: $\mathcal{C}(n, m) = \binom{n}{m}$ with $m = 1, \ldots, 5$; in the unordered case they are given by the Stirling numbers[7] of the second kind, $\mathcal{S}_2(n, m)$, and therefore grow more quickly with n than those of the ordered cuts. This is exemplified in the

---

[6] Note that in the pure gluonic setup tadpole cuts are absent; also bubble cuts placing a single gluon on one side of the cut lead to vanishing master integrals, hence, we only have $\mathcal{C}(n, 2) - n$ bubble cuts to deal with as shown by the table.

[7] More exactly, the number of bubble cuts is given by $2^{n-1} - 1 - n = \mathcal{S}_2(n, 2) - n$, since cuts that isolate one gluon do not contribute. For triangles, boxes and pentagons, we respectively have $(3^n - 3 \cdot 2^n + 3)/6 = \mathcal{S}_2(n, 3)$, $3\mathcal{S}_2(n, 4)$ and $12\mathcal{S}_2(n, 5)$ cuts where for the determination of the latter two, the recurrence relation $\mathcal{S}_2(n, m) = \mathcal{S}_2(n - 1, m - 1) + m\mathcal{S}_2(n - 1, m)$ is of help.

Table 4

The number of cuts needed to calculate color-dressed n-gluon amplitudes. The last three columns give ratios of total numbers of cuts required to compute the virtual corrections in both the color-decomposition and color-dressed approaches. The first of these columns shows the ratios for all generic color orderings whereas the other columns show the ratios for two specific configurations as given in the text.

Unordered cuts								
#	pentagon	box	triangle	bubble	sum	$\frac{sum_n}{sum_{n-1}}$	ordr total/unordr total		
n	cuts	cuts	cuts	cuts	$\equiv$ total		orderings	$(ab)_k$	$(cd)_k$
4	0	3	6	3	12		1.750	1.167	1.750
5	12	30	25	10	77	6.42	3.273	1.636	1.909
6	180	195	90	25	490	6.36	6.122	2.449	2.245
7	1680	1050	301	56	3087	6.30	12.24	4.082	1.361
8	12,600	5103	966	119	18,788	6.09	27.09	7.741	1.548
9	83,412	23,310	3025	246	109,993	5.85	66.53	16.63	2.495
10	510,300	102,315	9330	501	622,446	5.66	179.9	39.97	2.664
11	2,960,760	437,250	28,501	1012	3,427,523	5.51	529.9	106.0	
12	16,552,800	1,834,503	86,526	2035	18,475,864	5.39	1686	306.6	

"sum_n/sum_{n-1}" columns of the two tables. The growth factors slowly decrease for larger n, approaching the limit of 5 for the color-dressed case. As emphasized in Table 4 the pentagon-cut calculations dominate in this case over all other cut evaluations. The large-n growth of the total cut number is hence described by that of $\mathcal{S}_2(n, 5)$ leading to the observed large-n scaling of 5^n. Using the color-decomposition approach, we have to deal with much fewer cuts per ordering. However, the total number of ordered cuts is obtained only after multiplying with the relevant number of orderings. When considering all possible $(n-1)!/2$ orderings, the final numbers are given in column "total" of Table 3. The last three columns show the number of generic orderings and the numbers $\mathcal{N}$ of non-vanishing orderings (i.e. those having non-zero color factors) for two color configurations $(ab)_k \equiv (13)(31)(11)\ldots(11)$ and $(cd)_k \equiv (22)(12)(23)(31)(11)(22)(33)(11)(22)\ldots$.[8] Of course, for a fair comparison between the ordered and dressed approach, the latter two columns are of higher interest, since zero color weights are not counted. Still, the ratios of total numbers of ordered versus unordered cuts is always larger than one as can be read off the last three columns of Table 4. Keeping in mind the greater cost of evaluating dressed recursion relations, the color-decomposition approach can be expected to outperform the dressed method as long as these ratios remain of order $\mathcal{O}(1)$. This in particular is true for simple color configurations such as $(cd)_k$.

4.2.2. General test setup

The analytic knowledge of $\mathcal{M}^{(1)}(\mathbf{g}_1, \ldots, \mathbf{g}_n)$ presented in Eq. (62) enables us to perform stringent tests of our algorithm and its implementation. We consider $2 \to n-2$ processes where the gluons have possible polarization states $\lambda_k \in \{+, -\}$ and colors $(ij)_k$ where $i_k, j_k \in \{1, 2, 3\}$ and $k = 1, \ldots, n$, i.e. we make use of the color-flow notation. Our n-gluon results are given in the 4-dimensional helicity (FDH) scheme [49]. In almost all cases, we compare our new method labelled by "drss" with the color-decomposition approach, which – since it makes use of the ordered algorithm – we denote "ordr". We will present all our results for two choices of

---

[8] The first four colors are always fixed, supplemented by the repeating sequence $(11)(22)(33)$ according to the number of gluons, i.e. for $n = 5$ we have $(cd)_k \equiv (22)(12)(23)(31)(11)$, while for $n = 9$ we use $(cd)_k \equiv (22)(12)(23)(31)(11)(22)(33)(11)(22)$.

Table 5

Computer times τ_n in seconds obtained from the 4- and 5-dimensional evaluation of n-gluon virtual corrections at two random phase-space points a and b using a 3.00 GHz Intel Core2 Duo processor. The results are shown for both the color-ordered and color-dressed method. All virtual corrections were evaluated twice to check for the consistency of the solutions. The n gluons have colors $(ab)_k$ and polarizations κ_k as specified in the text. Also given are the ratios $r_n = \tau_n/\tau_{n-1}$ where τ_n is the time to compute the correction for n gluons, in particular $\tau_n = (\tau_n^{(a)} + \tau_n^{(b)})/2$. The τ_n ratios of the ordered versus dressed method are depicted in the respective last column of the 4- and 5-dimensional case.

n	4D-case							5D-case						
	ordr			drss			$\frac{\text{ordr}}{\text{drss}}$	ordr			drss			$\frac{\text{ordr}}{\text{drss}}$
	$\tau_n^{(a)}$	$\tau_n^{(b)}$	r_n	$\tau_n^{(a)}$	$\tau_n^{(b)}$	r_n		$\tau_n^{(a)}$	$\tau_n^{(b)}$	r_n	$\tau_n^{(a)}$	$\tau_n^{(b)}$	r_n	
4	0.027	0.026		0.061	0.062		0.43	0.053	0.052		0.139	0.140		0.38
5	0.159	0.161	6.04	0.368	0.364	5.95	0.44	0.415	0.412	7.88	1.026	1.029	7.37	0.40
6	1.234	1.235	7.72	2.152	2.146	5.87	0.57	3.887	3.928	9.45	7.137	7.124	6.94	0.55
7	12.07	12.00	9.75	13.06	13.08	6.08	0.92	41.66	41.61	10.7	49.62	49.85	6.98	0.84
8	131.2	131.3	10.9	80.22	80.53	6.15	1.6	493.2	498.6	11.9	348.0	346.9	6.99	1.4
9	1579	1563	12.0	511.6	507.8	6.34	3.1	6316	6296	12.7	2466	2470	7.10	2.6
10	20,900	20,480	13.2	3640	3629	7.13	5.7	88,320	88,810	14.0	21,590	21,620	8.75	4.1

loop-momentum and spin-polarization dimensionalities D and D_s: the "4D-case" is obtained by setting $D = D_s = 4$ and sufficient when merely calculating the cut-constructible part (ccp) of the one-loop amplitude. The "5D-case" specified by $D = D_s = 5$ allows us to determine the complete result including the rational part. In NLO calculations one identifies the momenta of the external gluons with those of well separated jets. We therefore apply cuts on the generated $k = 1, \ldots, n$ phase-space momenta ($l = 3, \ldots, n$):

$$|\eta_l| < 2, \qquad p_{\perp,l} > 0.1|E_1 + E_2|, \qquad \Delta R_{kl} > 0.7, \tag{65}$$

where η_l and $p_{\perp,l}$ respectively denote the pseudo-rapidity and transverse momentum of the l-th outgoing gluon; the ΔR_{kl} describe the pairwise geometric separations in pseudo-rapidity and azimuthal-angle space of gluons k and l. We perform a series of studies in the context of double-precision computations: we investigate the accuracies with which the double pole, single pole (sp) and finite part (fp) of the full one-loop amplitudes are determined by our algorithm. We also examine the efficiency of calculating virtual corrections by means of simple phase-space integrations. To begin with, we will verify the expected exponential scaling of the computation time for different numbers of external gluons.

4.2.3. Scaling of the algorithm for n-gluon one-loop amplitudes

The scaling of the computer time can roughly be estimated by $(f \times C_{\max})^n$. The constants $C_{\max} = 5(4)$ and $1 < f \leqslant 4$ express the fact that the number of pentagon (box) cuts and the exponential scaling with n of the tree-level color-dressed recursion relation respectively govern the asymptotic scaling behavior of the unordered algorithm. Although one naively expects $f = 4$, this factor is reduced by the efficient re-use of gluon currents among different cuts. The $C_{\max}^n$ growth of the number of cuts reflects the large-n limit of the Stirling number $S_2(n, C_{\max})$. We show four tables summarizing our results for the computation times τ_n of obtaining $\mathcal{M}^{(1)}(\mathbf{g}_1, \ldots, \mathbf{g}_n) = \mathcal{M}_n^{(1)}(\lambda_k, (ij)_k)$ by using two independent solutions of the unitarity constraints. The time for the re-computation has been included in τ_n. In real applications such a consistency check will become unnecessary, thereby halving the evaluation time per phase-space point. Table 5 lists the times obtained by running the 4- and 5-dimensional algorithms for the

Table 6
Computer times τ_n in seconds for the same settings as used in Table 5, this time using a 2.66 GHz Intel Core2 Quad processor. The rightmost part of the table depicts the ratios of 4- versus 5-dimensional computer times for both approaches.

n	4D-case						5D-case						4D/5D	
	ordr			drss			ordr			drss			ordr	drss
	$\tau_n^{(a)}$	$\tau_n^{(b)}$	r_n	$\tau_n^{(a)}$	$\tau_n^{(b)}$	r_n	$\tau_n^{(a)}$	$\tau_n^{(b)}$	r_n	$\tau_n^{(a)}$	$\tau_n^{(b)}$	r_n		
4	0.030	0.030		0.069	0.070		0.059	0.059		0.156	0.157		0.51	0.44
5	0.180	0.179	5.98	0.418	0.413	5.98	0.464	0.465	7.87	1.150	1.148	7.34	0.39	0.36
6	1.384	1.383	7.71	2.419	2.410	5.81	4.370	4.340	9.38	8.036	7.996	6.98	0.32	0.30
7	13.53	13.52	9.78	14.64	14.65	6.07	46.65	46.40	10.7	56.06	55.99	6.99	0.29	0.26
8	147.2	147.5	10.9	90.48	91.60	6.22	550.9	549.5	11.8	395.2	391.9	7.02	0.27	0.23
9	1766	1764	12.0	585.9	585.0	6.43	7013	7029	12.8	2844	2845	7.23	0.25	0.21
10	23.100	22,830	13.0	4233	4208	7.21	98,760	98,360	14.0	24,220	24,410	8.55	0.23	0.17

calculation of two random phase-space points labelled "a" and "b". The n gluons have colors $(ij)_k = (ab)_k$ and alternating polarizations $\lambda_k = \kappa_k \equiv + - \cdots + -(+)$. Owing to the absence of pentagon cuts we find that the "4D-case" calculations are faster. More importantly, the computation time does not vary when the n-gluon kinematics changes. Hence, we can calculate the ratios $r_n = \tau_n/\tau_{n-1}$ by defining $\tau_n = (\tau_n^{(a)} + \tau_n^{(b)})/2$ and show these ratios in the table. While for the dressed algorithm these ratios are almost stable, they are larger and increase gradually for the method based on ordered amplitudes. This reflects the $(n-2)!$ factorial growth of the number of non-vanishing orderings of the color configuration $(ab)_k$ as given in Table 3. For the dressed approach, we find constant ratios of $r_n \approx 6$ and $r_n \approx 7$ in the "4D-case" and "5D-case", respectively. This manifestly confirms our expectation of exponential scaling. The difference between the 4- and 5-dimensional ratios obviously arises because of the absence of pentagon cuts in the "4D-case". The r_{10} ratios do not fit the constant trend. We cannot exclude though that this is a consequence of the occurrence of large structures of maps to store the vast number of color-dressed coefficients. The increasing number of higher-cut subtractions terms may also cause deviations from the expected scaling, which we derived from our simple arguments stated above. Also, the conceptually easier way of storing all coefficients and calculating the largest-m cuts first is by far not the most economic in terms of memory consumption.[9] For small n, the lower complexity of the ordered recurrence relation facilitates a faster calculation of the virtual corrections through ordered amplitudes. The turnaround appears for $7 < n < 8$ and is just slightly above $n = 7$ for the "4D-case". With $n \geqslant 8$ the dressed method becomes superior owing to the different growth characteristics of the two approaches. This is neatly expressed by the "ordr/drss" ratios given in Table 5.

We have cross-checked the measured computation times in a different processor environment using exactly the same settings. The results are shown in Table 6 and consistent with those of Table 5. Instead of the "ordr/drss" ratios, here we list ratios comparing the 4- and 5-dimensional computation for both approaches. They stress the relative importance of the pentagon-cut evaluations, which start to dominate the full calculation when n gets large.

In Table 7 we detail computation times when varying the polarizations of the n gluons while keeping their color configuration fixed. We have chosen the two settings $\lambda_k = \sigma_k \equiv + + - \cdots -$ and, as before, $\lambda_k = \kappa_k$. In terms of colors we consider the computationally less involved point

---

[9] It is for this reason that our calculations are currently limited to $n = 12$ in the "4D-case" and $n = 10$ in the "5D-case".

Table 7

Computer times τ_n in seconds obtained for the color-ordered and color-dressed evaluation of n-gluon virtual corrections in 4 and 5 dimensions using a 3.00 GHz Intel Core2 Duo processor. Results are shown for two different polarization choices σ_k and κ_k. The virtual corrections were computed at the same random phase-space point with the n-gluon colors set to $(cd)_k$. The choices are specified in the text. Ratios $r_n = \tau_n/\tau_{n-1}$ are given where $\tau_n = (\tau_n^{(\sigma_k)} + \tau_n^{(\kappa_k)})/2$ is the time to evaluate the correction for n gluons two times. The re-computation is used to check both solutions for their consistency. The τ_n ratios of the ordered versus dressed method are depicted in the respective last column of the 4- and 5-dimensional case.

n	4D-case							5D-case						
	ordr			drss			$\frac{\text{ordr}}{\text{drss}}$	ordr			drss			$\frac{\text{ordr}}{\text{drss}}$
	$\tau_n^{(\sigma_k)}$	$\tau_n^{(\kappa_k)}$	r_n	$\tau_n^{(\sigma_k)}$	$\tau_n^{(\kappa_k)}$	r_n		$\tau_n^{(\sigma_k)}$	$\tau_n^{(\kappa_k)}$	r_n	$\tau_n^{(\sigma_k)}$	$\tau_n^{(\kappa_k)}$	r_n	
4	0.049	0.045		0.074	0.076		0.63	0.088	0.085		0.153	0.155		0.56
5	0.186	0.185	3.95	0.364	0.364	4.85	0.51	0.479	0.483	5.56	1.000	1.000	6.49	0.48
6	1.186	1.182	6.38	2.071	2.068	5.69	0.57	3.629	3.586	7.50	6.805	6.752	6.78	0.53
7	4.185	4.277	3.57	11.82	11.77	5.70	0.36	14.02	13.95	3.88	44.42	44.46	6.56	0.31
8	27.12	26.96	6.39	70.34	71.10	6.00	0.38	98.52	99.13	7.07	294.8	297.8	6.67	0.33
9	245.0	242.9	9.02	443.8	445.5	6.29	0.55	960.3	954.8	9.69	2080	2070	7.00	0.46
10	1442	1446	5.92	3265	3270	7.35	0.44	5943	5968	6.22	18,610	18,480	8.94	0.32
11				28,670	28,690	8.78								
6				2.044		5.62								
7				11.66		5.70								
8				68.85		5.90								
9				420.4		6.11								
10				2972		7.07								
11				26,310		8.85								
12					292,000	11.1								

$(ij)_k = (cd)_k$. Both amplitudes are calculated at the same random phase-space point "c" dissimilar from the points "a" and "b" previously used. For none of the four calculations, we notice manifest deviations in the times $\tau_n^{(\lambda_k)}$ associated with the two polarization settings. When inspecting the "ordr/drss" ratios, we observe that the ordered approach is advantageous in cases where only a few orderings contribute to the result of a certain point in color space. The fluctuations seen in the growth factors mirror the unsteady increase with n in non-zero orderings as depicted in the last column of Table 3. For the dressed approach, we get similar, though somewhat smaller, growth factors compared to the previous test. In order to validate the dressed algorithm up to $n = 12$ external gluons, we introduced a few more optimizations specific to the 4-dimensional calculations.[10] The lower part of Table 7 shows the computer times obtained after the optimization. They are consistent with our previous findings. As mentioned before, $r_{n\geqslant 10} > 6$ likely occur for reasons of increasingly complex higher-cut subtractions and computer limitations in dealing with large memory structures.

For the calculation of the virtual corrections, one might question whether there exist enough points in color space that occur with many trivial orderings. If so, the color-decomposition based method would be more efficient on average. This is not the case for larger n as shown in Table 8. For gluon multiplicities of $n = 4, \ldots, 10$ and polarizations set according to κ_k, we list mean computation times, growth factors, "ordr/drss" and "4D/5D" ratios obtained for one-loop amplitude evaluations where the phase- and color-space points have been chosen randomly. Following the

---

[10] Some parts of the algorithm can be speed up once pentagon cuts are completely avoided.

Table 8

Color-configuration averaged computation times τ_n in seconds obtained from the 4- and 5-dimensional color-ordered and color-dressed evaluations of n-gluon virtual corrections using 2.66 GHz Intel Core2 Quad processors. Results are shown for random phase- and color-space points and alternating gluon polarizations $\lambda_k = \kappa_k$, see text. The respective growth factors $r_n = \tau_n/\tau_{n-1}$ are given where τ_n denotes the time needed to calculate the n-gluon one-loop amplitude two times. The re-computation is used to check the two solutions for their consistency. Several time ratios are formed and given in the respective columns to compare the ordered with the dressed method and the 4- with the 5-dimensional computation.

| n | 4D-case | | | | | 5D-case | | | | | 4D/5D | |
| | ordr | | drss | | $\frac{\text{ordr}}{\text{drss}}$ | ordr | | drss | | $\frac{\text{ordr}}{\text{drss}}$ | ordr | drss |
	τ_n	r_n	τ_n	r_n		τ_n	r_n	τ_n	r_n			
4	0.026		0.062		0.42	0.065		0.151		0.43	0.40	0.41
5	0.222	8.54	0.394	6.35	0.56	0.615	9.46	1.139	7.54	0.54	0.36	0.35
6	1.863	8.39	2.378	6.04	0.78	5.544	9.01	7.970	7.00	0.70	0.33	0.30
7	15.06	8.08	14.58	6.13	1.03	50.41	9.09	56.94	7.14	0.89	0.30	0.26
8	129.2	8.58	93.09	6.38	1.39	476.7	9.46	401.5	7.05	1.19	0.27	0.23
9	1127	8.72	603.6	6.48	1.87	4483	9.40	2800	6.97	1.60	0.25	0.22
10	10,980	9.74	3961	6.56	2.77	50,260	11.2	25,140	8.98	2.00	0.22	0.16

Table 9

Parameter values a and b obtained from curve fitting of the computation times τ_n to the functional form of $\tau_n = ab^n$. The results are given for the three different n-gluon color assignments used in Table 5 (hard), Table 7 (simple) and Table 8 (random) and for all four algorithms, the 4- and 5-dimensional color-ordered and color-dressed algorithm.

| configuration: | hard colors $(ab)_k$ | | simple colors $(cd)_k$ | | random non-zero colors | |
fit values:	$a/10^{-6}$ sec	b	$a/10^{-6}$ sec	b	$a/10^{-6}$ sec	b
4D, ordr	1.91	$9.75^{+0.59}_{-0.56}$	34.5	$5.65^{+0.32}_{-0.30}$	4.67	$8.57^{+0.10}_{-0.09}$
5D, ordr	2.66	$10.99^{+0.48}_{-0.46}$	45.6	$6.39^{+0.29}_{-0.28}$	7.84	$9.46^{+0.13}_{-0.12}$
4D, drss	39.4	$6.19^{+0.09}_{-0.08}$	28.2	$6.51^{+0.29}_{-0.28}$	38.7	$6.30^{+0.04}_{-0.04}$
5D, drss	50.8	$7.21^{+0.10}_{-0.10}$	62.5	$6.92^{+0.08}_{-0.09}$	53.3	$7.28^{+0.11}_{-0.09}$

method outlined in Section 3.3, we only considered non-zero color configurations. We averaged over many events, for $n = 4, \ldots, 10$ gluons, we used $\mathcal{O}(10^6), \ldots, \mathcal{O}(10^2)$ points. We observe that the pattern of the results in Table 8 resembles that found in Tables 5 and 6 where we have studied the more complicated color point $(ik)_k = (ab)_k$. The ratios comparing the ordered and dressed approach are smaller with respect to those of Tables 5 and 6. This signals that the mean number of contributing orderings is somewhat lower than for the $(ab)_k$ case. We finally report dressed growth factors that are consistent with our previous findings confirming the approximate 6^n and 7^n growths in computational complexity of the new method for the 4- and 5-dimensional case, respectively.

Using the results of Tables 5, 7 and 8 we have performed fits to the functional form $\tau_n = ab^n$. We show the outcome of the curve fittings in Table 9. Recall that the computation times have been obtained by using different color assignments for the n gluons. Tables 5 and 7 present results where we have chosen $(ij)_k = (ab)_k$ and $(ij)_k = (cd)_k$ as examples of hard and simple color configurations, respectively. We have averaged over non-zero color settings to find the results of Table 8. Considering the performance of the dressed algorithm, we conclude that these data are in agreement with exponential growth for all color assignments. The errors on the fit parameter b
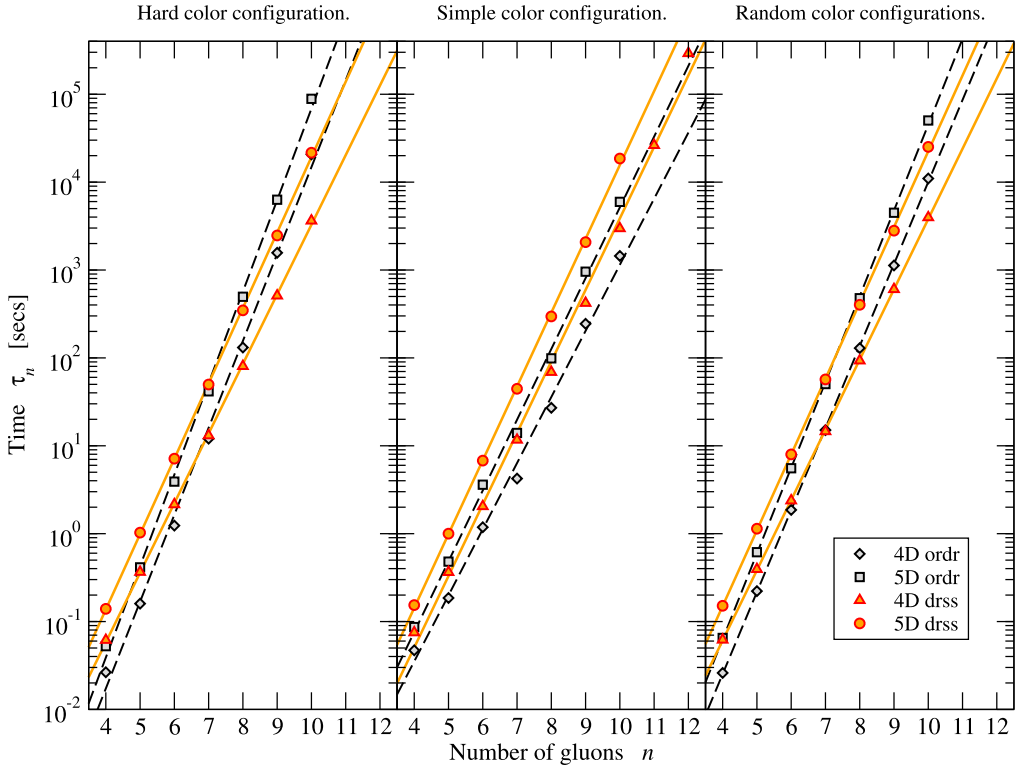
Fig. 8. Computation times τ_n versus the number n of external gluons for the three different gluon color assignments used in Table 5 (hard), Table 7 (simple) and Table 8 (random). The results reported in these tables are shown for the 4- and 5-dimensional color-ordered and color-dressed algorithms. The solid and dashed curves each represent the outcomes of the fits listed in Table 9 for both the dressed and ordered approach, respectively.

are relatively small, only the 4-dimensional case of simple colors is somewhat worse because we included results up to $n = 12$ where parts of the computation become less efficient as explained above. The hard- and simple-colors cases of the ordered approach show rather large errors for the b-parameter signalling that the genuine scaling law is not of an exponential kind in both cases. Interestingly, one observes an effective exponential scaling when averaging over many non-zero color configurations. The growth described by the b-parameter is however a good two units stronger for the ordered approach than the growth seen in the color-dressed approach. To summarize, we have plotted in Fig. 8 all computer times reported in Tables 5, 7 and 8 as a function of the number of external gluons in the range $4 \leqslant n \leqslant 12$. We have included in these plots the curves $\tau_n = ab^n$, which we calculated from the respective fit parameters stated in Table 9.

4.2.4. Accuracy of the coefficient determination

In the following we will discuss the quality of the semi-numerical evaluations of $\mathcal{M}_n^{(1)}$ amplitudes for both the color-ordered and color-dressed approaches. To this end we analyze the logarithmic relative deviations of the double pole, the single pole and the finite part. Independent of the number n of gluons, we define them as follows:
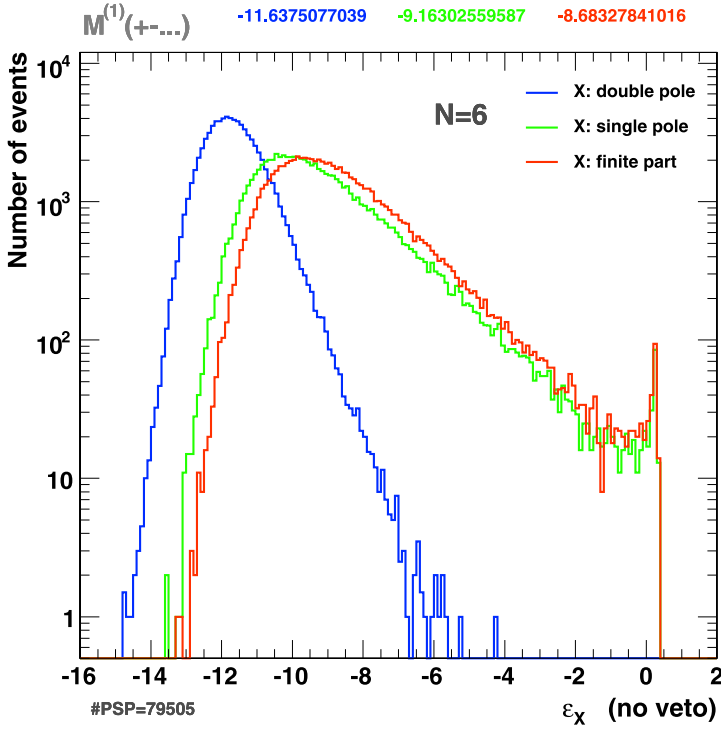
Fig. 9. Relative accuracies of the $1/\epsilon^{2,1,0}$ poles of $n = 6$ gluon one-loop amplitudes as determined by the double-precision color-dressed algorithm. The gluon polarizations are given by $\lambda_k = + - + - + -$, colors were chosen randomly among non-zero configurations. Vetoed events are included, only those with unstable ortho-vectors have been left out, see text for more explanations. The mean accuracies and the number of randomly picked phase-space points are displayed in the top row and bottom left corner of the plot, respectively.

$$\varepsilon_{\mathrm{dp}} = \log_{10} \frac{|\mathcal{M}_{\mathrm{dp,num}}^{(1)[1]} - \mathcal{M}_{\mathrm{dp,th}}^{(1)}|}{|\mathcal{M}_{\mathrm{dp,th}}^{(1)}|}, \qquad \varepsilon_{\mathrm{s/fp}} = \log_{10} \frac{2|\mathcal{M}_{\mathrm{s/fp,num}}^{(1)[1]} - \mathcal{M}_{\mathrm{s/fp,num}}^{(1)[2]}|}{|\mathcal{M}_{\mathrm{s/fp,num}}^{(1)[1]}| + |\mathcal{M}_{\mathrm{s/fp,num}}^{(1)[2]}|}, \tag{66}$$

where the structure of the double-poles $\mathcal{M}_{\mathrm{dp,th}}^{(1)}$ is known analytically given by Eq. (61). We use two independent solutions denoted by [1] and [2] to test the accuracy of the single poles and finite parts. All results reported here were obtained by using double-precision computations. We have run all our algorithms by choosing color configurations and phase-space points at random. Colors are distributed according to the "Non-Zero" method presented in Section 3.3. The phase-space points are accepted only if they obey the cuts, which we have specified earlier, see Section 4.2.2. The gluon polarizations are always alternating set by $\lambda_k = \kappa_k$. Fig. 9 shows the ε distributions in absolute normalization, which we obtain from the 5-dimensional color-dressed calculation for the case of $n = 6$ external gluons. The number of points used to generate the plots is given in the bottom left corner, the top rows display the means of the double-, single-pole and finite-part distributions. Limited to double-precision computations, we find that the numerical accuracy of our results for $\mathcal{M}_n^{(1)}$ is satisfying. With ε peak positions smaller than the respective mean values $\langle \varepsilon_{\mathrm{d/s/fp}} \rangle < -8$, we are able to provide sufficiently accurate solutions for almost all phase-space configurations.

Table 10

Fractions of n-gluon events that have a stable set of basis vectors in orthogonal space and also pass the veto on inaccurate master-integral bubble coefficients when using $\Delta_{\text{veto}} = 0.02$. In brackets, fractions of n-gluon events that pass the test for unstable ortho-vectors.

n	4D, ordr	5D, ordr	4D, drss	5D, drss
4	1.0	1.0	1.0	1.0
5	0.992	0.991	0.984	0.984 (0.999)
6	0.960	0.960	0.964	0.972 (0.994)
7	0.872	0.873	0.891	0.892 (0.982)
8	0.635	0.642	0.829	0.825 (0.953)
9	0.182 (0.84)	0.205 (0.81)	0.532 (0.93)	0.533 (0.903)
10	0.0 (0.61)	0.0 (0.50)	0.38 (0.86)	0.33 (0.83)

There is however a certain fraction of events where the single pole and finite part cannot be determined reliably. These $\mathcal{O}(100)$ (out of 79505) events occur because in exceptional cases small denominators, such as vanishing Gram determinants made of external momenta, cannot be completely avoided by the generalized-unitarity algorithms. We also see accumulation effects where larger numbers get multiplied together while determining the subtraction of higher-cut contributions. Owing to the limited range of double-precision calculations, such effects can lead to insufficient cancellations of intermediate large numbers that are supposed to cancel out eventually.[11] The current implementation of the algorithm has no special treatment for these exceptional events. One either has to come up with a more sophisticated method treating these points separately or increase the precision with which the corrections are calculated. Both of which is beyond the scope of this paper and we leave it at vetoing these points. Yet, we need robust criteria that allow us to keep track of the quality of our solutions: we first test the orthonormal basis vectors that span the space complementary to the physical space constructed from the external momenta associated with the particular cut configuration under consideration. Failures in generating these basis vectors always lead to the rejection of the event.[12] In the example of Fig. 9, such events occurred with a rate of 0.6% and were not included in the plot. Secondly, and more importantly, we test the reliability of solving the systems of equations to determine the master-integral coefficients. To this end we generate an extra 4-dimensional loop momentum during the evaluation of the bubble coefficients establishing the cut-constructible part. Inaccuracies in solving for triangle etc. coefficients will be also detected, since at this level all higher-cut subtractions are necessary to obtain the correct value of the bubble coefficients. We use the extra loop momentum to individually re-solve for the cut-constructible bubble coefficient and compare this solution with the one obtained in first place. We veto the event, if the deviation Δ_{veto} in the complex plane of the two solutions exceeds a certain amount. We fix the veto cut at $\Delta_{\text{veto}} = 0.02$ for this publication. Having this cross-check at hand, we gain nice control over the events populating the tail of the accuracy distributions in Fig. 9. Applying the veto, we arrive at the distributions presented in the top left plot of Fig. 12 where the steeper tails clearly demonstrate the effect of the veto. Certainly, both these shortcomings of imprecise ortho-vectors and inaccurately solved coefficients can be lifted by switching to higher precision whenever the respective double-precision evaluations have not passed our criteria. Accordingly, Table 10 quantifies the fractions of events, which are within

---

[11] More detailed explanations can be found in Ref. [37].

[12] We test in particular whether the normalization of the orthonormal basis vectors deviates less than 10^{-12} units from one.

the scope of the color-dressed and color-ordered algorithms presented here. Owing to the more complicated event structures, the fraction of rejected events increases with n, where most of the events fail the bubble-coefficient test. We observe that the loss of events is more severe for the ordered algorithm.

In the upper part of Figs. 10–16 we show the distributions of relative accuracies ε as occurring in the evaluation of gluon loop corrections with $n = 4, \ldots, 9$ external gluons. The lower part of these figures and Figs. 17 and 18 themselves depict scatter graphs visualizing the relative accuracies as a function of the size of the virtual corrections for the single-pole and finite-part contributions only, as the double-pole contribution has no observable variance. This form of presenting the results has information on whether certain points dominate the uncertainty of the total correction when averaging over the phase space. The r-variables used in these plots are defined by

$$r = \frac{1}{2\pi} \frac{\Re(\mathcal{M}^{(0)\dagger}\mathcal{M}^{(1)})}{|\mathcal{M}^{(0)}|^2} \qquad (67)$$

and represent corrections of the order of α_s. Specifically, the r and r' given in the plots are obtained by employing $\mathcal{M}^{(1)} = \mathcal{M}^{(1)[1]}_{\text{s/fp,num}}$ and $\mathcal{M}^{(1)} = \mathcal{M}^{(1)[2]}_{\text{s/fp,num}}$, respectively. In all cases we have rejected events with unreliable basis vectors in orthogonal space. Except for the results presented in Fig. 18, we have vetoed all events that led to unstable solutions of the bubble master-integral coefficient using $\Delta_{\text{veto}} = 0.02$. The statistics concerning these rejections is shown in Table 10.

We compare in all plots of Figs. 10–16 the color-dressed with the color-ordered approach where the results of the latter are indicated by dashed curves in the spectra (with the $\langle\varepsilon\rangle$ given by the lower top row of numbers) and brighter points in the scatter graphs. The ε spectra of the
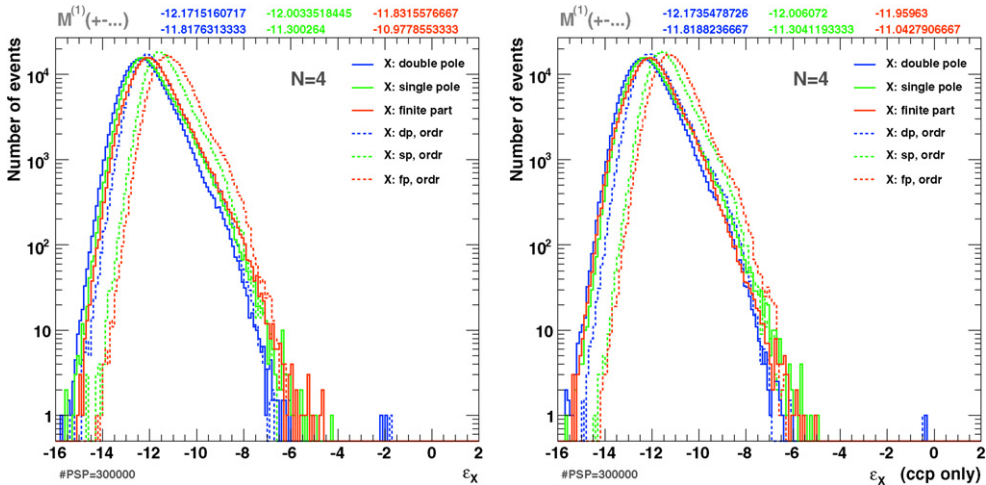
Fig. 10. Double-, single-pole and finite-part accuracy distributions (upper part) and scatter graphs (lower part) extracted from double-precision computations of one-loop amplitudes for $n = \text{N} = 4$ gluons with polarizations $\lambda_k = +-+-$ and randomly chosen non-zero color configurations. The virtual corrections were calculated at random phase-space points satisfying the cuts detailed in the text. Unstable solutions were vetoed. Results from the color-dressed algorithm are compared with those of the color-ordered method indicated by dashed curves and brighter dots in the plots. The 5(4)-dimensional case is shown in the top left (right) and center (bottom) part of the figure. The definitions of ε and r are given in the text. All scatter graphs contain 2×10^4 points.
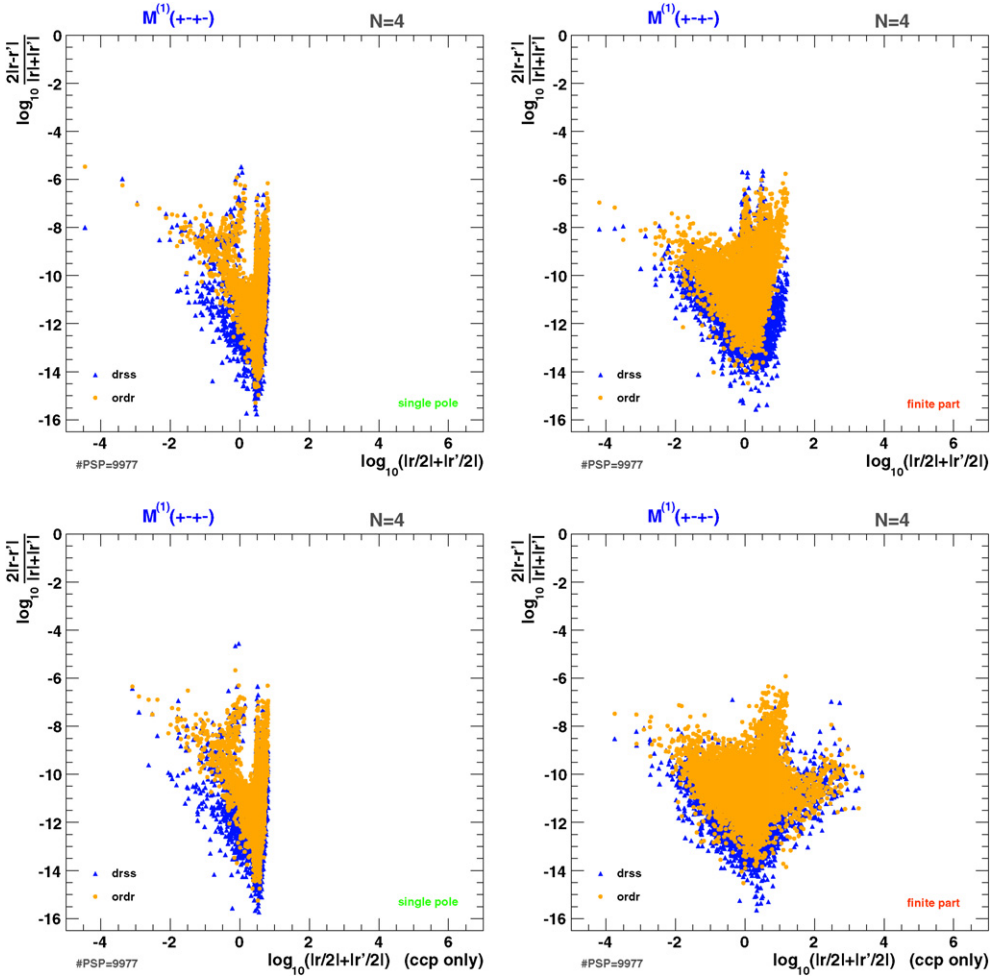
Fig. 10. (*continued*)

"5D-case" ("4D-case") are always shown in the top left (right) parts of the figures; the associated scatter graphs are compiled in the center (bottom) parts. In Fig. 17 we present our results for $n = 10$ gluons where for reasons of limited statistics we solely show the scatter graphs related to the dressed method. The veto procedure has a very strong impact on $\mathcal{M}_{9,10}^{(1)}$ calculations. For the purpose of direct comparisons between vetoed and non-vetoed samples, we have added in Fig. 18 scatter plots that include vetoed events.

In all cases we notice that the double poles are obtained very accurately with almost no loss in precision for increasing number of gluons. The n-dependence of the single-pole and finite-part precisions is not as stable as for the double pole. We see noticeable shifts of the peak and mean positions towards larger values when incrementing the number of external gluons. Because of the introduced veto procedure, the distribution's tails are under better control falling off more quickly around $\varepsilon \approx -2$. In rare cases worse accuracies occur, which happens more frequently for the 5-dimensional calculations. We can avoid these cases, if we extend the veto

criteria by re-solving for and testing the rational bubble coefficient as well. For $n \geqslant 9$, the limitations of double-precision computations unavoidably lead to rather unreliable single-pole and finite-part determinations. As an interesting fact, we observe that the color-dressed method yields throughout results of higher precision. Moreover, the decrease in accuracy for growing n is more moderate compared to the method based on color ordering. Clearly, on the one hand the ordered algorithm has to be run for many orderings and may therefore lead to an accumulation of small imprecisions. On the other hand a rather inaccurate determination of $m^{(1)}$ may appear just for a single ordering, in turn spoiling the overall result. Both effects make the ordered approach less capable of delivering accurate results. Turning to the scatter plots, we find that the most accurate but also inaccurate evaluations occur for points distributed near the vertical line of $\mathcal{O}(1)$ corrections. It is very encouraging that all top right quadrants are rather sparsely populated, dispelling the doubts that insufficiently determined large corrections may dominate our final results. The scatter regions of the double-pole solutions remain almost unchanged for larger n, while those of the single poles and finite parts are slightly growing gradually shifting towards lower relative accuracies. The scatter patches of the dressed method are displaced with respect to those of the color-decomposition approach: advantageously, they cover regions of greater precision, in particular populate the bottom right quadrants more densely. Due to the simplicity of the 4-gluon kinematics, the case of $n = 4$ gluons stands out from the rest: the single pole and finite part can be obtained with almost the same accuracy as the double pole. This feature is preserved even if rational-part calculations are included. With 5 gluons or more it is common that all coefficients contribute to the decomposition of the one-loop amplitude. The relative accuracies of the single poles and finite parts therefore develop a much different, less steeper, tail compared to the double poles. There are almost no differences between the double- and single-pole results obtained from the 4- and 5-dimensional algorithms. This is no surprise, since the coefficients necessary
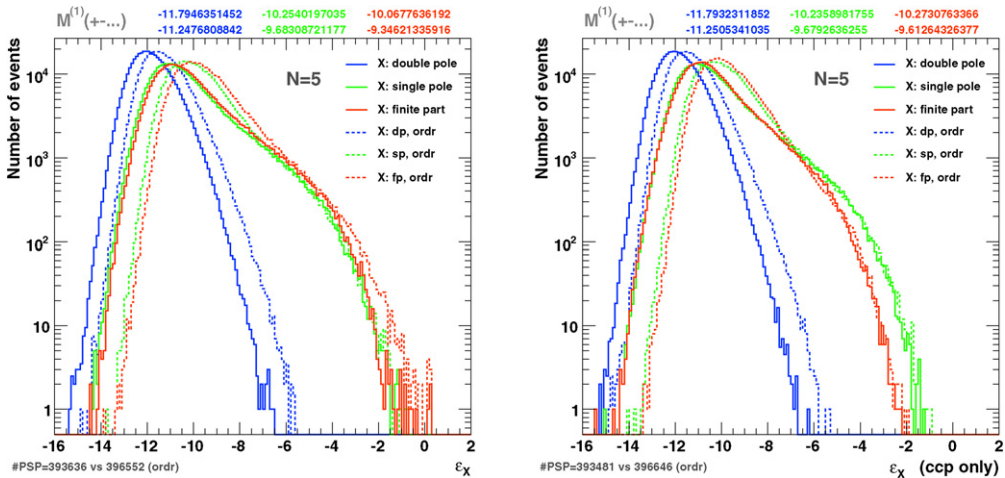
Fig. 11. Double-, single-pole and finite-part accuracy distributions (upper part) and scatter graphs (lower part) extracted from double-precision computations of one-loop amplitudes for $n = \mathbb{N} = 5$ gluons with polarizations $\lambda_k = + - + - +$ and randomly chosen non-zero color configurations. The virtual corrections were calculated at random phase-space points satisfying the cuts detailed in the text. Unstable solutions were vetoed. Results from the color-dressed algorithm are compared with those of the color-ordered method indicated by dashed curves and brighter dots in the plots. The 5(4)-dimensional case is shown in the top left (right) and center (bottom) part of the figure. The definitions of ε and r are given in the text. All scatter graphs contain 2×10^4 points.
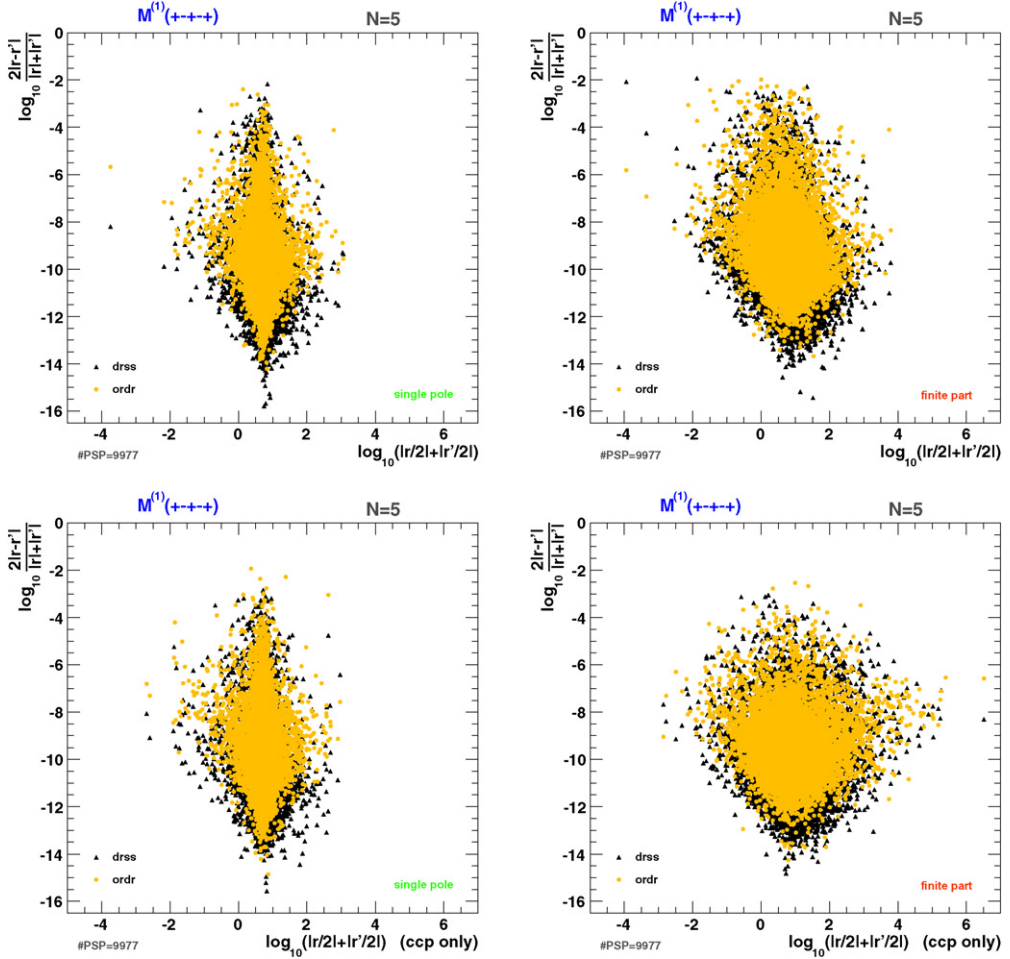
Fig. 11. (*continued*)

to reconstruct these poles can be determined in 4 dimensions and our algorithms have been set up accordingly. In the absence of rational-part calculations it turns out that the finite parts may on average be obtained slightly more precisely than the single poles. The tails of the $1/\epsilon$ spectra reach out to the largest ε-values occurring in the evaluation of the cut-constructible part. The behavior is reversed in the 5-dimensional case owing to the addition of the rational part. For the same reason, we note increased $\langle \varepsilon_{\mathrm{fp}} \rangle$ in the "5D-case", furthermore, the 5-dimensional scatter graphs show higher densities with respect to the 4-dimensional ones at lower accuracies.

As a special case of Fig. 12 we have displayed in Fig. 13 accuracy distributions and scatter plots for $n = 6$ gluons of polarizations $\lambda_k = + + - - - -$ where instead of using random color-space points the fixed non-zero color configuration $(ij)_k = (12)(21)(13)(31)(11)(22)$ has been selected. We notice that all ε-spectra are shifted towards smaller accuracies. Also, as illustrated by the scatter graphs, the magnitude of the virtual corrections is bound at $\mathcal{O}(1)$ with the exception of the finite piece of the cut-constructible part of the one-loop amplitudes. Interestingly, this is corrected back by adding in the rational part.

In Ref. [37] it was shown that the finite-part accuracy of the evaluation of ordered amplitudes is mostly correlated with that of the single poles. We have studied this issue for the dressed algorithm in the "5D-case". The corresponding scatter plots also include the vetoed events and are presented in Fig. 19. The multitude of points is distributed along the diagonal indicating a strong correlation. As for color-ordered amplitudes the evaluation of the rational part becomes more involved with increasing gluon numbers. Therefore, regions of lower finite-part precision start to get populated distorting the diagonal trend.

4.2.5. Convergence of Monte Carlo phase-space integrations using color sampling

Finally, we want to show that the Monte Carlo sampling as defined in Eq. (44) converges sufficiently fast for the color-dressed calculated virtual corrections. To this end we generalize the LO discussion following Eq. (35) with the details given in Section 3.3. The relevant quantity to explore in the Monte Carlo averaging is

$$
S_{\text{MC}}^{(0+1)} = \frac{1}{N_{\text{colpts}}} \sum_{k=1}^{N_{\text{colpts}}} W_{\text{col}}(n_1, n_2, n_3) \times \left[\left| \mathcal{M}_k^{(0)} \right|^2 + \frac{\widehat{\alpha}_s}{2\pi} \Re \left(\mathcal{M}_{\text{fp},k}^{(1)} \mathcal{M}_k^{(0)\dagger} \right) \right] \tag{68}
$$

where we choose $\widehat{\alpha}_S = 0.12$ and $\mathcal{M}_{\text{fp},k}^{(1)}$ is the finite part of the virtual corrections. The sum over the N_{colpts} color configurations for each phase-space point is an optional "mini-Monte Carlo" over colors for faster convergence as a function of the number of phase-space point evaluations. By adding the real corrections to Eq. (68) and performing the coupling constant renormalization and mass factorization, one obtains the gluonic contribution to the NLO multi-jet differential cross section. Therefore, the convergence of Eq. (68) is the relevant quantity to study.

Fig. 12. Double-, single-pole and finite-part accuracy distributions (upper part) and scatter graphs (lower part) extracted from double-precision computations of one-loop amplitudes for $n = \mathrm{N} = 6$ gluons with polarizations $\lambda_k = + - + - + -$ and randomly chosen non-zero color configurations. The virtual corrections were calculated at random phase-space points satisfying the cuts detailed in the text. Unstable solutions were vetoed. Results from the color-dressed algorithm are compared with those of the color-ordered method indicated by dashed curves and brighter dots in the plots. The 5(4)-dimensional case is shown in the top left (right) and center (bottom) part of the figure. The definitions of ε and r are given in the text. All scatter graphs contain 2×10^4 points.
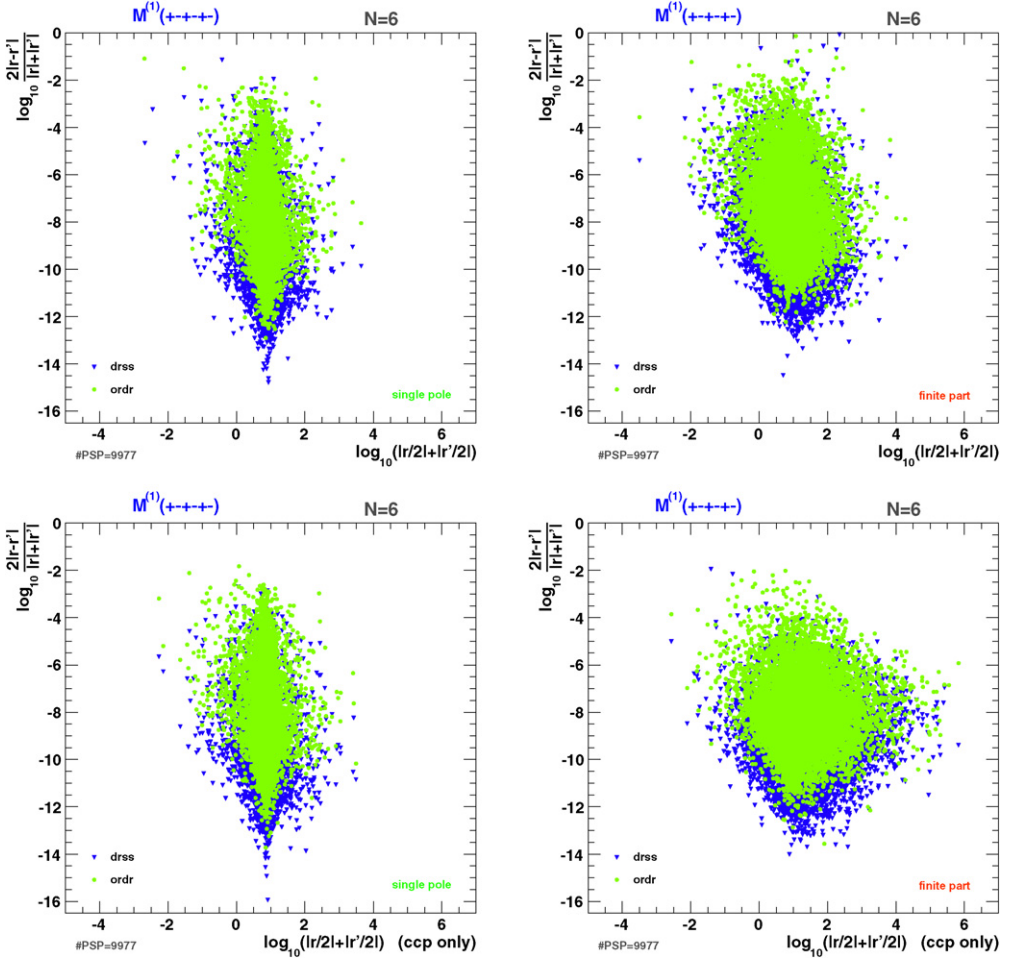
Fig. 12. (*continued*)

By defining the *n*-gluon color-summed counterpart of $S_{\mathrm{MC}}^{(0+1)}$,

$$S_{\mathrm{col}}^{(0+1)} = \sum_{i_1,\ldots,i_n=1}^{3} \sum_{j_1,\ldots,j_n=1}^{3} \left[\left| \mathcal{M}^{(0)} \right|^2 + \frac{\widehat{\alpha}_s}{2\pi} \Re\left(\mathcal{M}_{\mathrm{fp}}^{(1)} \mathcal{M}^{(0)\dagger} \right) \right], \tag{69}$$

we can form the ratios

$$R^{(0+1)} = \frac{\langle S_{\mathrm{MC}}^{(0+1)} \rangle \pm \sigma_{\langle S_{\mathrm{MC}}^{(0+1)} \rangle}}{\langle S_{\mathrm{col}}^{(0+1)} \rangle}, \qquad R^{(\mathrm{V})} = \frac{\langle S_{\mathrm{MC}}^{(0+1)} \rangle \pm \sigma_{\langle S_{\mathrm{MC}}^{(0+1)} \rangle}}{\langle S_{\mathrm{col}}^{(0)} \rangle} \tag{70}$$

analogously to Eq. (39). We define the mean values and standard deviations of the ratios similarly to Eqs. (37) and (38), respectively. Note that $S_{\mathrm{col}}^{(0)}$ is already defined at LO by Eq. (36). As we increase the number of Monte Carlo points, N_{MC}, the $R^{(\mathrm{V})}$-ratios quantify the relative importance of the virtual corrections, while the $R^{(0+1)}$-ratios should converge to one. For the latter, this is

nicely demonstrated in Fig. 20 for the 4-gluon virtual corrections and the "Non-Zero" sampling scheme as described in Section 3.3. Including the error on the average color sum we obtain after 15,900 events $\langle S_{\mathrm{MC}}^{(0+1)} \rangle / \langle S_{\mathrm{col}}^{(0+1)} \rangle = 0.939 \pm 0.039(\mathrm{MC}) \pm 0.028(\mathrm{col})$, which is satisfactory for this consistency check. Similarly to the tree-level case in Fig. 21 we again look separately at the relative errors of the two Monte Carlo averages that make up the R-ratios. The two curves at the bottom of the upper panel represent how $\sigma_{\langle S_{\mathrm{MC}}^{(0+1)} \rangle} / \langle S_{\mathrm{MC}}^{(0+1)} \rangle$ and $\sigma_{\langle S_{\mathrm{col}}^{(0+1)} \rangle} / \langle S_{\mathrm{col}}^{(0+1)} \rangle$ behave for the results presented in Fig. 20. We notice that, as at tree level, the color sampling introduces an additional uncertainty on top of the uncertainty given by the pure phase-space integration. For the examples of 4- and 5-gluon scatterings, Fig. 21 also depicts as functions of N_{MC} the relative errors of the averages $\langle S_{\mathrm{MC}}^{(0+1)} \rangle$ and $\langle S_{\mathrm{col}}^{(0)} \rangle$ that feed into the corresponding $R^{(\mathrm{V})}$-ratios. In all these cases we find that the Monte Carlo integration for each average on its own converges sufficiently.

As in the LO discussion we want to illustrate how many events are needed to achieve a certain relative integration uncertainty when performing the Monte Carlo color sampling. In analogy to Eq. (40) we can construct the ratio

$$R_{\mathrm{MC}}^{(0+1)}(N_{\mathrm{MC}}) = \frac{\sum_{r=1}^{N_{\mathrm{MC}}} S_{\mathrm{MC},r}^{(0+1)}}{\sum_{r=1}^{N_{\mathrm{MC}}} S_{\mathrm{col},r}^{(0+1)}} \tag{71}$$

as a function of N_{MC}. Again, it is interesting to change the normalization of the ratio and also define

$$R_{\mathrm{MC}}^{(\mathrm{V})}(N_{\mathrm{MC}}) = \frac{\sum_{r=1}^{N_{\mathrm{MC}}} S_{\mathrm{MC},r}^{(0+1)}}{\sum_{r=1}^{N_{\mathrm{MC}}} S_{\mathrm{col},r}^{(0)}} \tag{72}$$
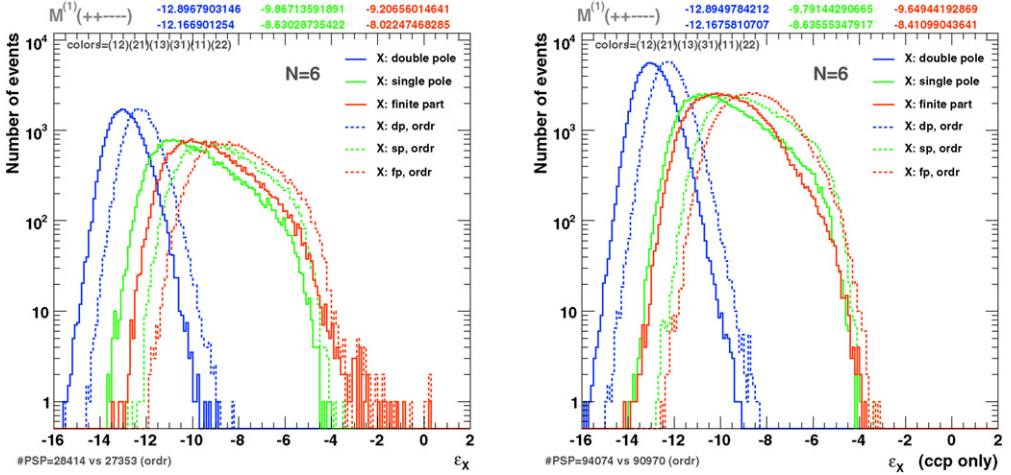
Fig. 13. Double-, single-pole and finite-part accuracy distributions (upper part) and scatter graphs (lower part) as obtained from double-precision evaluations of one-loop amplitudes for $n = \mathrm{N} = 6$ gluons with polarizations and colors set to $\lambda_k = + + - - - -$ and $(ij)_k = (12)(21)(13)(31)(11)(22)$, respectively. The virtual corrections were calculated at random phase-space points satisfying the cuts detailed in the text. The veto procedure has been applied to reject unstable solutions. The results given by the color-dressed algorithm are compared with those of the color-ordered method indicated by dashed curves and brighter dots in the plots. The 5(4)-dimensional case is shown in the top left (right) and center (bottom) part of the figure. The definitions of ε and r are given in the text. Each scatter graph contains 2×10^4 points. 94.7(94.1)% and 91.2(91.0)% of the events pass all tests in the dressed and ordered "5(4)D-case", respectively.
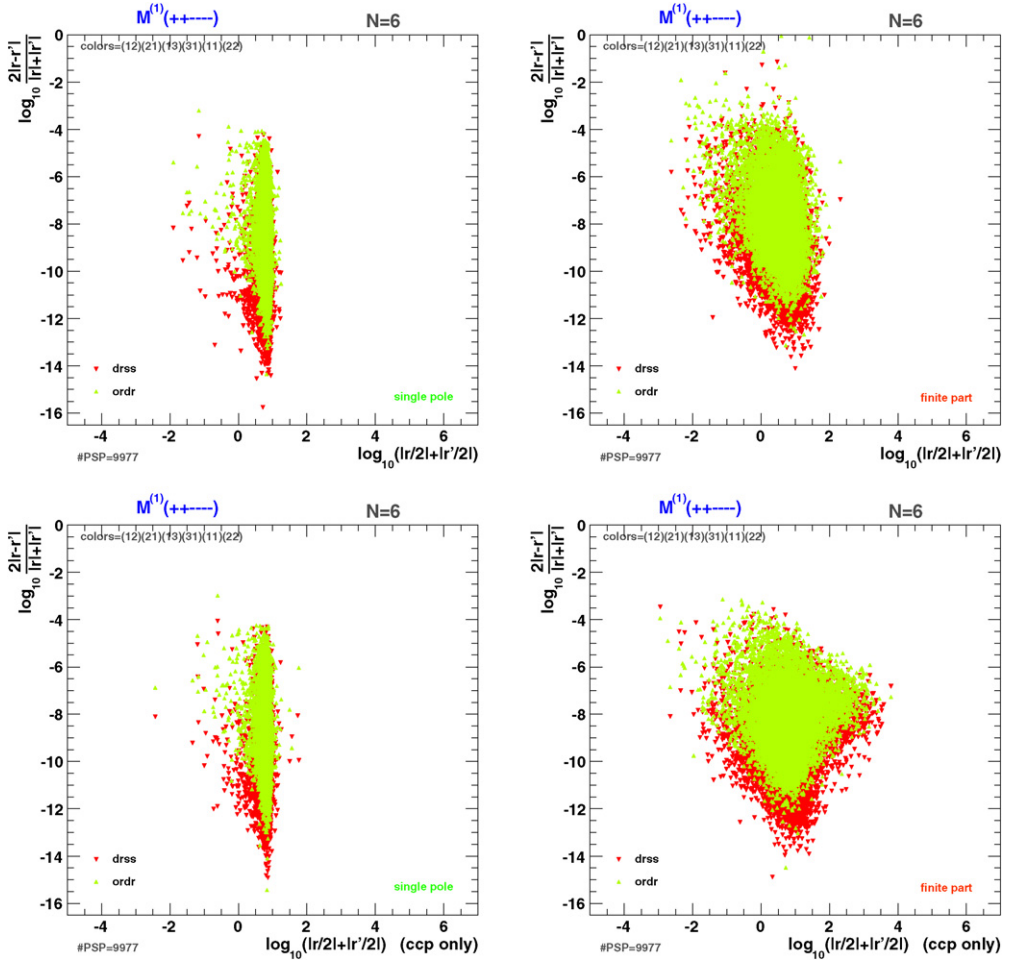
Fig. 13. (*continued*)

in order to study the impact of the virtual corrections. As before we partition $N_{event} = N_{trial} \times N_{MC}$ events to have a certain number of trials to compute the corresponding mean values μ and standard deviations σ for n-gluon LO and virtual scattering according to Eqs. (41) and (42), respectively. For the case of $R_{MC}^{(0+1)}(N_{MC})$ and 4-gluon scattering, the number of Monte Carlo points versus a given relative accuracy is shown in the inlaid plot of Fig. 20. As at LO, the curve bends behaving as statistically determined after a certain amount of Monte Carlo integration steps.

To quantify the color-integration performances, we again perform fits to the functional form $A \times N_{MC}^{-B}$ and show the values of the fitted parameters in Table 11 for the various cases. As argued in Section 3.3 for large enough N_{MC}, we expect a scaling of σ/μ that is proportional to $1/\sqrt{N_{MC}}$. The goodness of the sampling schemes is signified by the A- and A'-parameters, where the latter is more important since the time factors are included. Smaller values of these parameters indicate a better efficiency of the sampling procedure.

Table 11

Parameter values B, A and A' obtained from curve fitting of the $\sigma(R_{MC})/\mu(R_{MC})$ to the functional form $A \times N_{MC}^{-B}$. The results are given for the different ways of sampling over colors in n-gluon scattering. The 4-gluon case marked by "$*$" corresponds to the consistency check shown in Fig. 20, where $R_{MC}^{(0+1)}$ has been considered. In all other cases $R_{MC}^{(V)}$ has been used, cf. Figs. 22, 23 and 24. Note that for $n = 6$, we have fitted $\sigma(R_{MC}^{(V)})$. The parameters $A' = Af^B$ take into account that the evaluation of a fixed number of Monte Carlo events takes longer for the other than "Naive" color-sampling methods. The time factors f relative to the "Naive" case are also displayed.

:)	Naive		Conserved				Non-Zero				Non-Zero, $N_{colpts} = 4$			
n	B	A	B	A	A'	f	B	A	A'	f	B	A	A'	f
4*							0.479	3.36						
4	0.497	22.0	0.489	5.41	17.0	10.4	0.476	3.57	13.5	16.4	0.485	2.05	15.6	65.7
5	0.482	59.4	0.454	13.3	43.3	13.5	0.442	9.71	36.4	19.8	0.439	5.56	37.8	79.2
6	0.325	7.08	0.344	5.37	14.0	16.3	0.255	1.60	3.50	21.7	0.233	0.850	2.14	87.6

Using the $R^{(V)}$ and $R_{MC}^{(V)}(N_{MC})$ ratios, we summarize in Figs. 22–25 our Monte Carlo integration results for $n = 4, \ldots, 7$ gluon scattering processes and for the various color-sampling schemes. The upper graphs display the averaging of $S_{MC}^{(0+1)}$ normalized to the Monte Carlo average of the color-summed LO contribution as a function of the number of phase-space evaluations.[13] We also indicate the estimate of the integration uncertainty of the color sampling,
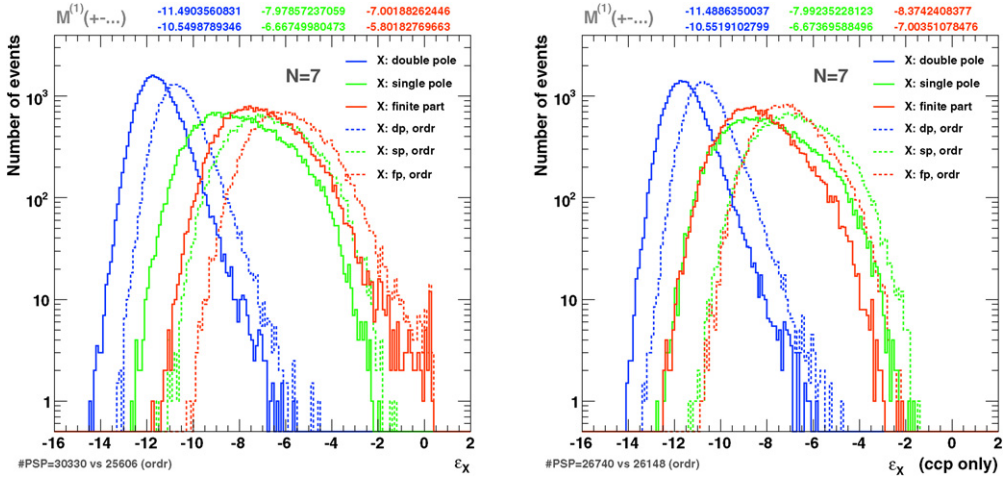
Fig. 14. Double-, single-pole and finite-part accuracy distributions (upper part) and scatter graphs (lower part) extracted from double-precision computations of one-loop amplitudes for $n = \mathrm{N} = 7$ gluons with polarizations $\lambda_k = +-+-+-+$ and randomly chosen non-zero color configurations. The virtual corrections were calculated at random phase-space points satisfying the cuts detailed in the text. Unstable solutions were vetoed. Results from the color-dressed algorithm are compared with those of the color-ordered method indicated by dashed curves and brighter dots in the plots. The 5(4)-dimensional case is shown in the top left (right) and center (bottom) part of the figure. The definitions of ε and r are given in the text. All scatter graphs contain 2×10^4 points.

---

[13] As for the LO studies in Section 3.3, the gluon polarizations are taken alternating and remain fixed while performing the Monte Carlo integrations.
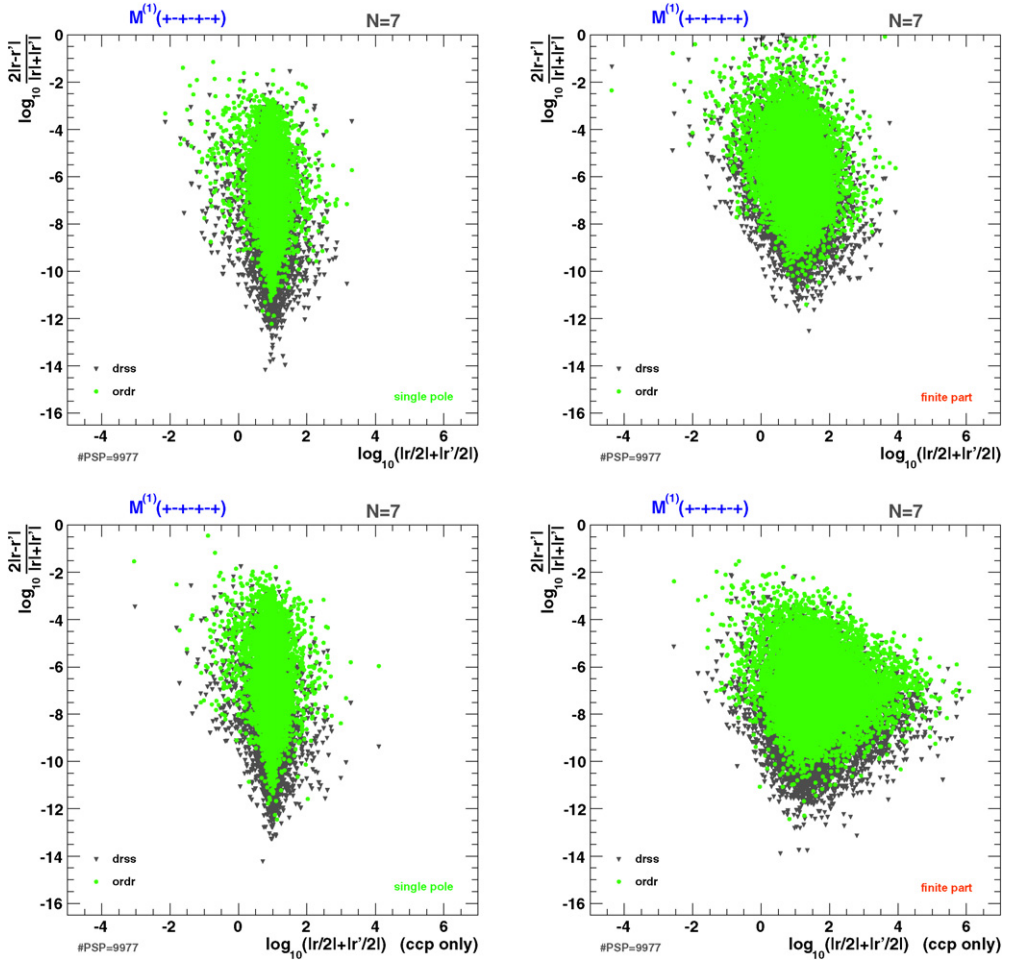
Fig. 14. (*continued*)

Table 12
Monte Carlo integration results for the $R^{(V)}$ ratios as defined in the text after N_{MC} phase-space point evaluations for n-gluon scattering and different color-sampling schemes using color-dressed tree-level and one-loop amplitude calculations. Note that the errors on $R^{(V)}$ indicated by "(col)" arise from the computation of the color-summed average. They are given in addition to those related to the color sampling.

:)	Naive		Conserved		Non-Zero		Non-Zero, $N_{colpts} = 4$	
n	N_{MC}	$R^{(V)}$	N_{MC}	$R^{(V)}$	N_{MC}	$R^{(V)}$	N_{MC}	$R^{(V)}$
4	$4 \cdot 10^6$	0.4739 ± 0.0054 ± 0.0011(col)	$4 \cdot 10^6$	0.4750 ± 0.0017 ± 0.0011(col)	$4 \cdot 10^6$	0.4724 ± 0.0013 ± 0.0011(col)	$1 \cdot 10^6$	0.4738 ± 0.0020 ± 0.0022(col)
5	631 K	0.241 ± 0.022 ± 0.0024(col)	631 K	0.2673 ± 0.0072 ± 0.0023(col)	631 K	0.2744 ± 0.0058 ± 0.0024(col)	160 K	0.2790 ± 0.0058 ± 0.0044(col)
6	64 K	-0.10 ± 0.12 ± 0.003(col)	64 K	-0.059 ± 0.094 ± 0.002(col)	50.2 K	-0.076 ± 0.062 ± 0.003(col)	16 K	-0.044 ± 0.066 ± 0.005(col)
7	4 K	-0.87 ± 0.66 ± 0.07(col)	4 K	-0.23 ± 0.09 ± 0.02(col)	4 K	-0.14 ± 0.10 ± 0.01(col)	2 K	-0.97 ± 0.65 ± 0.19(col)

$\sigma_{\langle S_{\mathrm{MC}}^{(0+1)} \rangle}$, see Eqs. (70) and (38). The final values for $R^{(V)}$ are listed in Table 12 where in addition to the errors shown in the plots we have added those emerging from the determination of the color-sum average. In the lower graphs of Figs. 22–25 we plot the number of phase-space point evaluations needed to reach a certain relative integration uncertainty on $R_{\mathrm{MC}}^{(V)}(N_{\mathrm{MC}})$. We show in Table 11 the results of the curve fittings represented by the dashed lines in these plots.

As is clear from these Monte Carlo averaging tests and results, the convergence of the integrations is satisfactory and suitable for future applications of the color-dressing techniques in NLO calculations. If faster sampling convergence is required we can evaluate multiple color configurations per phase-space point. This is shown in the graphs, where we have chosen to evaluate four color configurations at one phase-space point.

5. Conclusions

In this paper we explored the possibility of color sampling within the context of D-dimensional generalized unitarity. Up to now generalized unitarity has only been used within the context of color-ordered primitive amplitudes. In the color-ordered approach, color is treated differently from the other quantum numbers such as spin and flavor. This makes the reconstruction of the full one-loop amplitude rather cumbersome.

We have reformulated the D-dimensional generalized unitarity formalism to include color dressing. That is, we choose the explicit color of each parton, together with all other quantum numbers, for each Monte Carlo event. In this way all particles, colored or colorless, are treated
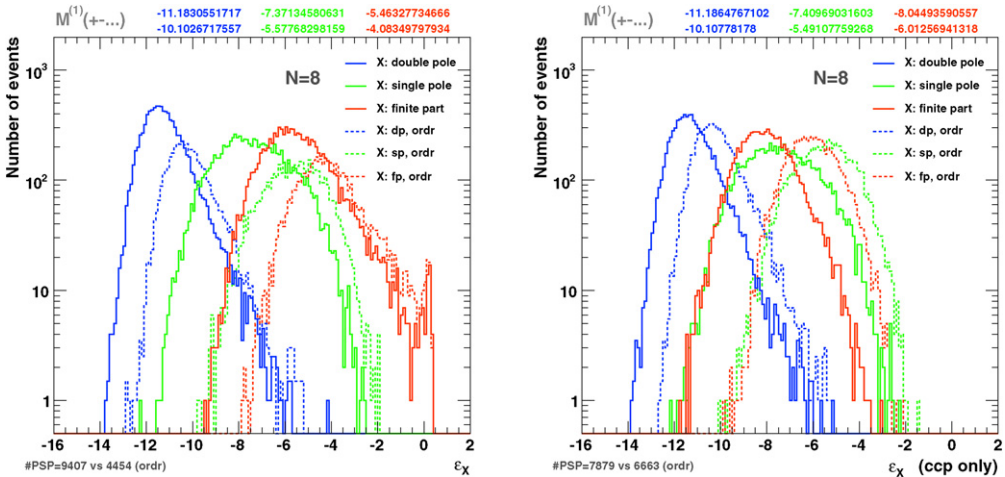
Fig. 15. Double-, single-pole and finite-part accuracy distributions (upper part) and scatter graphs (lower part) extracted from double-precision computations of one-loop amplitudes for $n = \mathrm{N} = 8$ gluons with polarizations $\lambda_k = + - + - + - + -$ and randomly chosen non-zero color configurations. The virtual corrections were calculated at random phase-space points satisfying the cuts detailed in the text. Unstable solutions were vetoed. Results from the color-dressed algorithm are compared with those of the color-ordered method indicated by dashed curves and brighter dots in the plots. The 5(4)-dimensional case is shown in the top left (right) and center (bottom) part of the figure. The definitions of ε and r are given in the text; the number of points contained by each scatter graph is found in the lower left.
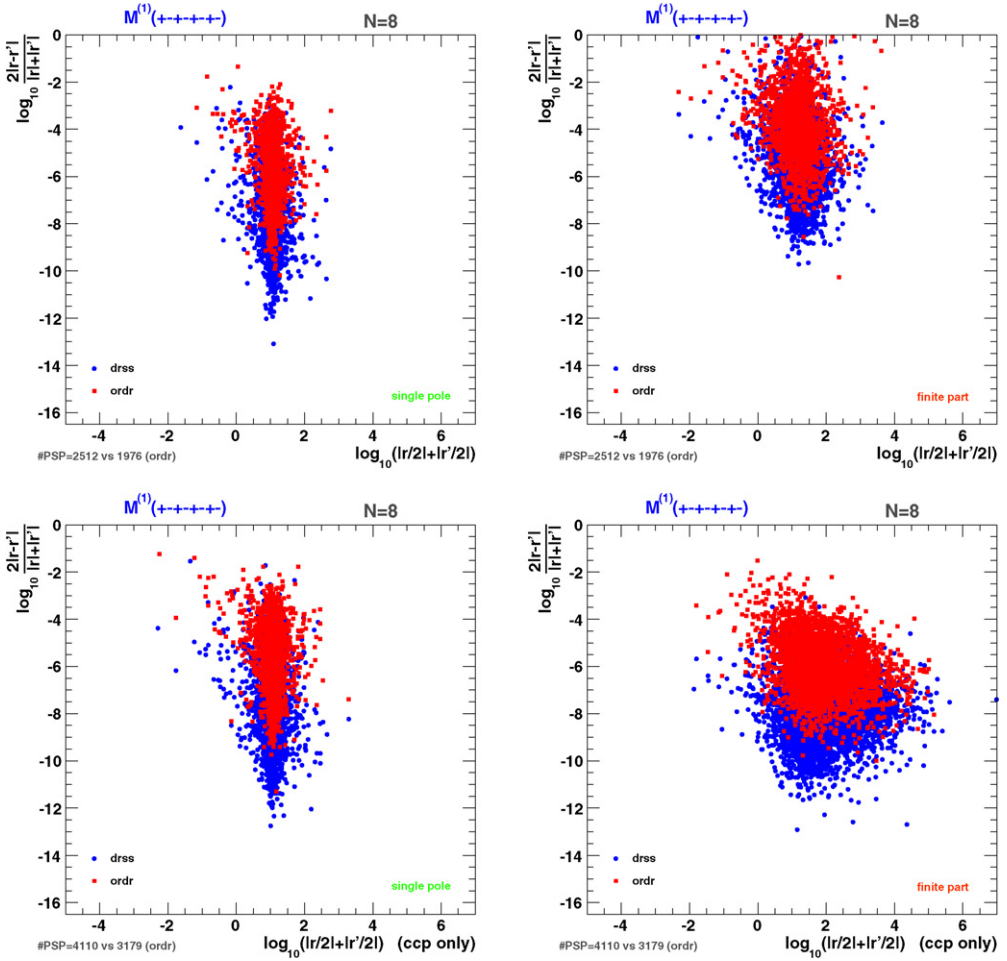
Fig. 15. (*continued*)

on an equal footing. There is no distinction between different particles as far as the formalism goes. Consequently, the resulting algorithm is independent of the type and flavor of the external particles. E.g. the same algorithm calculates the 6-gluon virtual corrections, the 6-photon virtual corrections and the $W + 6$ parton virtual corrections.

The use of unordered amplitudes requires the partition of the external legs into unordered subsets. This is necessary for the calculation of the tree-level amplitudes as well as for generating all the unitarity cuts. As a result the complexity of the resulting algorithm is exponential. That is, the computer time needed to calculate the virtual corrections grows with a constant multiplicative factor when one adds external particles. In addition, we have to sum over all color states of the internal lines. One may conclude from these general features that the implementation of the color-dressed D-dimensional generalized unitarity is less efficient in comparison with an implementation based on ordered primitive amplitudes. As we have explicitly demonstrated for the example of calculating the virtual corrections to n-gluon scattering, this is not the case. We compared the color-sampling approach for both the color-ordered and color-dressed

case. The calculation of the virtual corrections in the color-dressed case scales as 7^n, while in the color-ordered case the effective scaling up to 10 gluons behaves as 9^n. Moreover, the color-dressed method gives better accuracies compared to the color-ordered evaluations in calculating the values of the one-loop amplitudes. The improvements become more obvious for an increasing number n of gluons.

As we showed for n-gluon scattering, the color-dressed approach becomes more efficient than the color-ordered method for large n. One could argue that the differences are small and color sampling over the ordered n-gluon amplitudes will work as well. However, when including quarks and other electro-weak particles the color-dressed approach will easily win out over the color-ordered approach. This is because any notion of primitive amplitudes is absent. The algorithm simply calculates the virtual correction. Moreover, the color-dressed algorithm remains identical when including quarks and electro-weak particles. It is this algorithmic simplicity that will enable us to employ parallel programming to significantly improve the computer evaluation time.

We conclude that the color-dressed formulation is competitive for calculating one-loop virtual corrections for n-gluon scattering. It is expected that it will be even more efficient in calculating virtual corrections for processes involving quarks and electro-weak gauge bosons in addition to the gluons.
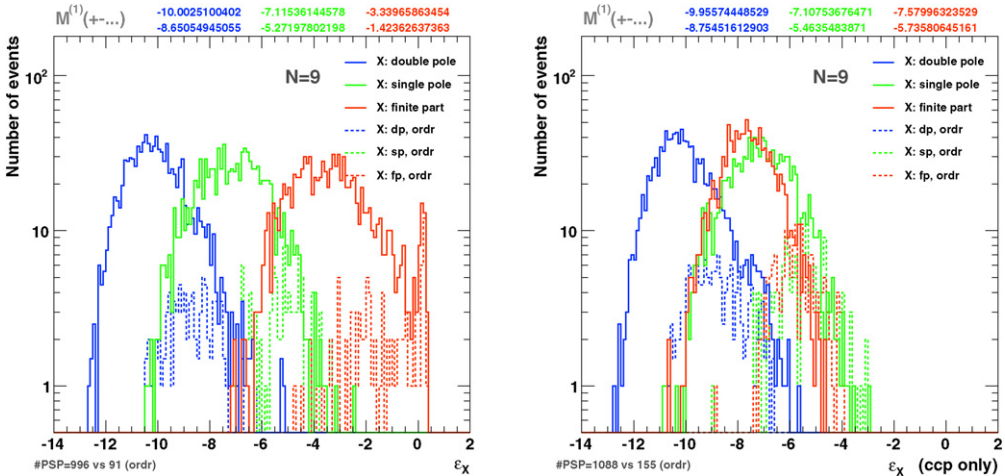
Acknowledgements

Fig. 16. Double-, single-pole and finite-part accuracy distributions (upper part) and scatter graphs (lower part) extracted from double-precision computations of one-loop amplitudes for $n = \mathrm{N} = 9$ gluons with polarizations $\lambda_k = + - + - + - + - +$ and randomly chosen non-zero color configurations. The virtual corrections were calculated at random phase-space points satisfying the cuts detailed in the text. Unstable solutions were vetoed. Results from the color-dressed algorithm are compared with those of the color-ordered method indicated by dashed curves and brighter dots in the plots. The 5(4)-dimensional case is shown in the top left (right) and center (bottom) part of the figure. The definitions of ε and r are given in the text; the number of points contained by each scatter graph is found in the lower left.
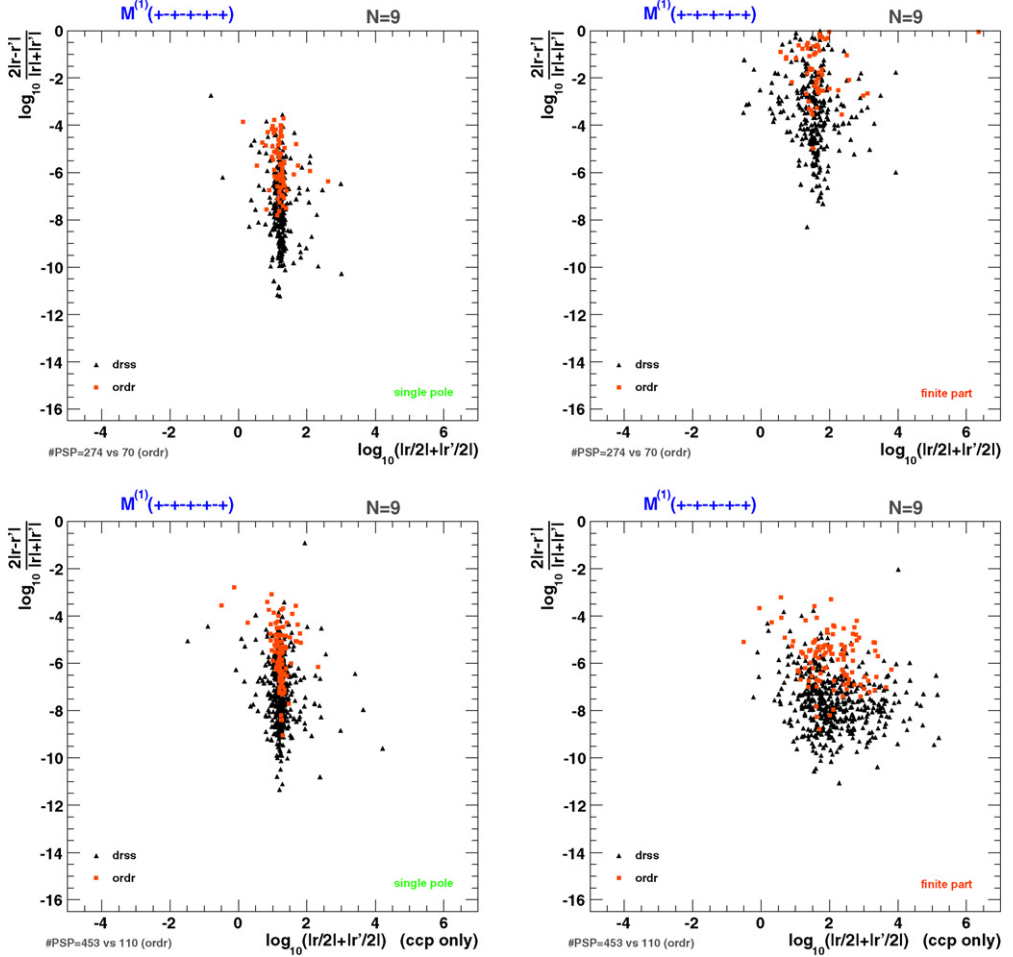
Fig. 16. (*continued*)

Appendix A. The tree-level 6-quark amplitude

As an example we can take a few recursive steps in calculating the 6-quark tree-level matrix element. We start with the definition of the tree-level matrix element in terms of the 5-quark fermionic current

$$\mathcal{M}^{(0)}(\mathbf{u}, \bar{\mathbf{u}}, \mathbf{d}, \bar{\mathbf{d}}, \mathbf{s}, \bar{\mathbf{s}}) = P^{-1}\big[J(\mathbf{u}, \bar{\mathbf{u}}, \mathbf{d}, \bar{\mathbf{d}}, \mathbf{s}), J(\bar{\mathbf{s}})\big] \tag{A.1}$$

where we use the shorthand notation $\mathbf{u} = u_{i_1}^{\lambda_1}(K_1)$, $\bar{\mathbf{u}} = \bar{u}_{j_1}^{-\lambda_1}(K_2)$, $\mathbf{d} = d_{i_2}^{\lambda_2}(K_3)$, $\bar{\mathbf{d}} = \bar{d}_{j_2}^{-\lambda_2}(K_4)$, $\mathbf{s} = s_{i_3}^{\lambda_3}(K_5)$ and $\bar{\mathbf{s}} = \bar{s}_{j_3}^{-\lambda_3}(K_6)$. The 5-quark fermionic current decomposes into

$$J_{\bar{\mathbf{s}}}(\mathbf{u}, \bar{\mathbf{u}}, \mathbf{d}, \bar{\mathbf{d}}, \mathbf{s}) = P_{\bar{\mathbf{s}}}\big[D\big[J(\mathbf{d}, \bar{\mathbf{d}}, \mathbf{s}), J(\mathbf{u}, \bar{\mathbf{u}})\big]\big] + P_{\bar{\mathbf{s}}}\big[D\big[J(\mathbf{u}, \bar{\mathbf{u}}, \mathbf{s}), J(\mathbf{d}, \bar{\mathbf{d}})\big]\big]$$
$$+ P_{\bar{\mathbf{s}}}\big[D\big[J(\mathbf{s}), J(\mathbf{u}, \bar{\mathbf{u}}, \mathbf{d}, \bar{\mathbf{d}})\big]\big]. \tag{A.2}$$
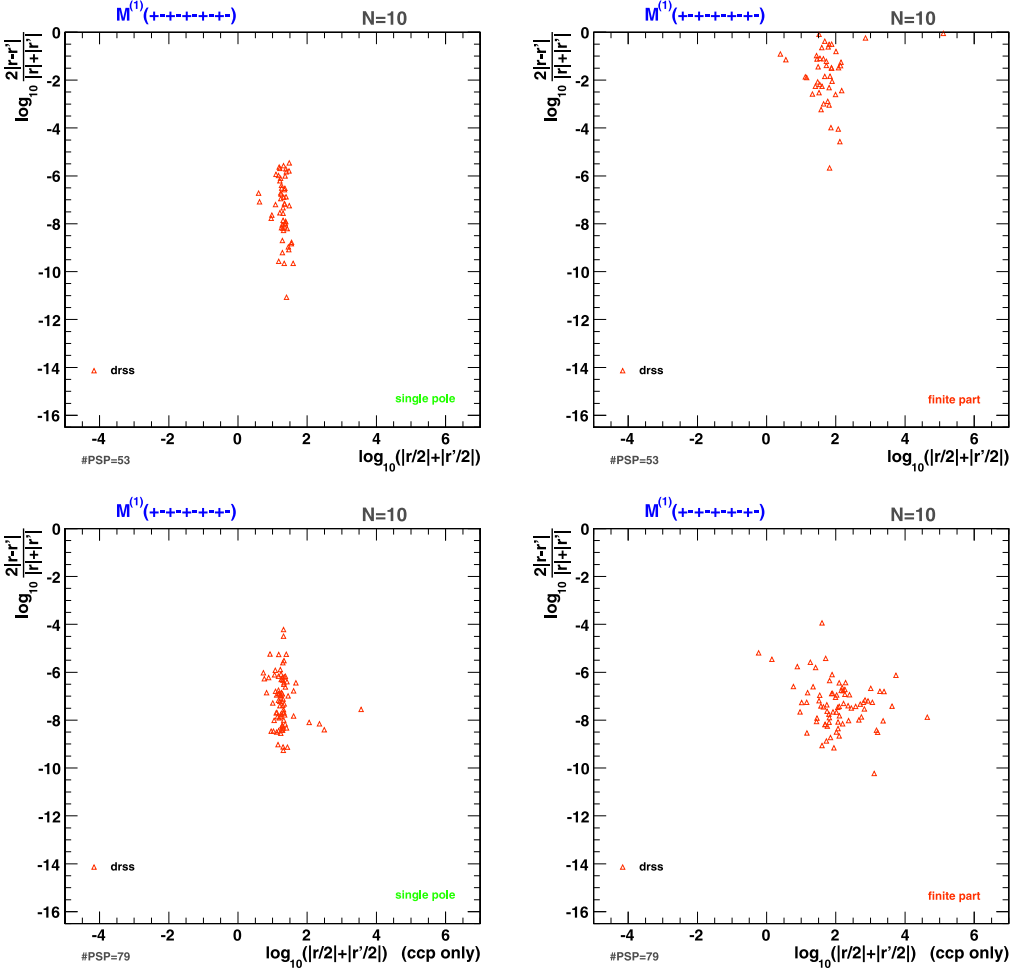
The 3-quark fermionic current decomposes into

Fig. 17. Single-pole and finite-part scatter graphs extracted from the double-precision computation of one-loop amplitudes for $n = N = 10$ gluons with polarizations $\lambda_k = + - + - + - + - + -$ and randomly chosen non-zero color configurations. The virtual corrections were calculated at random phase-space points satisfying the cuts as described in the text. Unstable solutions were vetoed and, therefore, not included in the plots. The upper (lower) row of plots shows the results obtained from the 5(4)-dimensional color-dressed algorithm. For the definition of r, see text. The number of points contained by each scatter graph can be found in the lower left.

$$J_{\bar{\mathbf{s}}}(\mathbf{q}, \bar{\mathbf{q}}, \mathbf{s}) = P_{\bar{\mathbf{s}}}\big[D\big[J(\mathbf{s}), J(\mathbf{q}, \bar{\mathbf{q}})\big]\big], \tag{A.3}$$

where $\mathbf{q} \in \{\mathbf{u}, \mathbf{d}\}$ and $\bar{\mathbf{q}} \in \{\bar{\mathbf{u}}, \bar{\mathbf{d}}\}$. The 1-quark fermionic current is simply the source term. Finally the 4-quark gluonic current is given by

$$
\begin{aligned}
J_{\mathbf{g}}(\mathbf{u}, \bar{\mathbf{u}}, \mathbf{d}, \bar{\mathbf{d}}) = {} & P_{\mathbf{g}}\big[D\big[J(\mathbf{u}), J(\mathbf{d}, \bar{\mathbf{d}}, \mathbf{u})\big]\big] + P_{\mathbf{g}}\big[D\big[J(\mathbf{u}, \mathbf{d}, \bar{\mathbf{u}}), J(\bar{\mathbf{u}})\big]\big] \\
& + P_{\mathbf{g}}\big[D\big[J(\mathbf{d}), J(\mathbf{u}, \bar{\mathbf{u}}, \mathbf{d})\big]\big] + P_{g}\big[D\big[J(\mathbf{d}, \mathbf{u}, \bar{\mathbf{u}}), J(\bar{\mathbf{d}})\big]\big],
\end{aligned}
\tag{A.4}
$$

and the 2-quark gluonic current is written as

$$J_{\mathbf{g}}(\mathbf{q}, \bar{\mathbf{q}}) = P_{\mathbf{g}}\big[D\big[J(\mathbf{q}), J(\bar{\mathbf{q}})\big]\big]. \tag{A.5}$$
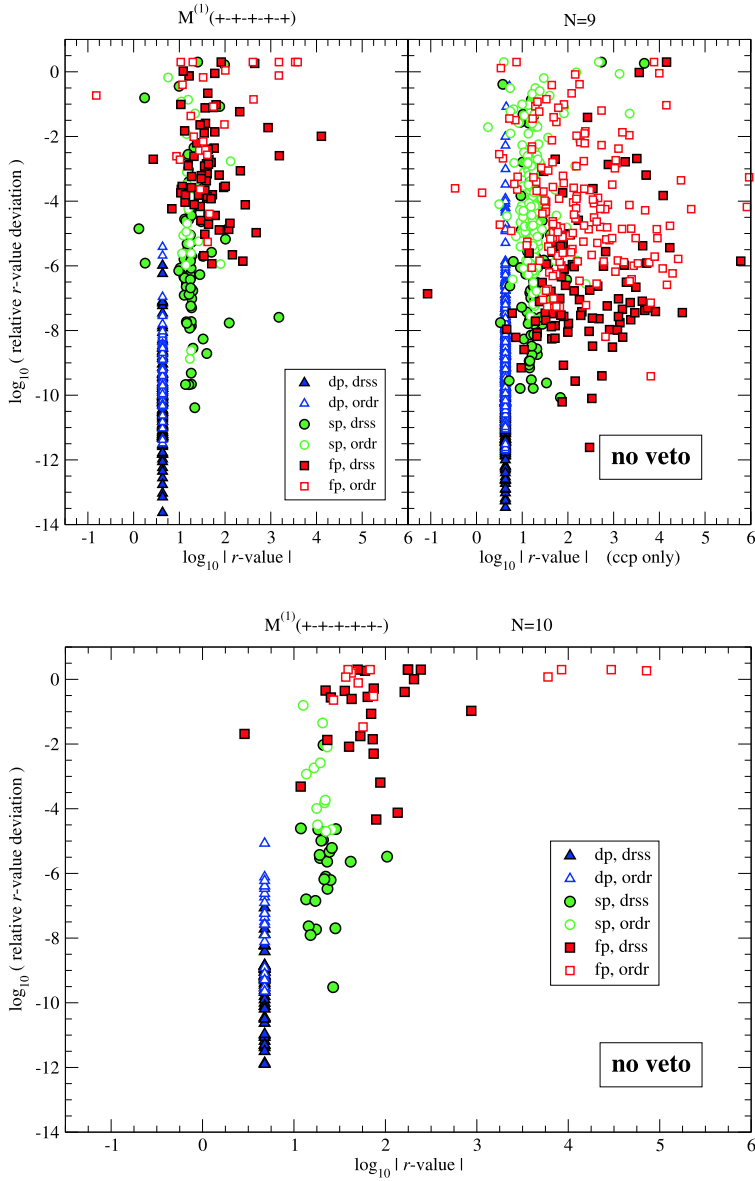
Fig. 18. Double-, single-pole and finite-part scatter graphs visualizing the accuracy of double-precision evaluations of one-loop amplitudes for $n = N = 9$ and 10 gluons of alternating polarizations. Randomly chosen non-zero color configurations were used. Note that unstable solutions were not vetoed and therefore included in this presentation. The virtual corrections were calculated at random phase-space points satisfying the cuts as described in the text. Results of the 5-dimensional algorithms either based on color ordering (ordr) or color dressing (drss) are shown; for $n = N = 9$, the "4D-case" results are also given (ccp only). For the definition of r, see text; axis labels as used in Fig. 17 are understood. The rightmost graph contains $\mathcal{O}(20)$ points per ϵ-pole, while the left plot of the "5(4)D-case" has approximately 50(120) points per pole.
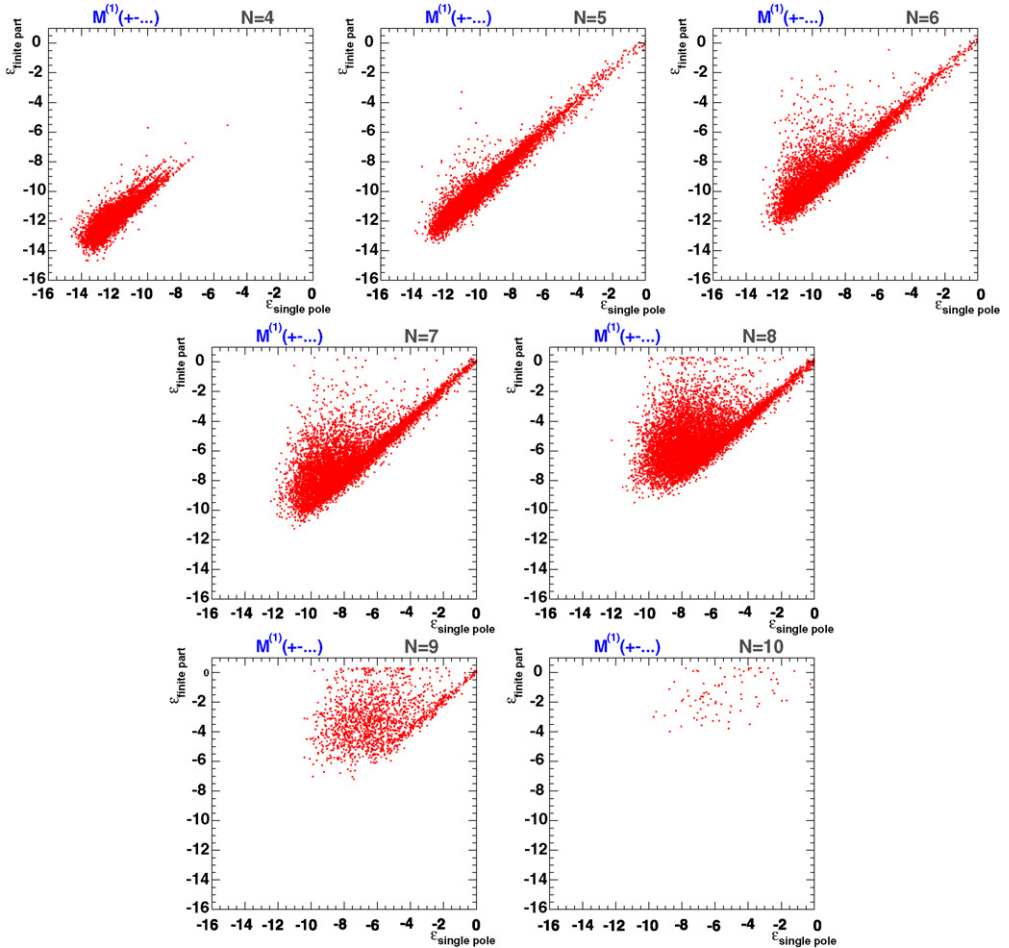
Fig. 19. Finite-part versus single-pole accuracy (in double precision) as achieved in one-loop amplitude calculations using the color-dressed approach for various numbers $n = \mathrm{N}$ of external gluons with polarizations $\lambda_k = + - \cdots + -(+)$ and colors randomly chosen among non-zero configurations. Note that unstable solutions have not been vetoed. The $n = \mathrm{N} = 9$ and $n = \mathrm{N} = 10$ graphs only contain $1.6 \cdot 10^3$ and 87 points, respectively, whereas all other plots comprise 10^4 points.

The above steps define the 6-quark LO amplitude recursively as would be done by the algorithm. Note that we have ignored all flavor violating currents.

Appendix B. The implemented gluon recursion relation

Making use of the color-flow representation [43], we define the color-dressed gluon currents as 3×3 matrices of ordered gluon currents:

$$J_\mu^{(IJ)}\big(g_1^{\lambda_1}\big) = \delta_{j_1}^I \delta_J^{i_1} J_\mu\big(g_1^{\lambda_1}\big), \tag{B.1}$$

where the external gluon g_1 has the polarization λ_1 and four-momentum K_1, its colors are denoted by $(ij)_1$. The color-flow labels of the dressed current are (IJ) and μ indicates the Lorentz
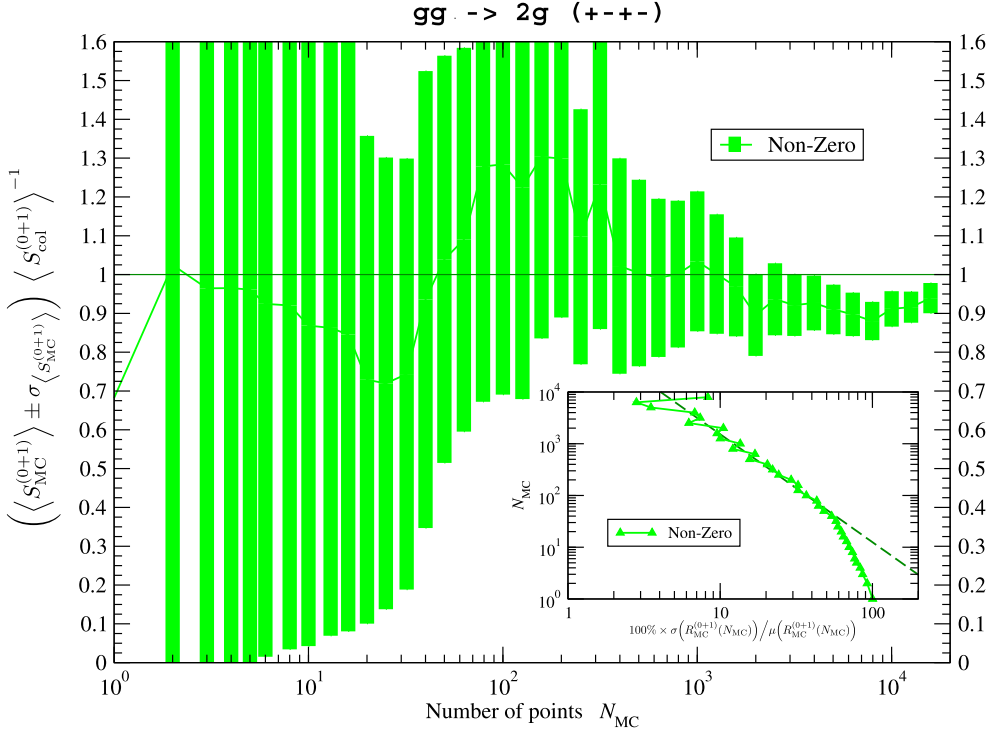
Fig. 20. Consistency test for the Monte Carlo integration of 4-gluon virtual corrections using "Non-Zero" color sampling compared to exact color summing. As a function of the number N_{MC} of evaluated phase-space points the $R^{(0+1)}$-ratio is plotted converging to one as it should be – however only the errors due to color sampling are shown, see text for the details. The inserted plot displays the number of phase-space evaluations needed to reach a given relative accuracy on $R_{MC}^{(0+1)}(N_{MC})$ while Monte Carlo integrating; cf. Eq. (71). The dashed line depicts the fit function $\sigma/\mu = A\,N_{MC}^{-B}$; see also Table 11.

label. Using this definition, the connection to the compact notation introduced in Section 3.1 is found as

$$J_{\mathbf{g}}(\mathbf{g}_1) = \delta^{Ii_1}\delta^{Jj_1}\varepsilon_\mu^{\lambda_1}(K_1) \equiv \delta_{j_1}^J \delta_I^{i_1} J_\mu\big(g_1^{\lambda_1}\big) = J_\mu^{(JI)}\big(g_1^{\lambda_1}\big). \tag{B.2}$$

Since we only consider gluons, a plain numbering of the external particles $\mathbf{g}_k = \{g_k, \lambda_k, (ij)_k, K_k\}$ is sufficient and helps simplify the notation such that the color dressing becomes more empha-sized. Hence, in all what follows we write $J_{\mathbf{g}}(\mathbf{1}) = \delta_{j_1}^J \delta_I^{i_1} J_\mu(1) = J_\mu^{(JI)}(1)$. Dressed n-gluon currents are then described by

$$J_\mu^{(IJ)}(1, 2, \ldots, n) = \sum_{\sigma \in S_n} \delta_{j_{\sigma_1}}^I \delta_{j_{\sigma_2}}^{i_{\sigma_1}} \cdots \delta_{j_{\sigma_n}}^{i_{\sigma_{n-1}}} \delta_J^{i_{\sigma_n}} J_\mu(\sigma_1, \sigma_2, \ldots, \sigma_n), \tag{B.3}$$

which follows as a consequence of the color decomposition of the tree-level amplitude into or-dered ones:

$$\mathcal{M}^{(0)}(1, 2, \ldots, n, n+1) = \sum_{\sigma \in S_n} \delta_{j_{\sigma_1}}^{i_{n+1}} \delta_{j_{\sigma_2}}^{i_{\sigma_1}} \cdots \delta_{j_{\sigma_n}}^{i_{\sigma_{n-1}}} \delta_{j_{n+1}}^{i_{\sigma_n}} m^{(0)}(\sigma_1, \sigma_2, \ldots, \sigma_n, n+1). \tag{B.4}$$
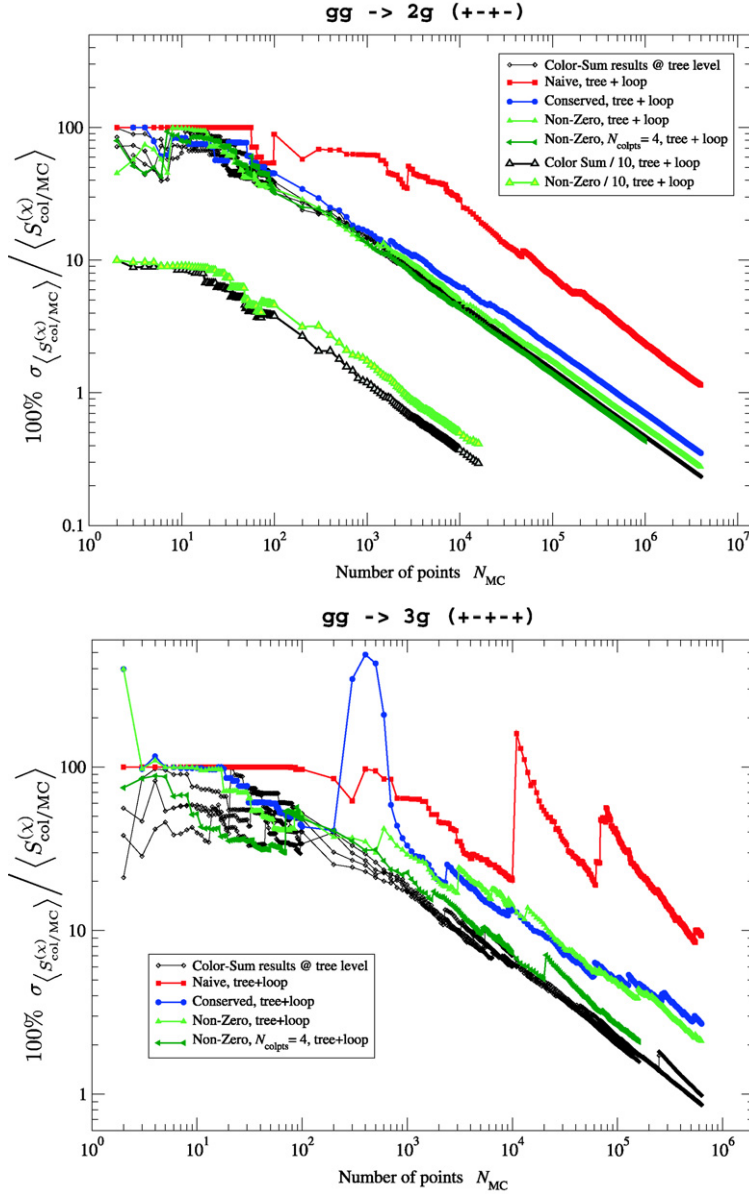
Fig. 21. Relative errors of the Monte Carlo phase-space integrations of color-summed and color-sampled 4- and 5-gluon matrix elements at the Born ($\chi = 0$) and Born plus virtual correction ($\chi = 0 + 1$) level. The errors are shown as functions of the number of generated flat phase-space points. The phase-space cuts are given in Eq. (65).

The vectors σ describe the elements of the permutations S_n of the set $\{1, 2, \ldots, n\}$. With the color-ordered amplitudes $m^{(0)}(\sigma_1, \sigma_2, \ldots, \sigma_n, n + 1)$ expressed through ordered J-currents and the definition of the dressed currents at hand, we can re-write the last equation and formulate the tree-level amplitude in terms of the color-dressed currents:
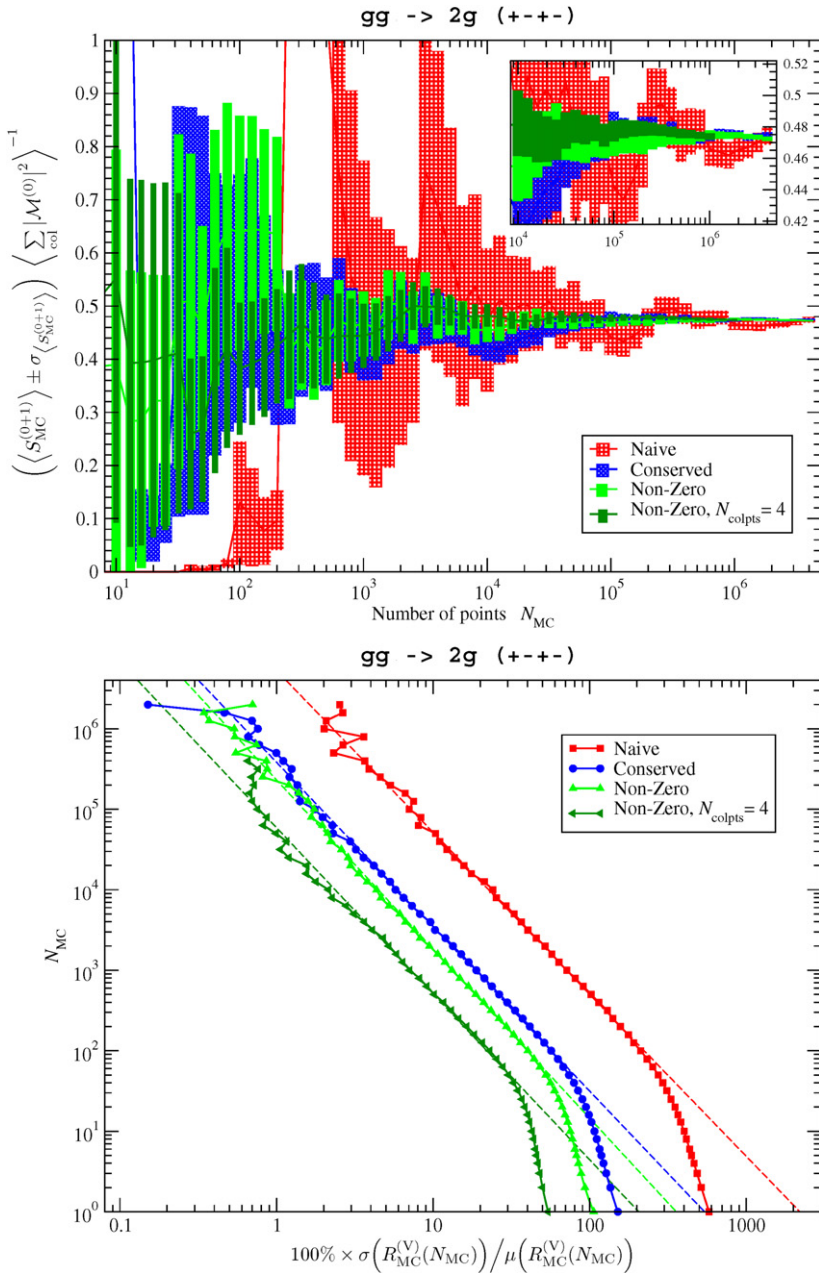
Fig. 22. Upper graph: convergence of the 4-gluon virtual corrections integration as a function of the number of evaluated phase-space points. Also shown is the standard deviation on the color-sampled average $\langle S_{MC}^{(0+1)} \rangle$ as an estimator of the integration uncertainty. Lower graph: convergence of the Monte Carlo integration, where the relative integration uncertainty is shown as a function of the number of phase-space evaluations. The dashed lines describe the fit functions $\sigma/\mu = A N_{MC}^{-B}$, see also Table 11. The "Naive", "Conserved" and "Non-Zero" color-sampling methods are explained in Section 3.3. The points indicated by "Non-Zero, $N_{colpts=4}$" average over 4 color configurations per phase-space point.
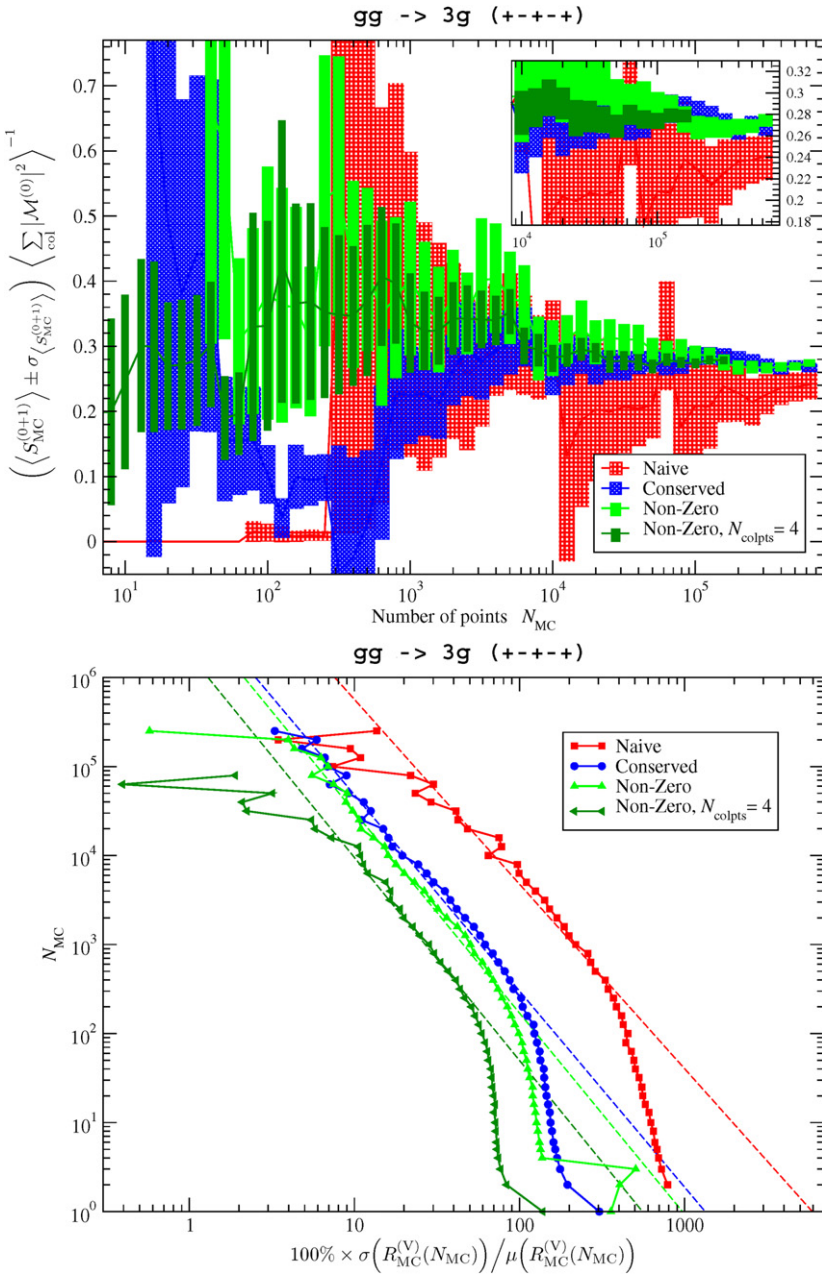
Fig. 23. Upper graph: convergence of the 5-gluon virtual corrections integration as a function of the number of evaluated phase-space points. Also shown is the standard deviation on the color-sampled average $\langle S_{\mathrm{MC}}^{(0+1)} \rangle$ as an estimator of the integration uncertainty. Lower graph: convergence of the Monte Carlo integration, where the relative integration uncertainty is shown as a function of the number of phase-space evaluations. The dashed lines describe the fit functions $\sigma/\mu = A N_{\mathrm{MC}}^{-B}$, see also Table 11. The "Naive", "Conserved" and "Non-Zero" color-sampling methods are explained in Section 3.3. The points indicated by "Non-Zero, $N_{\mathrm{colpts}=4}$" average over 4 color configurations per phase-space point.
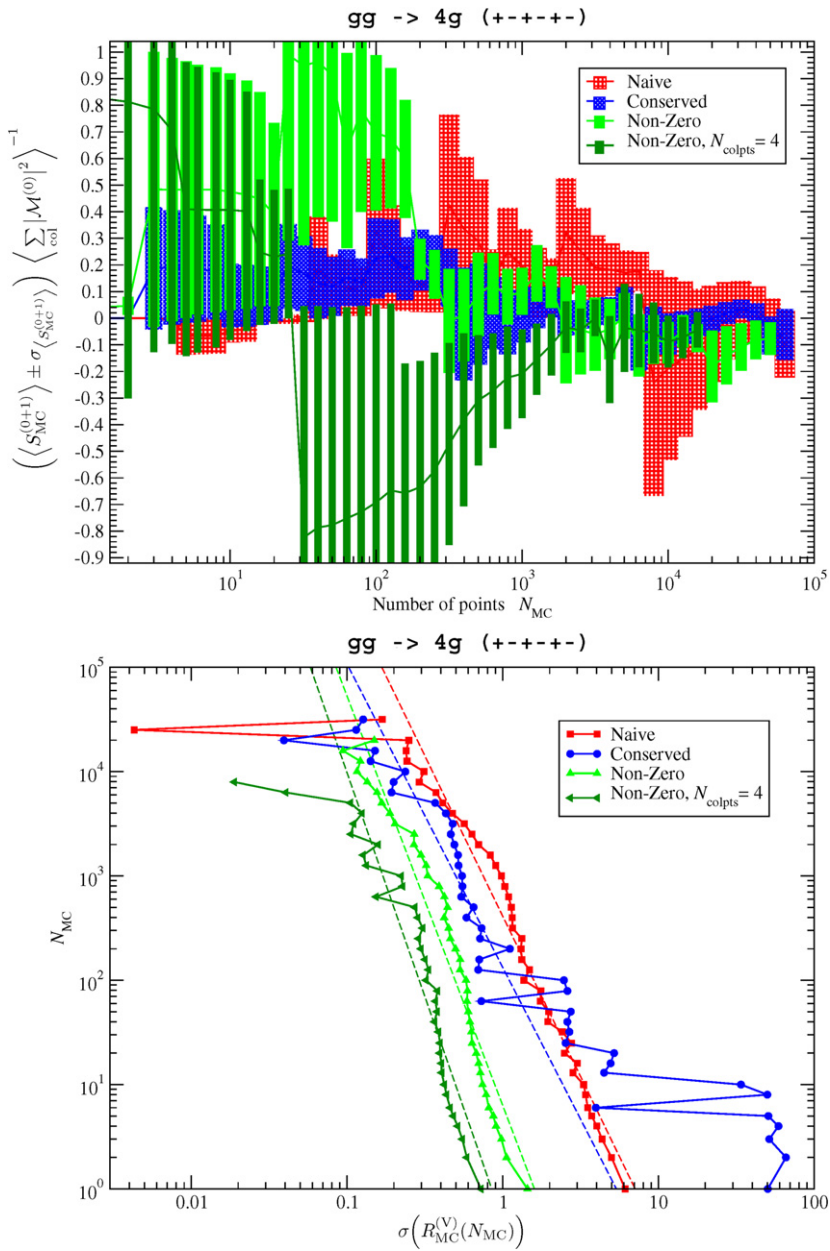
Fig. 24. Upper graph: convergence of the 6-gluon virtual corrections integration as a function of the number of evaluated phase-space points. Also shown is the standard deviation on the color-sampled average $\langle S_{MC}^{(0+1)} \rangle$ as an estimator of the integration uncertainty. Lower graph: convergence of the Monte Carlo integration, where this time the standard deviation is shown as a function of the number of phase-space evaluations. Note that for this case, the virtual corrections are as large as the LO contributions so that the full result is close to zero. The dashed lines describe the fit functions $\sigma = A N_{MC}^{-B}$, see also Table 11. The "Naive", "Conserved" and "Non-Zero" color-sampling methods are explained in Section 3.3. The points indicated by "Non-Zero, $N_{colpts=4}$" average over 4 color configurations per phase-space point.
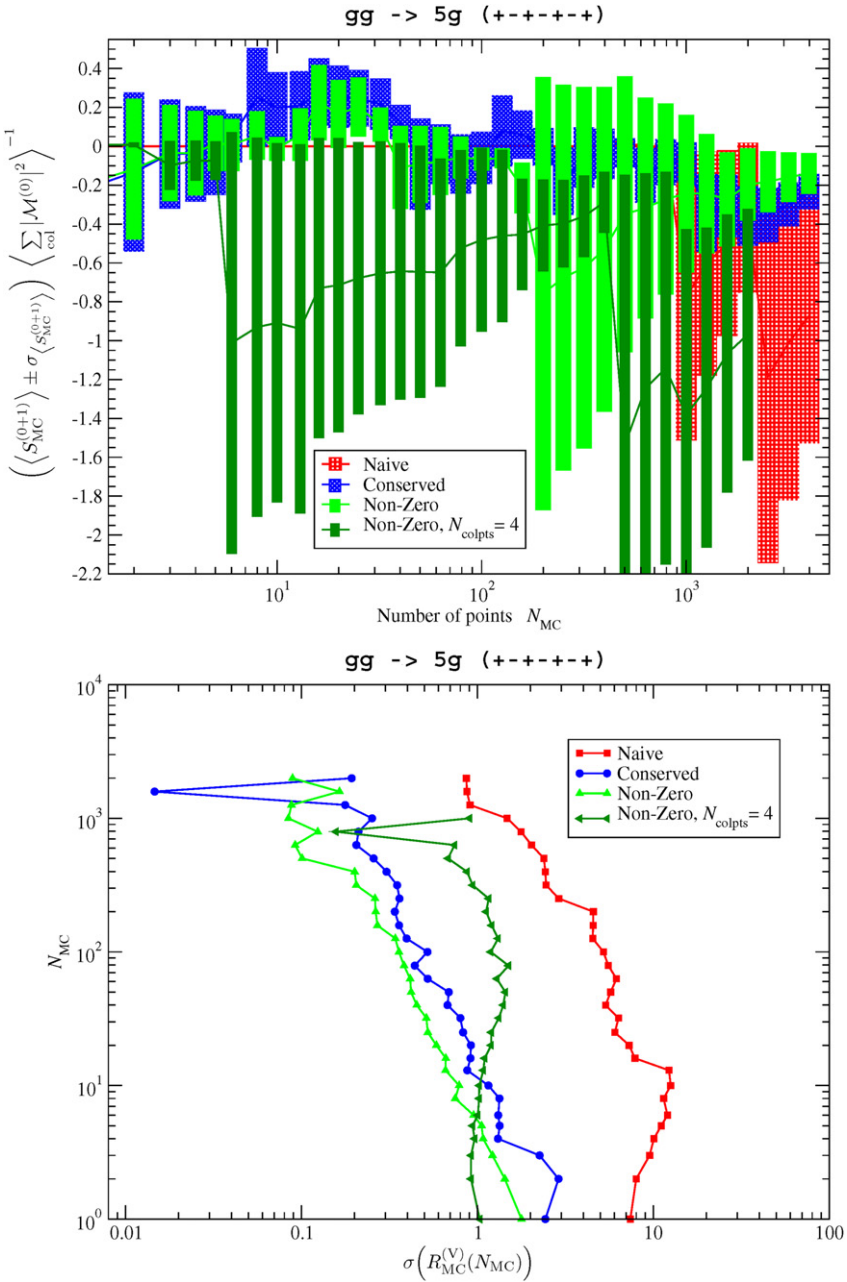
Fig. 25. Upper graph: convergence of the 7-gluon virtual corrections integration as a function of the number of evaluated phase-space points. Also shown is the standard deviation on the color-sampled average $\langle S_{\mathrm{MC}}^{(0+1)} \rangle$ as an estimator of the integration uncertainty. Lower graph: convergence of the Monte Carlo integration, where for this case, only the standard deviation is shown as a function of the number of phase-space evaluations. The "Naive", "Conserved" and "Non-Zero" color-sampling methods are explained in Section 3.3. The points indicated by "Non-Zero, $N_{\mathrm{colpts}=4}$" average over 4 color configurations per phase-space point.

$$\mathcal{M}^{(0)}(1, 2, \ldots, n, n+1) = K^2_{\{1,2,\ldots,n\}} \sum_{\sigma \in S_n} \delta^I_{j_{\sigma_1}} \delta^{i_{\sigma_1}}_{j_{\sigma_2}} \cdots \delta^{i_{\sigma_{n-1}}}_{j_{\sigma_n}} \delta^{i_{\sigma_n}}_J$$

$$\times J_\mu(\sigma_1, \sigma_2, \ldots, \sigma_n) \delta^J_{j_{n+1}} \delta^{i_{n+1}}_I J^\mu(n+1)$$

$$= K^2_{\{1,2,\ldots,n\}} J^{(IJ)}_\mu(1, 2, \ldots, n) J^{(JI),\mu}(n+1). \tag{B.5}$$

Owing to the simple color structure of the one-gluon current, the summation over the color indices (IJ) effectively reduces to the calculation of a single scalar product of the ordered currents $J^{(i_{n+1}j_{n+1})}_\mu$ and $J^{(j_{n+1}i_{n+1}),\mu}$. The invariant-mass prefactor K^2 is determined by the gluon momenta via $K^2_{\{1,2,\ldots,n\}} = (K_1 + K_2 + \cdots + K_n)^2$. The one-gluon current is given in Eq. (B.1), while the multi-gluon current is obtained recursively. Starting from Eq. (B.3), one incorporates the ordered gluon recurrence relation to evaluate $J_\mu(\sigma_1, \ldots, \sigma_n)$ and re-groups accordingly to identify the partitioning. After some algebra, one finds

$$J^{IJ}_\mu(1, 2, \ldots, n) = K^{-2}_{\{1,2,\ldots,n\}} \Bigg[\sum_{P_{\pi_1\pi_2}(1,\ldots,n)} \left(\delta^{ILN}_{KMJ} - \delta^{INL}_{MKJ} \right) \left[J^{(KL)}_\mu(\pi_1), J^{(MN)}_\mu(\pi_2) \right]$$

$$+ \sum_{P_{\pi_1\pi_2\pi_3}(1,\ldots,n)} \left(\delta^{ILNP}_{KMOJ} + \delta^{IPNL}_{OMKJ} - \delta^{ILPN}_{KOMJ} - \delta^{INPL}_{MOKJ} \right)$$

$$\times \left(\left\{ J^{(KL)}_\mu(\pi_1), J^{(MN)}_\mu(\pi_2), J^{(OP)}_\mu(\pi_3) \right\} + \pi_1 \leftrightarrow \pi_2 \right) \Bigg] \tag{B.6}$$

where we have employed the bracket notation for ordered-current operations, which was introduced in Ref. [26]. The partition sums are explained in Section 3.1 and an implicit summation over the color indices K, L, M, N, O, P is understood. To efficiently compute the dressed currents, the color factors in front of the operator brackets can be pre-calculated such that the computation of zero color-weight contributions can be avoided. We have used the shorthand notation

$$\delta^{ik\cdots m}_{jl\cdots n} = \delta^i_j \delta^k_l \cdots \delta^m_n. \tag{B.7}$$

The recursion relation presented in Eq. (B.6) scales asymptotically as 4^n, since we kept the 4-gluon vertex as an entity in our calculation. As a consequence we have to evaluate 3-subset partitions and the corresponding curly brackets that merge three different dressed currents.

References

[1] T. Stelzer, W.F. Long, Comput. Phys. Commun. 81 (1994) 357, arXiv:hep-ph/9401258.
[2] F. Krauss, R. Kuhn, G. Soff, JHEP 0202 (2002) 044, arXiv:hep-ph/0109036.
[3] M.L. Mangano, M. Moretti, F. Piccinini, R. Pittau, A.D. Polosa, JHEP 0307 (2003) 001, arXiv:hep-ph/0206293.
[4] P.D. Draggiotis, R.H.P. Kleiss, C.G. Papadopoulos, Eur. Phys. J. C 24 (2002) 447, arXiv:hep-ph/0202201.
[5] E. Boos, et al., CompHEP Collaboration, Nucl. Instrum. Meth. A 534 (2004) 250, arXiv:hep-ph/0403113.
[6] C.G. Papadopoulos, M. Worek, Eur. Phys. J. C 50 (2007) 843, arXiv:hep-ph/0512150.
[7] A. Cafarella, C.G. Papadopoulos, M. Worek, Comput. Phys. Commun. 180 (2009) 1941, arXiv:0710.2427 [hep-ph].
[8] T. Gleisberg, S. Höche, JHEP 0812 (2008) 039, arXiv:0808.3674 [hep-ph].
[9] Z. Bern, L.J. Dixon, D.C. Dunbar, D.A. Kosower, Nucl. Phys. B 435 (1995) 59, arXiv:hep-ph/9409265.
[10] R. Britto, F. Cachazo, B. Feng, Nucl. Phys. B 725 (2005) 275, arXiv:hep-th/0412103.
[11] C.F. Berger, Z. Bern, L.J. Dixon, D. Forde, D.A. Kosower, Phys. Rev. D 74 (2006) 036009, arXiv:hep-ph/0604195.
[12] G. Ossola, C.G. Papadopoulos, R. Pittau, Nucl. Phys. B 763 (2007) 147, arXiv:hep-ph/0609007.
[13] W.T. Giele, Z. Kunszt, K. Melnikov, JHEP 0804 (2008) 049, arXiv:0801.2237 [hep-ph].

[14] C.F. Berger, et al., Phys. Rev. D 78 (2008) 036003, arXiv:0803.4180 [hep-ph].

[15] A. van Hameren, C.G. Papadopoulos, R. Pittau, arXiv:0903.4665 [hep-ph].

[16] R. Keith Ellis, K. Melnikov, G. Zanderighi, arXiv:0906.1445 [hep-ph].

[17] K. Melnikov, M. Schulze, JHEP 0908 (2009) 049, arXiv:0907.3090 [hep-ph].

[18] G. Bevilacqua, M. Czakon, C.G. Papadopoulos, R. Pittau, M. Worek, JHEP 0909 (2009) 109, arXiv:0907.4723 [hep-ph].

[19] C.F. Berger, et al., arXiv:0907.1984 [hep-ph].

[20] C.F. Berger, et al., arXiv:0909.4949 [hep-ph].

[21] K. Melnikov, G. Zanderighi, arXiv:0910.3671 [hep-ph].

[22] T. Gleisberg, F. Krauss, Eur. Phys. J. C 53 (2008) 501, arXiv:0709.2881 [hep-ph].

[23] R. Frederix, T. Gehrmann, N. Greiner, JHEP 0809 (2008) 122, arXiv:0808.2128 [hep-ph].

[24] F.A. Berends, W. Giele, Nucl. Phys. B 294 (1987) 700.

[25] M.L. Mangano, S.J. Parke, Z. Xu, Nucl. Phys. B 298 (1988) 653.

[26] F.A. Berends, W.T. Giele, Nucl. Phys. B 306 (1988) 759.

[27] F.A. Berends, W.T. Giele, H. Kuijf, Nucl. Phys. B 333 (1990) 120.

[28] R. Kleiss, H. Kuijf, Nucl. Phys. B 312 (1989) 616.

[29] K. Ellis, W. Giele, Z. Kunszt, The NLO multileg working group: Summary report, Published in Les Houches 2007, Physics at TeV colliders, arXiv:0803.0494 [hep-ph].

[30] M. Bruinsma, The Caravaglios–Moretti algorithm and vanishing theorems in scalar theories, Master Thesis, Univ. of Amsterdam, 1996.

[31] P. Draggiotis, R.H.P. Kleiss, C.G. Papadopoulos, Phys. Lett. B 439 (1998) 157, arXiv:hep-ph/9807207.

[32] C. Duhr, S. Höche, F. Maltoni, JHEP 0608 (2006) 062, arXiv:hep-ph/0607057.

[33] Z. Bern, L.J. Dixon, D.C. Dunbar, D.A. Kosower, Nucl. Phys. B 425 (1994) 217, arXiv:hep-ph/9403226.

[34] R.K. Ellis, W.T. Giele, Z. Kunszt, K. Melnikov, G. Zanderighi, JHEP 0901 (2009) 012, arXiv:0810.2762 [hep-ph].

[35] F. Caravaglios, M.L. Mangano, M. Moretti, R. Pittau, Nucl. Phys. B 539 (1999) 215, arXiv:hep-ph/9807570.

[36] F. Caravaglios, M. Moretti, Phys. Lett. B 358 (1995) 332, arXiv:hep-ph/9507237.

[37] J. Winter, W.T. Giele, arXiv:0902.0094 [hep-ph].

[38] V. Del Duca, L.J. Dixon, F. Maltoni, Nucl. Phys. B 571 (2000) 51, arXiv:hep-ph/9910563.

[39] G. 't Hooft, Nucl. Phys. B 72 (1974) 461.

[40] M.L. Mangano, S.J. Parke, Phys. Rep. 200 (1991) 301, arXiv:hep-th/0509223.

[41] A. Kanaki, C.G. Papadopoulos, Comput. Phys. Commun. 132 (2000) 306, arXiv:hep-ph/0002082.

[42] A. Kanaki, C.G. Papadopoulos, arXiv:hep-ph/0012004.

[43] F. Maltoni, K. Paul, T. Stelzer, S. Willenbrock, Phys. Rev. D 67 (2003) 014026, arXiv:hep-ph/0209271.

[44] R.K. Ellis, W.T. Giele, Z. Kunszt, JHEP 0803 (2008) 003, arXiv:0708.2398 [hep-ph].

[45] S.D. Badger, JHEP 0901 (2009) 049, arXiv:0806.4600v1 [hep-ph].

[46] W.T. Giele, G. Zanderighi, JHEP 0806 (2008) 038, arXiv:0805.2152 [hep-ph].

[47] A. Lazopoulos, arXiv:0812.2998 [hep-ph].

[48] R.K. Ellis, W.T. Giele, Z. Kunszt, K. Melnikov, arXiv:0806.3467 [hep-ph].

[49] Z. Bern, A. De Freitas, L.J. Dixon, H.L. Wong, Phys. Rev. D 66 (2002) 085002, arXiv:hep-ph/0202271.

[50] R.K. Ellis, G. Zanderighi, JHEP 0802 (2008) 002, arXiv:0712.1851 [hep-ph].